Performance of Various Hybrid RANS-LES Turbulence Models in an Aerodynamics CFD Simulation of a Simple Pickup Truck Shape

by

Kyle Smolarek

**A thesis submitted in partial fulfillment
of the requirements for the degree of
Master of Science in Engineering
(Mechanical Engineering)
in the University of Michigan-Dearborn
2019**

Master's Thesis Committee:

**Professor Oleg Zikanov, Chair
Assistant Professor Youngki Kim
Professor Subrata Sengupta**

ACKNOWLEDGEMENTS

Credit to Ford Motor Company for generously lending their HPC resources and providing the simplified truck geometry. The simplified truck geometry is a variant of the Generic Truck Utility (GTU) model with an altered body and more detailed underbody. As of this writing, the GTU will soon be made available for public use. Thanks to my advisor for his guidance through the long process of writing this paper. Finally, thanks to my parents and brother for their support since I started my education in 1998.

TABLE OF CONTENTS

CHAPTER

LIST OF FIGURES

ABSTRACT

The top three best-selling vehicles in the United States are pickup trucks, therefore their unique aerodynamics are of considerable industrial interest. Hybrid RANS-LES turbulence models are popular in automotive aerodynamics CFD. Papers have examined their performance on simplified car shapes, but none have done so for a pickup truck shape. Three hybrid RANS-LES turbulence models—detached eddy simulation (DES), delayed detached eddy simulation (DDES), and improved delayed detached eddy simulation (IDDES)—were examined in incompressible, transient CFD on a simplified pickup truck shape using OpenFOAM. These models were also benchmarked against Spalart-Allmaras and k-ω SST steady RANS models. The hybrid RANS-LES turbulence models differed in values of drag and lift coefficients by up to 0.002 and 0.014, and predicted on average 0.040 and 0.078 higher than the steady RANS models, respectively. The flow fields of the hybrid RANS-LES models were largely similar to each other, but differed from the RANS results downstream of the front fascia and particularly in highly-detached regions, where they predicted earlier vortex bursting. Wind tunnel test data and flow visualization are required to confirm the results predicted by the hybrid RANS-LES models.

CHAPTER I: INTRODUCTION

1.1 Motivation

In the automotive industry, aerodynamics is concerned with the study of how air flows around a vehicle at speed, and the resultant forces and moments on the vehicle. For consumer vehicles, the drag force the force component anti-parallel to vehicle velocity is the primary focus. This is because the power of aerodynamic drag increases with the cube of speed; at freeway speeds, it is a larger contributor to the engine load than rolling resistance, driveline friction, or accessory load. Stricter fuel economy and emissions regulations, consumer demand for better fuel economy, and the advent of electric cars where driving range is at a premium due to limited battery capacity motivates manufacturers to decrease drag coefficient, C_d, as much as possible. On high-performance vehicles, low lift coefficient C_l is exploited to yield higher cornering speeds, higher top speeds, shorter braking distances, and ultimately faster lap times. C_d and C_l are defined as

$$\begin{aligned} C_d &= \frac{F_d}{1/2\rho U_\infty^2 A_f} \quad (1.1) \\ C_l &= \frac{F_l}{1/2\rho U_\infty^2 A_f}. \quad (1.2) \end{aligned}$$

A_f is the projected frontal area of the vehicle, U_∞ is the freestream velocity, ρ is the air density, and $\vec{F}_d$ and $\vec{F}_l$ are the resultant drag and lift forces, respectively.

Traditionally, cars were designed in the wind tunnel; however, continuous advances in CFD practice and computational power enable engineers to use it as a powerful design tool. In CFD, airflow over a CAD representation of the vehicle is modeled with the Navier-Stokes equations and solved on a high performance computer cluster. Compared to wind tunnel tests, CFD simulations are cheaper, faster, and allow deeper insight into the flow behavior. They can drive design optimization studies, which increases design iteration speed. In addition, as computer simulations, they do not abide by the constraints of physical testing, which opens the door to other modeling possibilities. For instance, instead of building an expensive active flow control device to test in the tunnel, the effect could be modeled in CFD by imposing a boundary condition on a surface.

Traditional CFD solvers use the finite volume method to linearize, discretize, and approximately solve the Navier-Stokes equations, although Lattice-Boltzmann methods are also popular. The turbulence modeling, finite volume schemes, and solver schemes are some of the many settings that must be chosen appropriately. Different models and schemes are well- or ill-suited for a given problem. Expert knowledge is required to configure the simulation correctly and obtain good results. Equally critical is the design of the computational mesh used to discretize the domain. The goal is to find a CFD setup and process that allows CFD models to be rapidly prototyped and ran with good correlation to the wind tunnel, the streets, and the race track. The less time engineers spend fiddling with the minutiae of CFD, the more time they have to interpret results and design better vehicles.

For all its merits, CFD still stands to be improved. Simulations are computationally expensive: it is common for simulations to run in-parallel on hundreds if not thousands of processors, and still take days to complete. Even then, predicted force coefficients and flow fields can be inaccurate, sometimes contradicting test results. These inaccuracies are due to a number of factors the least of which are mesh discretization error, fidelity of the CAD model, and the shortfalls of turbulence modeling. The search to make CFD faster and more accurate is ongoing.

This study will survey the performance of various turbulence models applied to the flow over a simple pickup truck shape. Such vehicles are popular in the North American market. Consequential flow phenomenon such as vortices, flow separation, pressure recovery, and wake behavior are directly affected by turbulence model selection. The turbulence models surveyed will be transient hybrid RANS-LES models, which have been popular in vehicle aerodynamics simulations over the past 15 years. These types of models are successful because they can resolve the large turbulent length scales found in vehicle aerodynamic flows, while modeling the effect of small length scales in dissipating turbulent kinetic energy. In the boundary layers, the model transitions to a RANS formulation, which is effective in simulating the small length scale, attached eddies. Importantly, these formulations tend to perform well in predicting pressure-induced flow separation.

CHAPTER II: LITERATURE REVIEW

2.1 Turbulence Modeling

Three different hybrid RANS-LES models were surveyed in this paper: DES, DDES, and IDDES. Two RANS turbulence models were used for comparison: Spalart-Allmaras and k-ω SST. k-ω SST is a two-equation turbulence model which is commonly used for pure RANS simulations in the automotive industry. Spalart-Allmaras is a one-equation turbulence model, which is used as both the RANS and subgrid stress model in DES, DDES, and IDDES.

2.1.1 Navier-Stokes Equations and the Difficulty of Direct Solution

The isothermal, incompressible, transient Navier-Stokes equations are [1]

$$\frac{\partial u_i}{\partial x_i} = 0, \tag{2.1}$$

$$\frac{\partial u_i}{\partial t} + \frac{\partial}{\partial x_j}\left(u_i u_j\right) = -\frac{1}{\rho}\frac{\partial p}{\partial x_i} + \nu \bigtriangledown^2 u_i \tag{2.2}$$

Where u_i, $i = 1,2,3$ are the velocity components, p is the pressure, and ρ, ν are the density and kinematic viscosity of the fluid. In order to accurately simulate a fluid flow field with a discretized representation, there must be sufficient spatial resolution in all regions to capture the smallest gradients and flow features. Laminar flow is characterized by large, smooth, dissipative flow features, making it easier to model. Turbulent flow, which is present in nearly every region of interest in vehicle aerodynamics, is chaotic and consists of various eddies of different length scales. According to Kolmogorov, at high Reynold's number the smallest length scales are statistically isotropic and independent of the large-scale eddies. In order to resolve the entire spectrum on discrete mesh, the cell size must be as small as the smallest possible length scale. This is the Kolmogorov microscale,

$$\eta \sim L \cdot Re^{-3/4}. \tag{2.3}$$

In a typical automotive aerodynamic flow, $U = 50\,\mathrm{m\,s^{-1}}$, $\nu = 1.2 \times 10^{-5}\,\mathrm{m^2/s}$, and $L = 4\,\mathrm{m}$. Then $\eta \sim 10^{-5}\,\mathrm{m}$ and

$$N \sim \left(\frac{L}{\eta}\right)^3 \sim 10^{15}. \tag{2.4}$$

Simulations that directly resolve the smallest length scale are called Direct Numerical Simulation (DNS). On the basis of cell count alone, this problem far exceeds current computational resources. For quick turnaround time, industrial simulations typically require $N \sim 10^6$.

2.1.2 Reynolds-Averaged Navier-Stokes Equations

For a steady-state solution, it is assumed that $\frac{\partial u_i}{\partial t} = 0$. For a turbulent flow field, $u(x,t)$ and $p(x,t)$ can be expressed in terms of mean and fluctuating quantities.

$$u(x,t) = \langle u \rangle (x) + u'(x,t) \tag{2.5}$$

$$p(x,t) = \langle p \rangle (x) + p'(x,t) \tag{2.6}$$

Where the averaging operation is defined as

$$\langle u \rangle (x) = \lim_{T \to \infty} \frac{1}{T} \int_0^T u(x,t)\,dt \tag{2.7}$$

$$\langle p \rangle (x) = \lim_{T \to \infty} \frac{1}{T} \int_0^T p(x,t)\,dt \tag{2.8}$$

Averaging the fluctuations around the mean quantities show that $\langle u' \rangle = 0$ and $\langle p' \rangle = 0$. The time derivative $\frac{\partial u_i}{\partial t}$ averages to zero. Applying this operation to the Navier-Stokes equations yields the

Reynolds Averaged Navier-Stokes (RANS) equations, see [1].

$$\frac{\partial \langle u_i \rangle}{\partial x_i} = 0 \tag{2.9}$$

$$\frac{\partial}{\partial x_j} \langle u_i u_j \rangle = -\frac{1}{\rho} \frac{\partial \langle p \rangle}{\partial x_i} + \nu \bigtriangledown^2 \langle u_i \rangle \tag{2.10}$$

Expanding the nonlinear term $\langle u_i u_j \rangle$ yields the Reynolds stress tensor τ_{ij}, so-called because it has the effect of turbulent momentum transport added to the transport produced by the viscous stress.

$$\tau_{ij} \equiv \langle u_i{}' u_j{}' \rangle = \langle u_i u_j \rangle - \langle u_i \rangle \langle u_j \rangle \tag{2.11}$$

The final RANS equations can then be expressed in terms of the averaged field variables and τ_{ij}

$$\frac{\partial \langle u_i \rangle}{\partial x_i} = 0 \tag{2.12}$$

$$\frac{\partial}{\partial x_j} \left(\langle u_i \rangle \langle u_j \rangle \right) = -\frac{1}{\rho} \frac{\partial \langle p \rangle}{\partial x_i} + \nu \bigtriangledown^2 \langle u_i \rangle - \frac{\partial \tau_{ij}}{\partial x_j}. \tag{2.13}$$

The Reynolds stress is unknown as a function of the mean flow field $\langle u \rangle (x,t)$ and $\langle p \rangle (x,t)$, so the function of turbulence modeling in RANS is to model τ_{ij}. All the RANS turbulence models surveyed in this paper are eddy viscosity models. These models assume that the Reynolds stress obeys the Boussinesq eddy viscosity hypothesis

$$\tau_{ij} \equiv \langle u_i{}' u_j{}' \rangle = -2\nu_t \langle S_{ij} \rangle + \frac{2}{3} \delta_{ij} k \tag{2.14}$$

The mean strain-rate tensor $\langle S_{ij} \rangle$ is

$$\langle S_{ij} \rangle = \frac{1}{2} \left(\frac{\partial \langle u_i \rangle}{\partial x_j} + \frac{\partial \langle u_j \rangle}{\partial x_i} \right) \tag{2.15}$$

and the turbulent kinetic energy k is

$$k \equiv \frac{1}{2}\langle u_i{}' u_j{}' \rangle = \frac{1}{2}\langle u_x{}' u_x{}' + u_y{}' u_y{}' + u_z{}' u_z{}' \rangle. \tag{2.16}$$

Thus in order to model the Reynolds stress τ_{ij}, the turbulence model must provide the eddy viscosity ν_t and turbulent kinetic energy k.

2.1.3 Spalart-Allmaras

The Spalart-Allmaras turbulence model is a one-equation eddy viscosity turbulence model, empirically calibrated to free-shear flows.[2]

$$\begin{aligned} \frac{\partial \tilde{\nu}}{\partial t} + u_j \frac{\partial \tilde{\nu}}{\partial x_j} = c_{b1}\left[1 - f_{t2}\right]\tilde{S}\tilde{\nu} + \frac{1}{\sigma}\left\{\nabla \cdot \left[(\nu + \tilde{\nu})\nabla\tilde{\nu}\right] + c_{b2}|\nabla\tilde{\nu}|^2\right\} \qquad (2.17) \\ - \left[c_{w1} f_w - \frac{c_{b1}}{\kappa^2} f_{t2}\right]\left(\frac{\tilde{\nu}}{d}\right)^2 + f_{t1}\Delta U^2 \end{aligned}$$

$$\nu_t = \tilde{\nu} f_{v1} \tag{2.18}$$

$$f_{v1} = \frac{\chi^3}{\chi^3 + c_{v1}^3} \tag{2.19}$$

$$f_{v2} = 1 - \frac{\chi}{1 + \chi f_{v1}} \tag{2.20}$$

$$\chi = \frac{\tilde{\nu}}{\nu} \tag{2.21}$$

$$\tilde{S} \equiv S + \frac{\tilde{\nu}}{\kappa^2 d^2} f_{v2} \tag{2.22}$$

$$f_w = g\left[\frac{1 + c_{w3}^6}{g^6 + c_{w3}^6}\right]^{1/6} \tag{2.23}$$

$$g = r + c_{w2}(r^6 - r) \tag{2.24}$$

$$r \equiv \frac{\tilde{\nu}}{\tilde{S}\kappa^2 d^2} \tag{2.25}$$

$$\tag{2.26}$$

where

$$f_{t1} = c_{t1} g_t \exp\left(-c_{t2} \frac{\omega_t^2}{\Delta U^2} [d^2 + g_t^2 d_t^2]\right) \tag{2.27}$$

$$f_{t2} = c_{t3} \exp(-C_{t4} \chi^2) \tag{2.28}$$

$$S = \equiv \sqrt{2\Omega_{ij}\Omega_{ij}} \tag{2.29}$$

$$\Omega_{ij} \equiv \frac{1}{2}\left(\frac{\partial u_i}{\partial x_j} - \frac{\partial u_j}{\partial x_i}\right) \tag{2.30}$$

$$g_t \equiv \min(0.1, \Delta U / \omega_t \Delta x) \tag{2.31}$$

The standard Spalart-Allmaras constants are as follows:

$$\sigma = 2/3$$

$$c_{b1} = 0.1355$$

$$c_{b2} = 0.622$$

$$\kappa = 0.41$$

$$c_{w1} = c_{b1}/\kappa^2 + (1 + c_{b2})/\sigma$$

$$c_{w2} = 0.3$$

$$c_{w3} = 2$$

$$c_{v1} = 7.1$$

$$c_{t1} = 1$$

$$c_{t2} = 2$$

$$c_{t3} = 1.1$$

$$c_{t4} = 2$$

2.1.4 k-ω Shear Stress Transport

k-ω SST (Shear Stress Transport) [3] is a two-equation eddy viscosity turbulence model where k is the turbulent kinetic energy and ω is the rate of kinetic energy dissipation. It is a hybrid model that becomes Wilcox k-ω [4] in the inner 50 % of the boundary layer, then transitions to k-ε in the free shear layer. The model also includes a provision to model transport of shear stress τ by assuming that τ is proportional to k.

$$\frac{\partial k}{\partial t}+\frac{\partial (U_j k)}{\partial x_j}=\tilde{P}_k-\beta^*\omega k+\frac{\partial}{\partial x_j}\left(\Gamma_k\frac{\partial k}{\partial x_j}\right) \tag{2.32}$$

$$\frac{\partial \omega}{\partial t}+\frac{\partial (U_j \omega)}{\partial x_j}=\frac{\gamma}{\rho\nu_t}P_k-\beta\omega^2+\frac{\partial}{\partial x_j}\left(\Gamma_\omega\frac{\partial \omega}{\partial x_j}\right)+(1-F_1)\,2\sigma_{\omega 2}\frac{1}{\omega}\frac{\partial k}{\partial x_j}\frac{\partial \omega}{\partial x_j} \tag{2.33}$$

$$\Gamma_k=\nu+\frac{\nu_t}{\sigma_k} \tag{2.34}$$

$$\Gamma_k=\nu+\frac{\nu_t}{\sigma_\omega} \tag{2.35}$$

$$P_k=\tau_{ij}\frac{\partial U_i}{\partial x_j} \tag{2.36}$$

$$\tilde{P}_k=\min\left(P_k;\frac{c_1\varepsilon}{\rho}\right) \tag{2.37}$$

$$\nu_t=\frac{a_1 k}{\max\left(a_1\omega; S\cdot F_2\right)} \tag{2.38}$$

where S is the magnitude of the strain rate [5]. Note that k and ω are ultimately used to calculate ν_t. Any coefficient ϕ of the model is a function of F_1, with $\phi=F_1\phi_1+(1-F_1)\,\phi_2$, with ϕ_1, ϕ_2 representing the coefficients in the k-ε and k-ω models, respectively.

$$\sigma_{k1}=1.176 \tag{2.39}$$

$$\sigma_{\omega 1}=2.000 \tag{2.40}$$

$$\kappa=0.41 \tag{2.41}$$

$$\gamma_1=0.5532 \tag{2.42}$$

$$\beta_1=0.0750 \tag{2.43}$$

$$\beta^*=0.09 \tag{2.44}$$

$$c_1 = 10 \tag{2.45}$$

$$\sigma_{k2} = 1.000 \tag{2.46}$$

$$\sigma_{\omega 2} = 1.168 \tag{2.47}$$

$$\gamma_2 = 0.4403 \tag{2.48}$$

$$\beta_2 = 0.0828 \tag{2.49}$$

F_1 is a blending function which is equal to 1 near the wall, then decreases to 0 in the outer half of the boundary layer and into the free shear layer. This facilitates the transition from Wilcox k-ω ($F_1 = 1$) to k-ε ($F_1 = 0$).

$$F_1 = \tanh\left(arg_1^4\right) \tag{2.50}$$

$$arg_1 = \min\left(\max\left(\frac{\sqrt{k}}{\beta^*\omega\gamma}; \frac{500\nu}{\gamma^2\omega}\right); \frac{4\rho\sigma_{\omega 2}k}{CD_{k\omega}y^2}\right) \tag{2.51}$$

$$CD_{k\omega} = \max\left(2\rho\sigma_{\omega 2}\frac{1}{\omega}\frac{\partial k}{\partial x}\frac{\partial \omega}{\partial x_j}; 1.0e{-}10\right) \tag{2.52}$$

$$F_2 = \tanh\left(arg_2^2\right) = \max\left(2\frac{\sqrt{k}}{\beta^*\omega y}; \frac{500\nu}{y^2\omega}\right) \tag{2.53}$$

$$arg_2 = \max\left(2\frac{\sqrt{k}}{\beta^*\omega y}; \frac{500\nu}{y^2\omega}\right) \tag{2.54}$$

$$\tau_{ij} = \nu_t\left(\frac{\partial U_i}{\partial x_j} + \frac{\partial U_j}{\partial x_i} - \frac{2}{3}\frac{\partial U_k}{\partial x_k}\right) - \frac{2}{3}k\delta_{ij} \tag{2.55}$$

k-ω SST has several benefits over its constitutive models. Wilcox k-ω performs better in adverse pressure gradient flows than k-ε, which over-predicts τ and delays separation. For this reason, k-ω SST uses Wilcox k-ω in the inner boundary layer. However, unlike Wilcox k-ω, the behavior of k-ω SST in the boundary layer is insensitive to freestream values of ω. k-ω SST transitions to k-ε in the free shear layer because k-ε performs well there. Wilcox k-ω can predict spreading rates incorrectly in the free shear layer. Finally, k-ω SST does better in adverse pressure gradient flows than Wilcox k-ω because it accounts for shear stress transport effects, unlike eddy viscosity

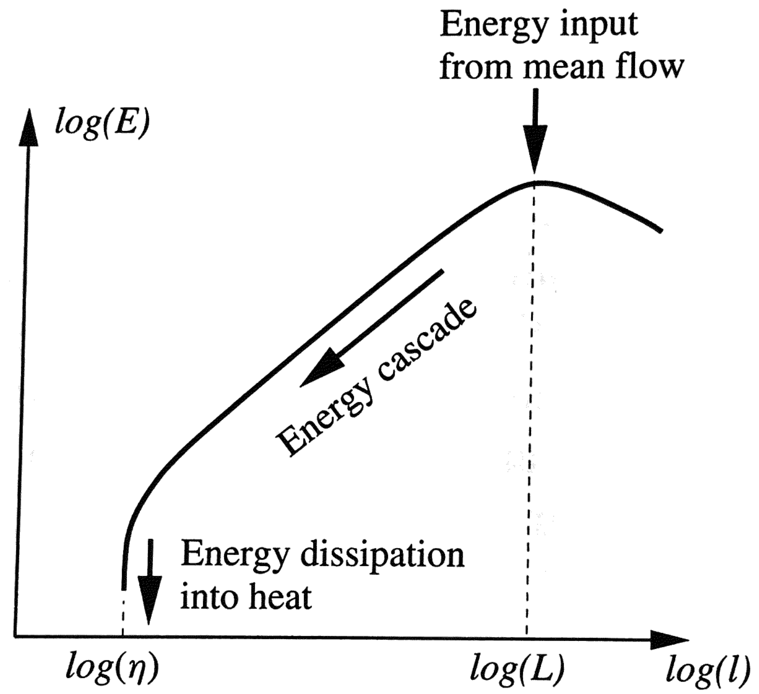

Figure 2.1: Turbulent kinetic energy cascades from the inertial to dissipative length scales. (source: [1])

models.

2.1.5 Large Eddy Simulation

As discussed in Section 2.1.1, turbulent flows contain eddies with a spectrum of length scales. The largest eddies, that belong to the energy input and inertial ranges of scales, contain nearly all the kinetic energy. They are non-isotropic and directly influence the flow momentum. According to Kolmogorov's self-similarity hypothesis, the smallest length scales, called the dissipative length scales, are statistically isotropic. Their only contribution is to dissipate kinetic energy to heat. The large eddies break down into smaller eddies, transferring kinetic energy down the length scales and eventually to heat. This is known as the turbulent kinetic energy cascade, shown in Figure 2.1.

As demonstrated in Section 2.1.1, it is too computationally expensive to resolve the Kolmogorov microscale. Large Eddy Simulation (LES) attempts to overcome this by not resolving the smallest eddies, instead modeling their energy dissipation. The important inertial length scales

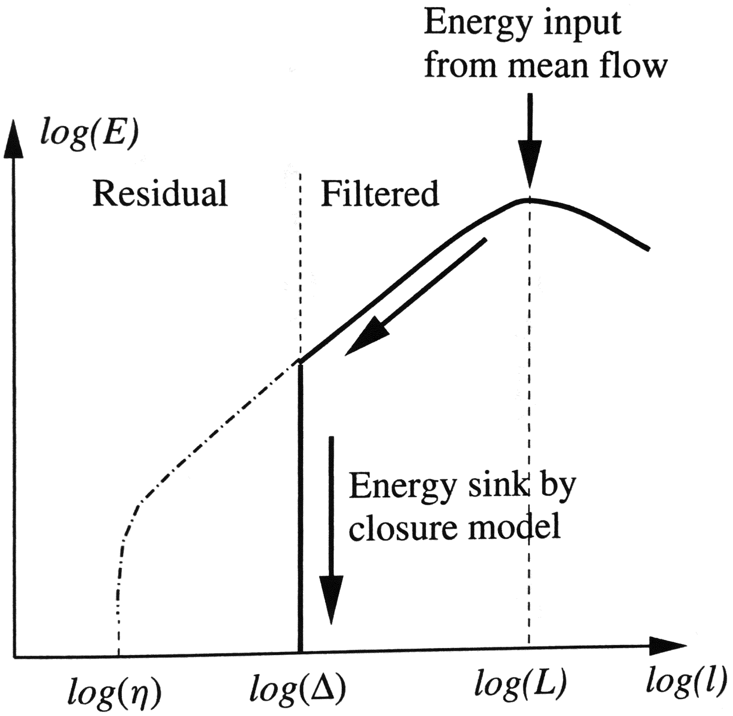

Figure 2.2: LES truncates the turbulent energy cascade at the filter length Δ. (source: [1])

can then be resolved with a larger cell size, resulting in a lower cell count. This is demonstrated in Figure 2.2.

To accomplish this, the velocity and pressure field are filtered into resolved and unresolved portions.

$$u_i = \bar{u}_i + u_i' \tag{2.56}$$

$$p = \bar{p} + p' \tag{2.57}$$

The filter function is applied as

$$\bar{u}(x,t) \equiv \int G(r,x)\, u(x-r,t)\, dr \tag{2.58}$$

A box filter is typically used as shown in Figure 2.3. Δ is taken to be the local cell size. Applying

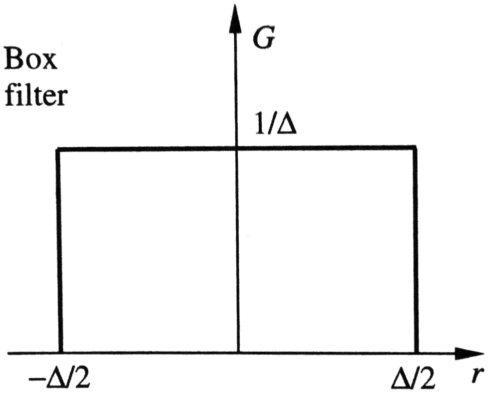

Figure 2.3: A box filter with length Δ. (source: [1])

the filter to the incompressible Navier-Stokes equations yields [6], [7]

$$\frac{\partial \bar{u}_i}{\partial x_i} = 0 \tag{2.59}$$

$$\rho \frac{\partial \bar{u}_i}{\partial t} + \rho \frac{\partial}{\partial x_j}\left(\bar{u}_i \bar{u}_j\right) = -\frac{\partial \bar{p}}{\partial x_i} + \mu \bigtriangledown^2 \bar{u}_i - \frac{\partial \tau_{ij}}{\partial x_j} \tag{2.60}$$

Where $\tau_{ij} = \rho \overline{u_i u_j} - \rho \bar{u}_i \bar{u}_j$ is the subgrid scale (SGS) stress tensor resulting from the filtering operation. Like the Reynold's stress, the SGS stress uses an eddy viscosity model

$$\tau_{ij} = \frac{1}{3}\tau_{ii}\delta_{ij} - 2\mu_t \bar{S}_{ij} \tag{2.61}$$

where $\bar{S}_{ij} = \frac{1}{2}\left(\frac{\partial \bar{u}_i}{\partial x_j} + \frac{\partial \bar{u}_j}{\partial x_i}\right)$ is the filtered strain rate tensor, and μ_t is the eddy viscosity. LES uses the Smagorinsky model [7]

$$\mu_t = \rho (C_S \Delta)^2 |\bar{S}| \tag{2.62}$$

where Δ is the filter width and C_S is the empirical Smagorinsky constant.

We can estimate the required cell count using the Taylor microscale. The Taylor microscale is the length scale below which the eddies are significantly affected by fluid viscosity, which is the dissipative range. The Taylor microscale can be approximated as

$$\lambda = \sqrt{10}\eta^{2/3}L^{1/3} \approx 3.2\,\mathrm{mm} \tag{2.63}$$

Then the estimated cell count is

$$N^3 \approx \left(\frac{L}{\lambda}\right)^3 \sim 10^8. \tag{2.64}$$

Such a simulation would be computationally expensive but obtainable in a research setting. LES may see mainstream automotive aerodynamics CFD use within 5 to 10 years due to ever-increasing computational power.

2.1.6 Detached Eddy Simulation

Detached Eddy Simulation (DES) is a hybrid approach that uses Spalart-Allmaras RANS to model attached, small scale eddies in near wall regions, then switches to LES in detached regions away from the wall, where large scale eddies can be resolved. Spalart-Allmaras is also used as the SGS stress eddy viscosity model in this formulation, by replacing wall distance d_w in the Spalart-Allmaras RANS model with $\tilde{d_w}$ [8]

$$\tilde{d_w} \equiv \min\left(d_w, C_{DES}\Delta\right). \tag{2.65}$$

DES switches from RANS to LES once $d_w > C_{DES}\Delta$. By relying on wall distance and grid size, the LES zones need not be known *a priori*.

2.1.7 Delayed Detached Eddy Simulation

Occasionally, DES improperly switches to an LES zone when the grid size is ambiguous. The grid size is ambiguous when the grid size is fine enough that $d_w > C_{DES}\Delta$ in the boundary layer, yet the grid size is still too coarse for a properly resolved LES [9]. The eddy viscosity is reduced as the model switches from RANS to LES mode, however the grid is not fine enough to resolve the velocity fluctuations present in LES to replace the modeled viscosity. Shear stress then drops, a phenomenon called Modeled Stress Depletion (MSD)[9] . Artificially low shear stress in the boundary layer can then lead to premature flow separation, called Grid Induced Separation (GIS) [9]. This is a top concern for vehicle aerodynamic flows where separation is a critical. In [9], a new version of DES is proposed called Delayed Detached Eddy Simulation (DDES) to address this issue.

$$l_{ddes} = d_w - f_d \max\left(0, d_w - C_{DES}\Delta\right) \tag{2.66}$$

$$f_d = 1 - \tanh\left|(8r_d)^3\right| \tag{2.67}$$

$$r_d = \frac{\nu + \nu_t}{\kappa^2 d_w^2 \sqrt{\left(\frac{\partial U_i}{\partial x_j}\right)^2}} \tag{2.68}$$

l_{DDES} is the DDES length scale, and f_d is the delaying function. r_d is the same quantity from the Spalart-Allmaras model, which is has the value of 1 at the wall and 0 in the free shear flow. By redefining the limiter in this way, RANS can be preserved in the boundary layer while still allowing the switch to LES in the appropriate regions.

2.1.8 Improved Delayed Detached Eddy Simulation

Improved Delayed Detached Eddy Simulation (IDDES) is another hybrid model proposed in [10] that extends the capability of DDES to Wall-Modeled LES (WMLES) applications. It also provides a flexible, variable subgrid length scale, Δ. In LES, Δ is a function purely of the grid size. This is problematic because the appropriate value of Smagorinsky constant then varies in different regions of the flow. IDDES redefines Δ to be

$$\Delta = \min\left\{\max\left[C_w d_w, C_w h_{max}, h_{wn}\right], h_{max}\right\}. \tag{2.69}$$

C_w is an empirical constant which does not have to change throughout the flow, and h_{wn} is the grid spacing in direction normal to the wall. Δ was chosen to satisfy

$$\Delta_{free} = h_{max} \equiv \max\left\{h_x, h_y, h_z\right\} \tag{2.70}$$

$$\Delta_{wall} = \Delta\left(h_x, h_z\right). \tag{2.71}$$

Δ_{free} follows the suggestions of [9] to use the maximum grid spacing, which is acceptable because cells far away from the wall should be fairly isotropic. Near the wall, Δ depends only on the x and z cell spacings. Recall the length scales used in the DDES model,

$$l_{RANS} = d_w \tag{2.72}$$

$$l_{LES} = C_{DES}\Psi\Delta \tag{2.73}$$

$$l_{DDES} = l_{RANS} - f_d \max\left\{0, l_{RANS} - l_{LES}\right\}. \tag{2.74}$$

Where Ψ is a low-Re correction term,

$$\Psi^2 = \min\left[100, \frac{1 - \frac{c_{b1}}{c_{w1}\kappa^2 f_w^*}\left[f_{t2} + \left(1 - f_{t2}\right) f_{v2}\right]}{f_{v1}\max\left(10^{-10}, 1 - f_{t2}\right)}\right]. \tag{2.75}$$

Define a new length scale for WMLES as

$$l_{WMLES} = f_B\left(1 + f_e\right) l_{RANS} + \left(1 - f_B\right) l_{LES}. \tag{2.76}$$

The first blending function is intended as a switch between RANS and LES modes,

$$f_B = \min\left\{2\exp\left(-9\alpha^2\right), 1.0\right\} \tag{2.77}$$

$$\alpha = 0.25 - d_w/h_{max}. \tag{2.78}$$

The model transitions from RANS to LES within d_w less than one local h_{max} of the wall. The second function f_e is intended to prevent log layer mismatch of Reynold's stresses.

$$f_e = \max\{(f_{e1} - 1), 0\} \Psi f_{e2} \tag{2.79}$$

$$f_{e1}(d_w/h_{max}) = \begin{cases} 2\exp\left(-11.09\alpha^2\right), & \text{if } \alpha \geq 0 \\ 2\exp\left(-9\alpha^2\right), & \text{if } \alpha < 0 \end{cases} \tag{2.80}$$

$$f_{e2} = 1.0 - \max\{f_t, f_l\} \tag{2.81}$$

$$f_t = \tanh\left[\left(c_t^2 r_{dt}\right)^3\right] \tag{2.82}$$

$$f_l = \tanh\left[\left(c_t^2 r_{dl}\right)^{10}\right] \tag{2.83}$$

$$r_{dt} = \frac{\nu_t}{\kappa^2 d_w^2 \max\left\{\left[\sum_{ij}\left(\partial u_i/\partial x_j\right)^2\right]^{1/2}, 10^{-10}\right\}} \tag{2.84}$$

$$r_{dl} = \frac{\nu}{\kappa^2 d_w^2 \max\left\{\left[\sum_{ij}\left(\partial u_i/\partial x_j\right)^2\right]^{1/2}, 10^{-10}\right\}} \tag{2.85}$$

In order to combine the DDES and WMLES, a new blending function $\tilde{f}_d$ is defined

$$\tilde{f}_d = \max\{(1 - f_{dt}), f_B\} \tag{2.86}$$

where

$$f_{dt} = 1 - \tanh\left[(8r_{dt})^3\right], \tag{2.87}$$

then l_{DDES} is redefined as

$$\tilde{l}_{DDES} = \tilde{f}_d l_{RANS} + \left(1 - \tilde{f}_d\right) l_{LES} \tag{2.88}$$

Finally, a hybrid length scaled can be defined by combining the definitions

$$l_{hyb} = \tilde{f}_d (1 + f_e) l_{RANS} + \left(1 - \tilde{f}_d\right) l_{LES} \tag{2.89}$$

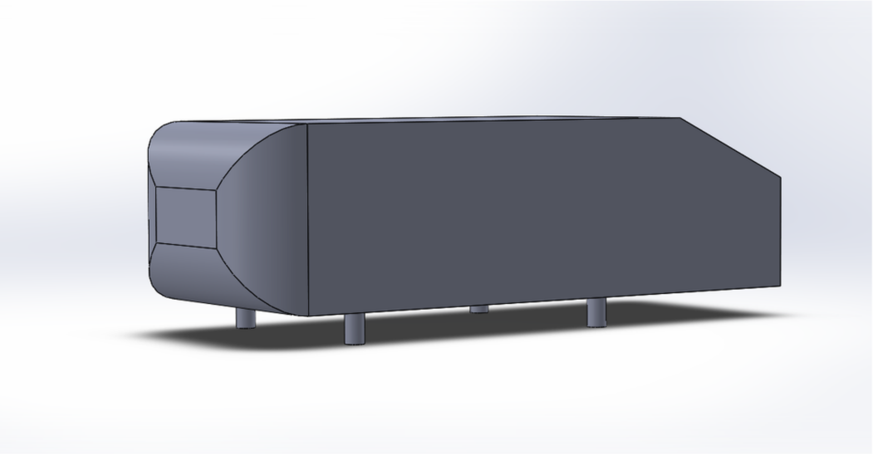

Figure 2.4: The Ahmed Body used for studying simple bluff body aerodynamics. (source: https://grabcad.com/library/ahmed-body-2)

2.2 Applied Automotive Aerodynamics

For automotive aerodynamicists, finding a model geometry for detailed study and experimentation is a non-trivial problem. While there is no shortage of real automobiles, they have many complex flow features due to myriad components in the hood and underbody, small gaps, seals, and cooling openings, which makes them difficult to study in a research setting. Fast product development cycles prevent automotive manufacturers from spending much time on a single design, and industry secrecy further disinclines them from sharing. Research has been done on simplified bluff bodies such as the Ahmed Body [11], which is useful for understanding some basic flow phenomenon; however the results are ultimately limited because it lacks many of the key features that characterize a vehicle aerodynamic flow. Besides its somewhat rounded front end and a backward-facing ramp on the back, the Ahmed Body doesn't much resemble an automobile at all, see Figure 2.4. Aerodynamicists needed a model to fill the gap between overly-simplified shapes and too-detailed real vehicles. To this end, the DrivAer model was created with the help of car manufacturers to study the more salient features of automotive aerodynamics [12]. The shape is based on a genericized car, available with three distinct rear end shapes: fastback, notchback, and estate. The model geometry was based off two real vehicles; the Audi A4 and the BMW 3-series

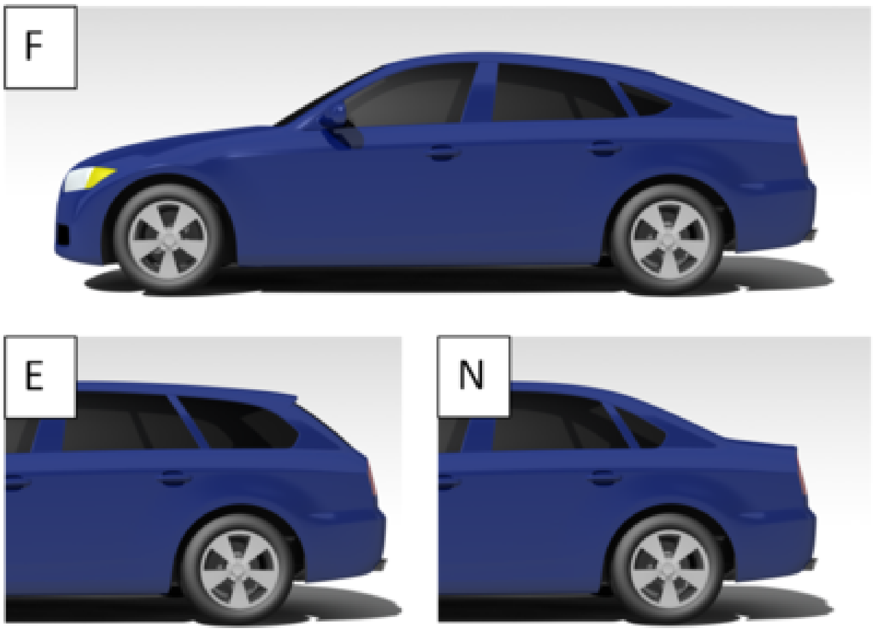

Figure 2.5: The DriAer simplified car model can switch between three rear shapes. (source: http://www.aer.mw.tum.de/en/research-groups/automotive/drivaer/)

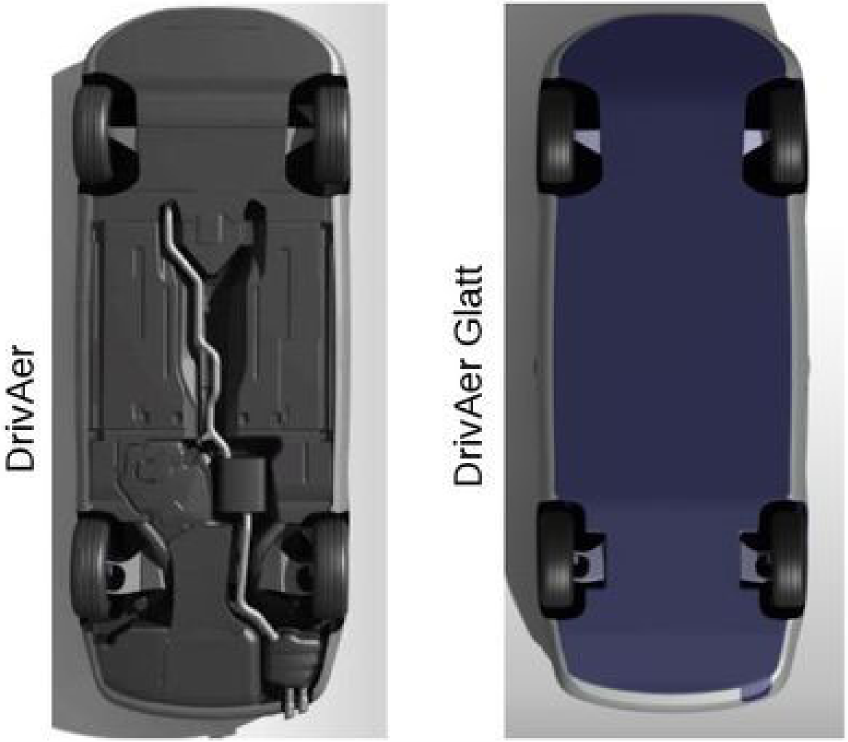

Figure 2.6: The DriAer model underbody is configurable between smooth or detailed. (source: https://www.aer.mw.tum.de/en/research-groups/automotive/drivaer/)

cars. As seen in Figures 2.5 and 2.6, the vehicle shape is highly realistic, and the model has A- through D-pillars, mirrors, and wheel openings. The underbody is simplified, retaining the larger components that affect the flow while doing away with small, unimportant details. The DrivAer model is thus an inspiration for the simple truck shape.

The application of hybrid RANS-LES turbulence models for automotive aerodynamics has been studied before. In [13], the authors used a similar methodology to this paper – transient DES simulation using the OpenFOAM toolbox – on several Volkswagen Group vehicles and a high simplified car shape called the Volkswagen Red Model. The vehicles tested in a wind tunnel and the results were compared to CFD. The authors found generally good agreement between overall force coefficients, as well as between the CFD-predicted surface c_p and pressure taps on the vehicle. However, the CFD struggled to predict force coefficients on vehicles with sloped and/or rounded rear shapes. CFD was not predicting the adverse pressure gradient-driven flow separation on these surfaces correctly, leading to insufficient pressure recovery and consistently overpredicted C_{lr} and C_d. The authors also compared the surface flow topology between simulation and experiment using oil streaks, and found large scale agreement.

In [14], a similar study was undertaken by comparing three different hybrid RANS-LES turbulence models on an Audi A1 car to wind tunnel results. The models were: Partially-Averaged Navier Stokes (PANS), Delayed Detached Eddy Simulation (DDES), and Very Large Eddy Simulation (VLES). The paper found similar results to [13], with some discrepancies observed in C_l and large scale agreement in surface flow topology.

CHAPTER III: MODEL SETUP

3.1 Mesh

CFD results are only as good as the mesh they were computed on. A well-designed mesh uses cell count effectively, increasing resolution where there are gradients to resolve, and decreasing where it is not needed for faster run time. The mesh must have sufficient quality, with cell skewness, aspect ratio, and non-orthogonality under the acceptable limits. The surface mesh needs to capture the geometry surface with sufficient fidelity, including gaps and edges. The entire model must have a prism layer mesh with the correct first cell height, growth ratio, and total thickness to resolve the boundary layer behavior. Critically, the mesh needs to properly resolve the boundary layer with an appropriate total layer thickness, growth rate, and a first cell height that yields the desired y^+ values. y^+ is the dimensionless wall distance defined as

$$y^+ = \frac{u_\tau y}{\nu}, \tag{3.1}$$

where y is the actual wall distance, ν is the kinematic eddy viscosity, and u_τ is the wall friction velocity,

$$u_\tau = \sqrt{\frac{\tau_w}{\rho}}. \tag{3.2}$$

The dimensionless velocity u^+ is defined as

$$u^+ = \frac{u}{u_\tau} \tag{3.3}$$

The flow velocity u^+ is prescribed near the wall by Law of the Wall, shown in Figure 3.1. According to Law of the Wall, $u^+ = y^+$ in the viscous sublayer where $0 < y^+ < 5$. $5 < y^+ < 30$ is the buffer layer where u^+ is unknown. Finally, $30 < y^+ < 200$ is the log layer, where u^+ is prescribed as

$$u^+ = \frac{1}{\kappa} log(y^+) + C. \tag{3.4}$$

C is a constant approximately equal to 5.1 for smooth walls and $\kappa = 0.41$ is the von Kármán

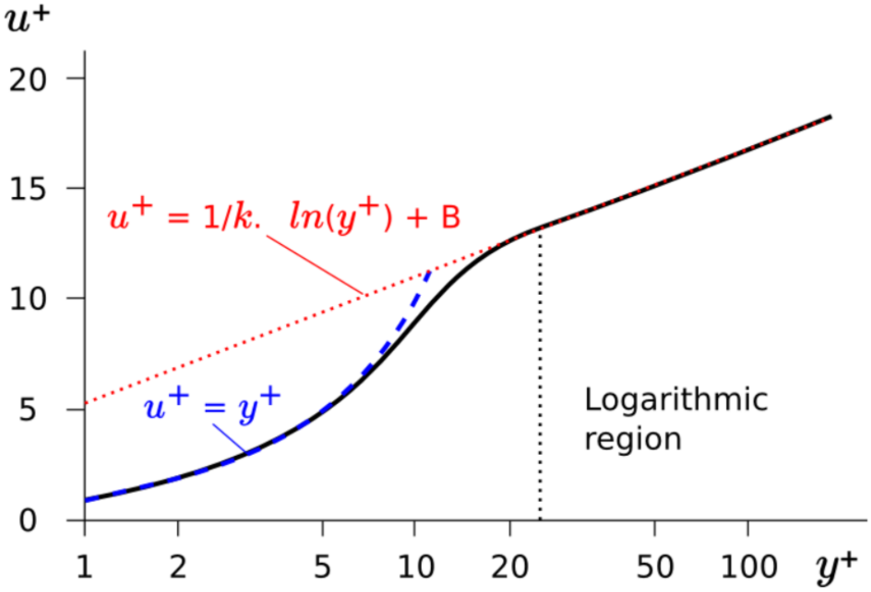

Figure 3.1: Law of the Wall (source: https://www.cfd-online.com/Wiki/Law_of_the_wall))

constant. In order to prescribe the correct u^+ near the wall, the y^+ of the first cell must be either in the viscous sublayer or the log layer. Due to the high Reynold's Number ($Re \approx 8.1e6$) of this flow, a y^+ in the log layer is targeted to keep cell count reasonable.

For volumetric mesh refinement, the mesh is left coarse far away from the vehicle, where the flow is largely uniform. The mesh is then refined in blocks with decreasing distance to the vehicle. Some of the refinement zones extended multiples of vehicle length downstream to capture the decay of the wake into the freestream flow. Finally, the mesh near the wall consists of thin, higher aspect ratio cells to resolve boundary layer behavior as previously discussed, see Figure 3.4.

The last matter is to perform a mesh independence study to ensure the domain is sufficiently

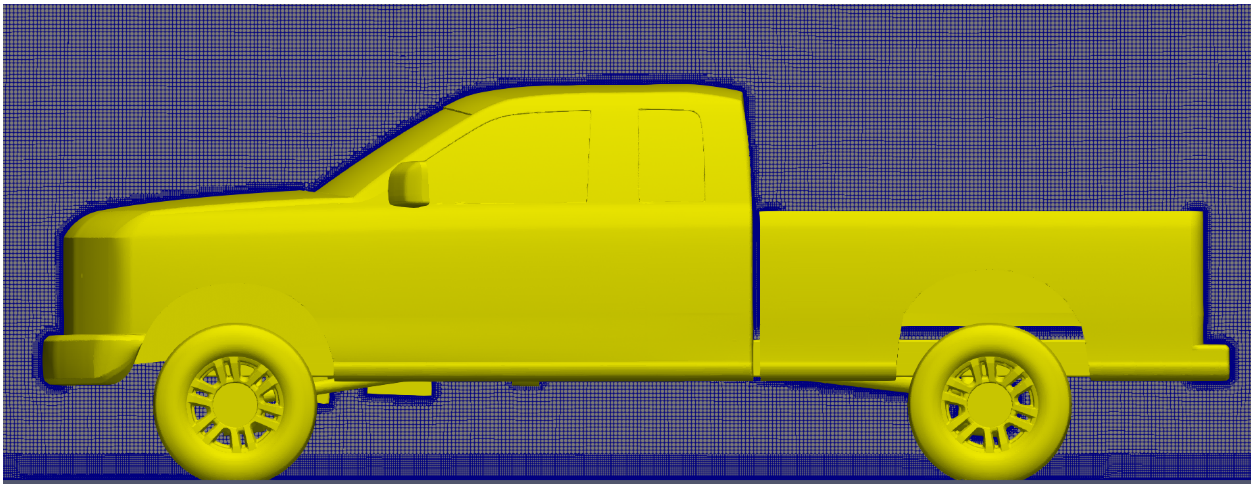

Figure 3.2: Mesh near the truck, side view

Base mesh size	C_d	C_l	Cell count
3.5 m	0.551	0.342	18×10^6
2.5 m	0.552	0.345	41×10^6
2.0 m	0.551	0.347	71×10^6
1.5 m	0.553	0.335	147×10^6

Table 3.1: Mesh convergence study averaged force coefficients

refined. This is done by globally decreasing the mesh size by multiples until the solution no longer changes significantly. To accomplish this, the mesh size is defined as follows. The largest cell size in the model is called the base size, and all smaller sizes are defined by multiples of the base size as

$$\text{refinement}_n = (\text{base size})\left(\frac{1}{2}\right)^n, \tag{3.5}$$

where n is called the refinement level. By defining mesh size in this way, it is easy to globally change refinement while not changing the topology of the mesh. Table 3.1 shows the results of varying the base mesh size. C_d and C_l vary by less than 1 and 5 percent, respectively, demonstrating acceptable mesh convergence for this study. From these results, a base mesh size of 2.0 m was chosen. For this mesh, the surface size is 4 mm, and the first cell height is 0.5 mm.

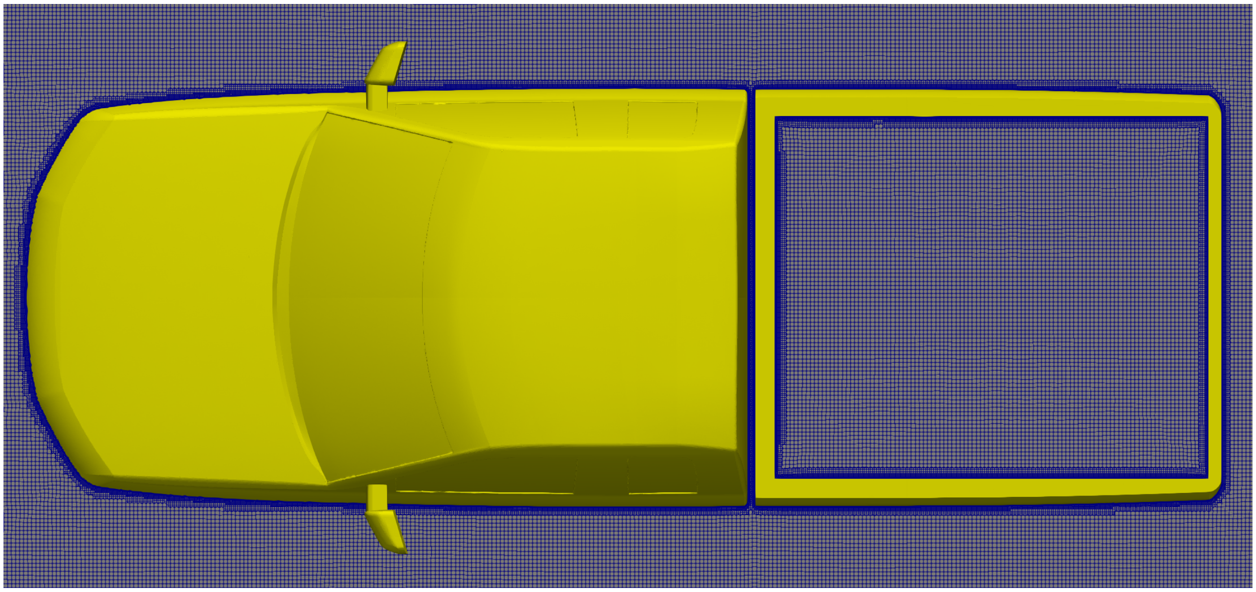

Figure 3.3: Mesh near the truck, top view

3.2 Geometry

The geometry tested has the profile of a simplified truck. Small details present on real trucks, such as door handles, body lines, panel gaps, and various underbody components are eliminated, whereas important features were made to be representative of a real truck. These include: the shape of the A-pillar, tumblehome, rear header taper, cargo box boattailing, box height, and windshield angle. The overall dimensions of the truck, such as wheelbase, box length, cab length, and roof height were also chosen to be representative of contemporary trucks. This strategy has a few benefits. First, simplifying the vehicle makes it easier to mesh and lowers cell count, easing numerical convergence and decreasing simulation time. Second, the extra features introduce noise into the solution: small flow features which we aren't really interested in, and vary from truck to truck. We want to narrow the scope and focus on the characteristic aerodynamic features of a truck - vortices rolling off the A-pillars, flow off the rear header, downwash into the bed, and so forth - and how the choice of turbulence model affects them. Finally, it is important the vehicle is not so simplified that the flow is not representative of a real truck. Some simple models are useful for

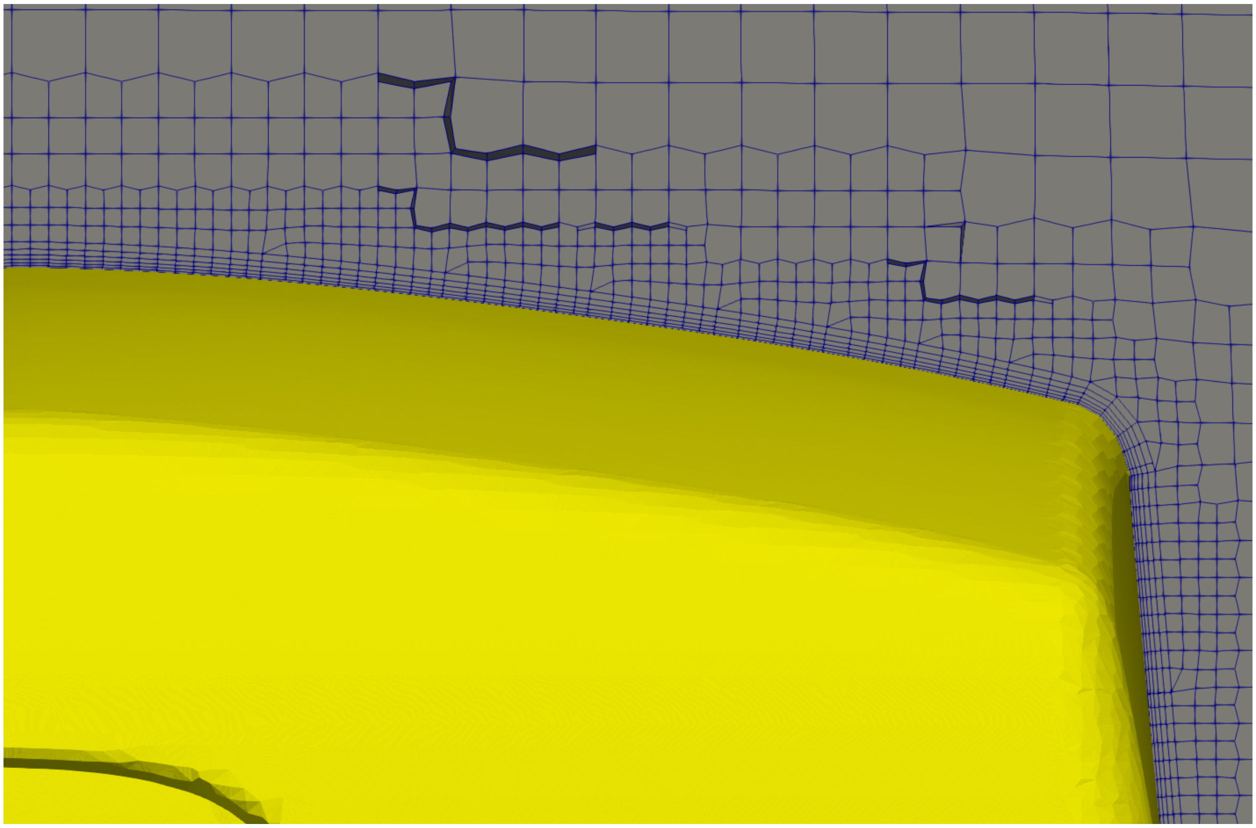

Figure 3.4: Prism layer mesh for resolving the boundary layer

studying specific aerodynamic phenomenon such as the Ahmed Body, which is used to study the relationship between backlite angle, flow separation, and wake behavior for a bluff body but are do not capture the true shape of a vehicle, and all of its interacting features. The Drivair Model [12] is an example of a full featured simplified car model, which also has interchangeable back ends (hatchback, wagon, and sedan). The front end of the pickup model includes A-pillar and roof offsets, and roof and hood lead-edges are radiused. All cooling openings are closed, as seen in Figure 3.5. The model underbody includes a smoothed floorpan and rocker offsets. Engine bay is open from the bottom, and the model has a simplified engine, transmission, driveline, exhaust, and frame, as shown in Figure 3.6. The model has B- and C-pillar offsets that are radiused. The roof rear header has curvature. The wheel base, roof height, box length, and cab length are representative of a production vehicle. The tires are smooth and intersected 30 mm into the ground (Figures

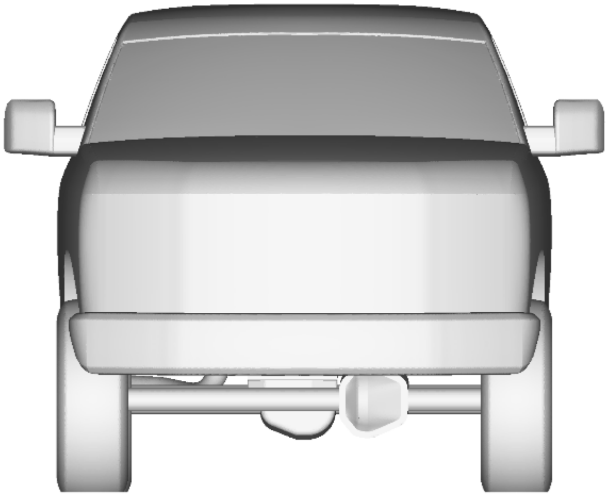

Figure 3.5: Front view of simplified truck

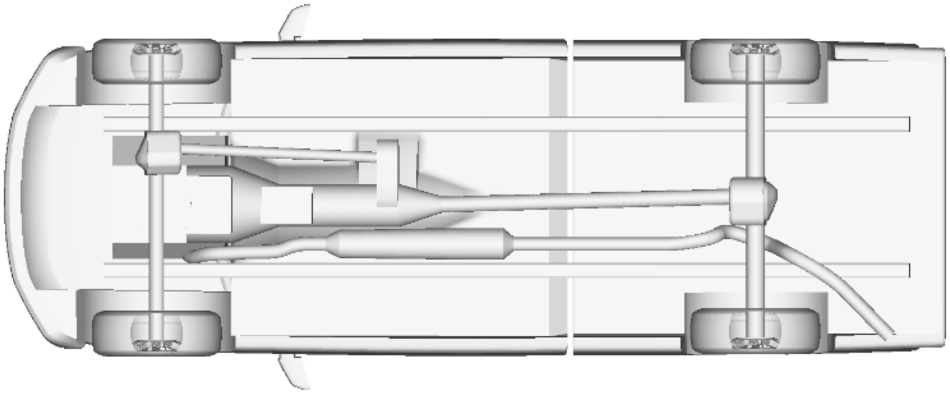

Figure 3.6: Underbody view of simplified truck

3.7 and 3.8).

3.3 Initial and Boundary conditions

Both the steady state and transient simulations were initialized using the OpenFOAM solver potentialFoam, which solves the potential flow equation. The flow is assumed inviscid and irrotational, so then velocity $\vec{u}$ is a function of velocity potential ϕ

$$\vec{u} = \bigtriangledown \phi . \tag{3.6}$$

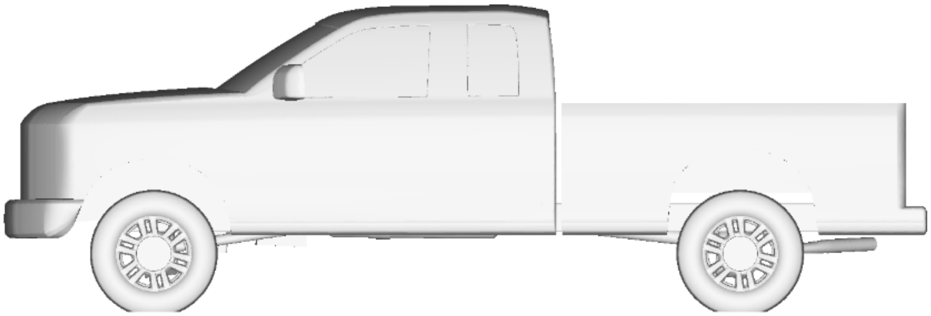

Figure 3.7: Side view of simplified truck

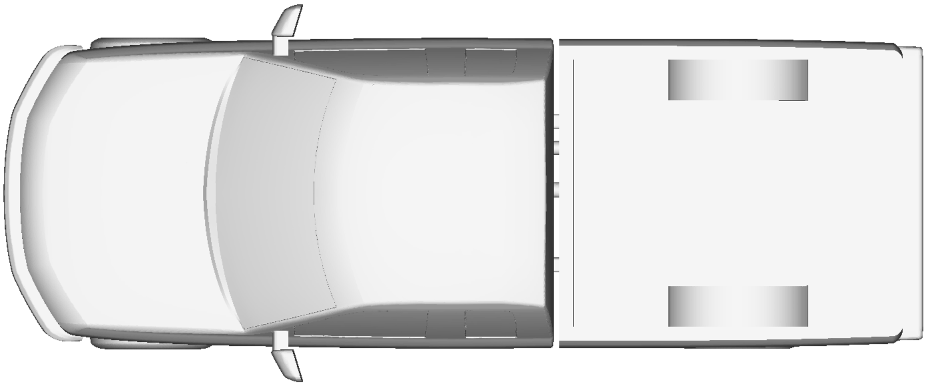

Figure 3.8: Top view of simplified truck

By the continuity equation, ϕ must then satisfy the Laplace equation

$$\bigtriangledown \cdot (\bigtriangledown \phi) = \bigtriangledown^2 \phi = 0. \tag{3.7}$$

The flow domain is simulated as a simple, large box wind tunnel. The model is centered in the domain, which is sized to have a low blockage ratio, and the model is located multiple vehicle lengths away from the domain walls. The freestream enters normal through the inlet to yield a Reynold's Number of approximately 8.1×10^6 , using the model wheelbase as the characteristic length scale. The inlet and outlet faces have special boundary conditions for velocity and pressure intended to prevent backflow and achieve the target flow rate through the domain. The other walls of the domain and the pickup model surface have symmetry boundary conditions for pressure.

The floor has a translating velocity boundary condition to simulate the road moving under the vehicle as it travels at the freestream velocity. The other walls of the domain parallel to the floor have slip velocity boundary conditions. The vehicle body has a no-slip velocity boundary condition everywhere except for the wheels, which have rotating velocity boundary conditions corresponding to their respective angular velocities.

3.4 Navier-Stokes solvers

Two different OpenFOAM solvers were used in this study: SIMPLEC (Semi-Implicit Method for Pressure-Linked Equations Consistent) for steady problems, and PISO (Pressure Implicit with Splitting Operators) for transient problems. Both are semi-implicit pressure projection methods. Starting from a solution at time step n with u^n, p^n, the next time step u^{n+1}, p^{n+1} must be calculated. Rearrange the Navier-Stokes equations as

$$\frac{u^{n+1}-u^n}{\Delta t} = -\frac{1}{\rho} \bigtriangledown p^{n+1} - N\left(u^n, u^n\right) + \nu \bigtriangledown^2 u^{n+1} + f^{n+1} \tag{3.8}$$

$$\bigtriangledown \cdot u^{n+1} = 0, \tag{3.9}$$

where $N\left(u^n, u^n\right)$ are the advection terms [1]. By taking the divergence of the momentum equation, we obtain the pressure equation

$$\bigtriangledown^2 p^{n+1} = -\rho \bigtriangledown \cdot \left(-N\left(u^n, u^n\right) + \nu \bigtriangledown^2 u^{n+1} + f^{n+1}\right), \tag{3.10}$$

which is really just the Poisson equation. Rewrite the pressure field as

$$p^{n+1} = p^n + \delta p, \tag{3.11}$$

where δp is the pressure correction. The predictor step of the method calculates the intermediate velocity u^*

$$u^* = u^n + \Delta t \left(-N(u^n, u^n) + \nu \bigtriangledown^2 u^{n+1} + f^{n+1} \right) - \frac{\Delta t}{\rho} \bigtriangledown p^n. \tag{3.12}$$

Because u^* is only a prediction, δp is omitted in order to split the p and u fields. Then, the pressure equation is solved using u^* and δp

$$\bigtriangledown^2 \delta p = \frac{\rho}{\Delta t} \bigtriangledown \cdot u^*. \tag{3.13}$$

Finally, the corrector step updates the u field [1]

$$u^{n+1} = u^* - \Delta t \bigtriangledown \delta p. \tag{3.14}$$

These methods are called semi-implicit because the predictor step is implicit, while the corrector step is explicit. The SIMPLEC and PISO algorithms follow this general procedure, but operate on the discretized and linearized equations. The momentum equation in this form is written

$$a_P(u^{(m)}) u^*_{i,P} + \sum_l a_{l,P}(u^{(m)}) u^*_{i,l} = Q_P(u^{(m)}) - \left(\frac{\delta p^{(m)}}{\delta x_i} \right), \tag{3.15}$$

where P represents the value at cell P, l represents the contributions from the neighboring cells, and Q_P are the right hand side terms. The first step of SIMPLEC and PISO is to evaluate a_P, $a_{l,P}$, and Q_P at the current time layer. Then use these coefficients to obtain u^*_i from the linearized momentum equation. The values of u and p at the next time layer are represented as

$$u_i^{(m+1)} = u^* + u'_i \tag{3.16}$$

$$p_i^{(m+1)} = p^* + p'_i. \tag{3.17}$$

The next step is to solve the pressure equation

$$\frac{\delta}{\delta x_i}\left(\frac{1}{a_P(u^{(m)})}\frac{\delta p'}{\delta x_i}\right) = \left(\frac{\delta u_i^*}{\delta x_i}\right) + \left(\frac{\delta \tilde{u}_i'}{\delta x_i}\right), \tag{3.18}$$

where $\tilde{u}_i'$ is an unknown function defined by

$$\tilde{u}_{i,P}' = u_{i,P}' + \frac{1}{a_P(u^{(m)})}\left(\frac{\delta p'}{\delta x_i}\right). \tag{3.19}$$

SIMPLEC approximates $\tilde{u}_{i,P}'$ using

$$\tilde{u}_{i,P}' \approx u_{i,P}'\frac{\sum_l a_{l,P}(u^{(m)})}{a_P(u^{(m)})}. \tag{3.20}$$

After solving the pressure equation, solve for velocity corrector

$$u_{i,P}' = -\frac{1}{a_P(u^{(m)})}\left(\frac{\delta p'}{\delta x_i}\right), \tag{3.21}$$

then the next time layer $u^{(m+1)}$ and $p^{(m+1)}$ can be calculated. SIMPLEC repeats these steps until convergence is reached.

The PISO algorithm differs slightly from SIMPLEC. When solving the pressure equation, the $\tilde{u}_{i,P}'$ term is dropped. $\tilde{u}_{i,P}'$ is instead calculating using the relationship

$$\tilde{u}_{i,P}' = -\frac{\sum_l a_{l,P}(u^{(m)})u_{i,l}'}{a_P(u^{(m)})}, \tag{3.22}$$

and then solving for a second pressure correction

$$\frac{\delta}{\delta x_i}\left(\frac{1}{a_P(u^{(m)})}\frac{\delta p''}{\delta x_i}\right)_P. \tag{3.23}$$

Simulation type	Steady-state	Transient
Solver	simplecFoam	pisoFoam
Total time	6000 s	4.0 s
Time step	1 s	2×10^{-4} s

Table 3.2: OpenFOAM solvers and time settings

Operator	Scheme
Gradient	Gauss Linear
Divergence	Gauss Upwind
Laplacian	Gauss Linear

Table 3.3: Finite volume schemes

Finally, use the second pressure correction to obtain a second velocity correction

$$u'' = \tilde{u}'_{i,P} - \frac{1}{a_P(u^{(m)})}\left(\frac{\delta p''}{\delta x_i}\right)_P . \tag{3.24}$$

The time step and total amount of simulated time for each simulation type are shown in Table 3.2. The steady-state time steps are much larger because the solver aims to obtain only the steady-state solution, rather than being time-accurate like the transient solver.

3.5 Finite volume schemes

With the finite volume approach, each integral term in the Navier-Stokes equations must be discretized. There are three types of operators to discretize: gradient, divergence, and Laplacian. The schemes are summarized in Table 3.3. ”Gauss” indicates the use of Divergence Theorem to transform each volume integral into a surface flux integral. The next term indicates the interpolation scheme used to obtain the cell face values for the surface flux integral. Linear interpolation is equivalent to central differencing, and upwind interpolation is a simple backward difference [15].

Variable	Solver
p	Geometric Algebraic Multigrid
U	Biconjugate Gradient Stabilized
$\tilde{\nu}_t$	Biconjugate Gradient Stabilized
k	Biconjugate Gradient Stabilized
ε	Biconjugate Gradient Stabilized
ω	Biconjugate Gradient Stabilized

Table 3.4: Linear solver schemes

3.6 Linear solvers

The reason for linearizing and discretizing the Navier-Stokes equations is so that they can be recast into various linear systems which can be solved. Due to the large size of the matrices involved, at minimum $n \times n$ where n is the number of cells, direct methods are infeasible. Efficient, iterative linear solver algorithms are required. These standard OpenFOAM linear solvers [15] used throughout the simulation are summarized in Table 3.4.

CHAPTER IV: RESULTS

4.1 Numerical convergence

To test the numerical convergence of each model, the values of C_d and C_l are monitored over time until they settle into a pattern around a mean value. Additionally, the solution residuals are monitored to ensure the linear solvers are converging. The mean flow fields are used to compare the steady and transient runs. For transient runs, the solution is time-averaged from a certain point until the end time, with a large enough window to capture all periods of oscillation in the solution. For steady state runs, the latest time step is typically used; however, because the solution still oscilliates strongly, it too is time-averaged over an interval. This is due to the inherently unsteady nature of the flow. The steady state runs were averaged from time step 4000 to 6000, and the transient runs from 2.0 s to 4.0 s. Figures 4.1 through 4.10 show that each turbulence model achieved convergence in C_d and C_l. The RANS models converged within +/- 0.010 C_d and C_l, while the transient models converged within +/- 0.050 C_d and C_l. The transient convergence signals are noisier than the steady state because the transient solutions are time-accurate. They are capturing the real oscillations in aerodynamic forces due to turbulence and unsteady flow structures. These are suppressed in the steady simulations. Figures 4.11 to 4.15 show acceptably low solution residuals.

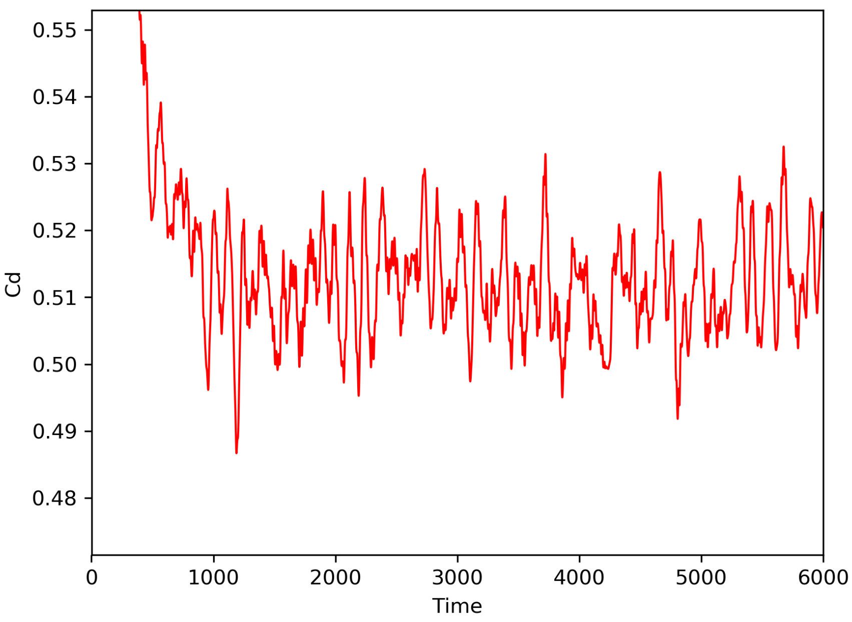

Figure 4.1: Spalart-Allmaras model C_d convergence

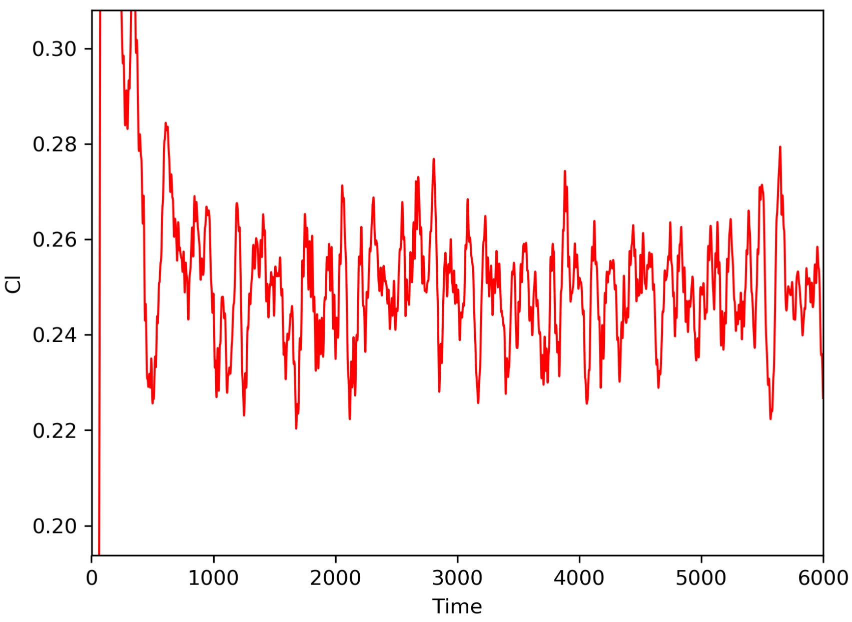

Figure 4.2: Spalart-Allmaras model C_l convergence

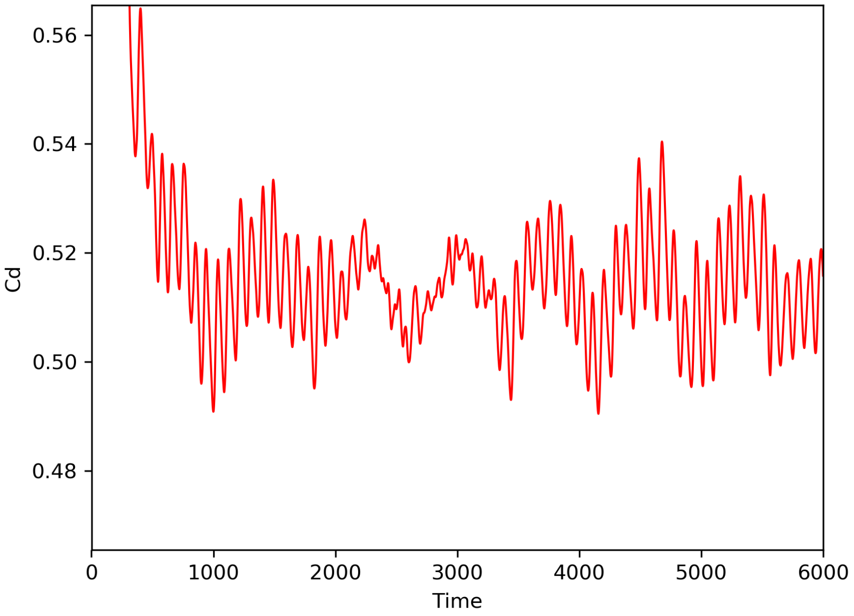

Figure 4.3: k-omega SST model C_d convergence

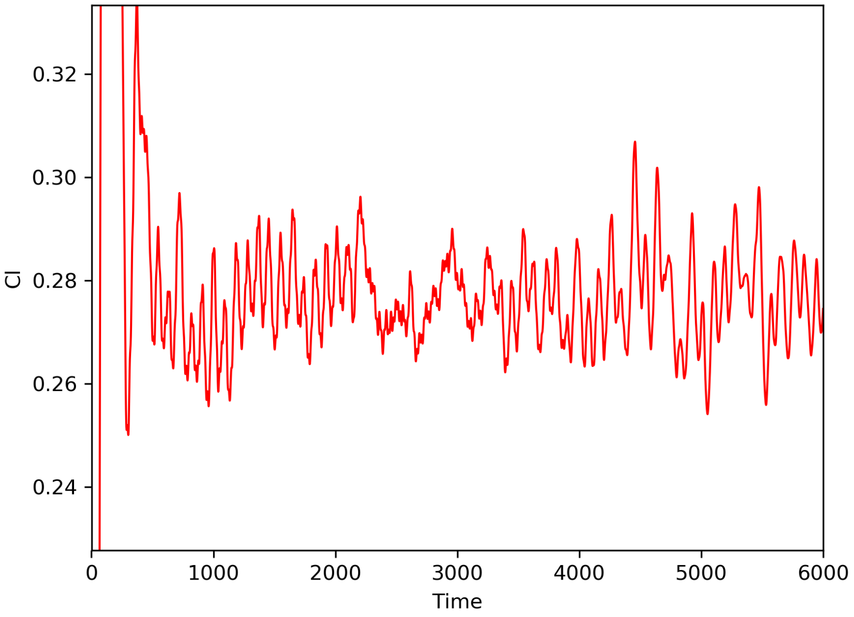

Figure 4.4: k-omega SST model C_l convergence

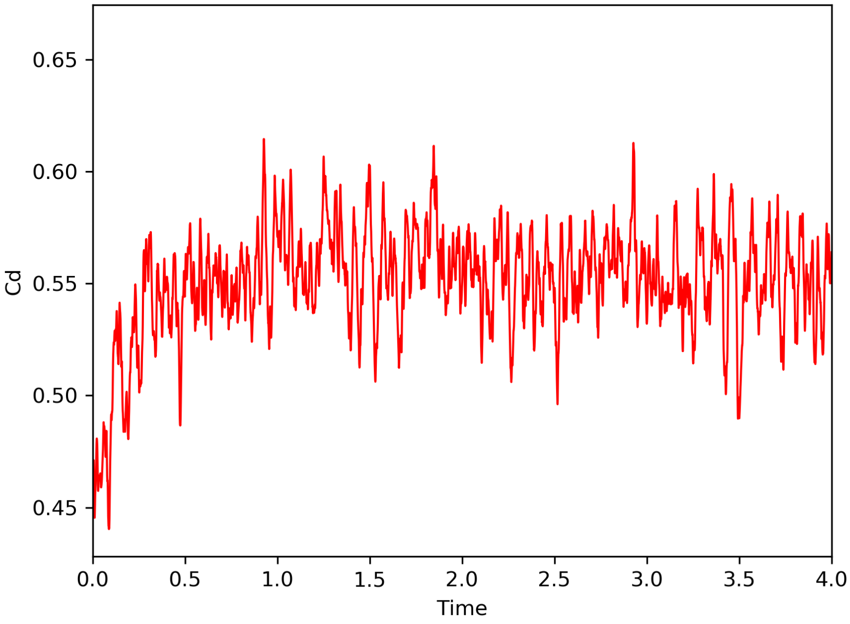

Figure 4.5: DES model C_d convergence

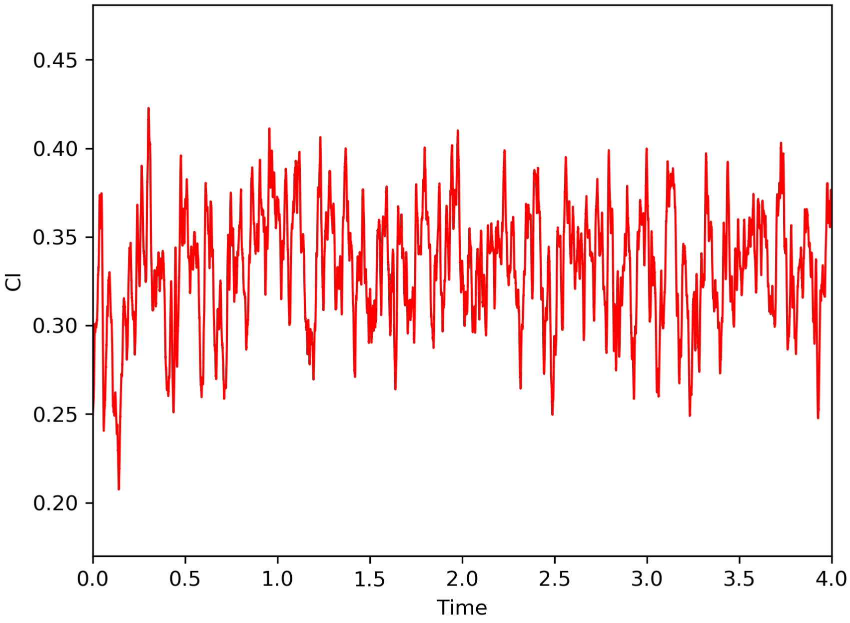

Figure 4.6: DES model C_l convergence

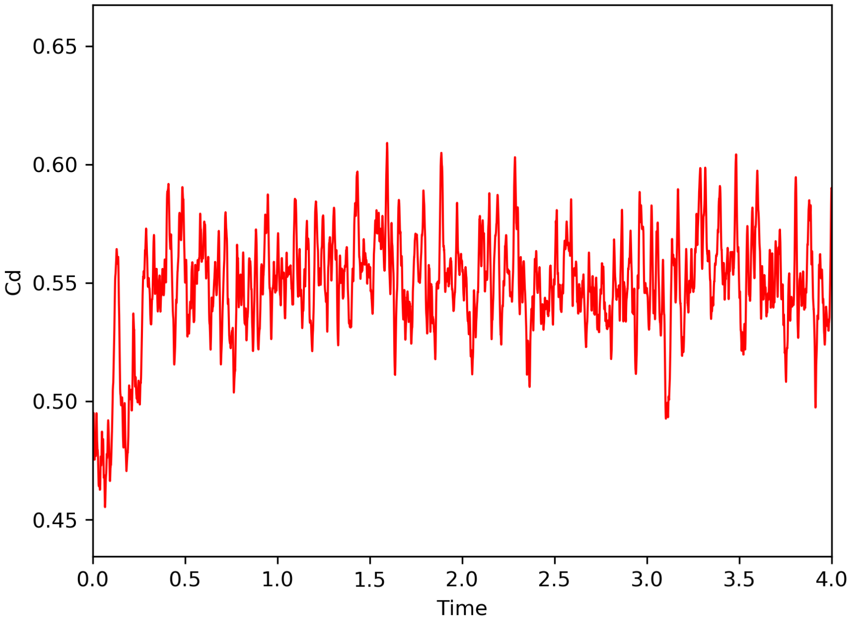

Figure 4.7: DDES model C_d convergence

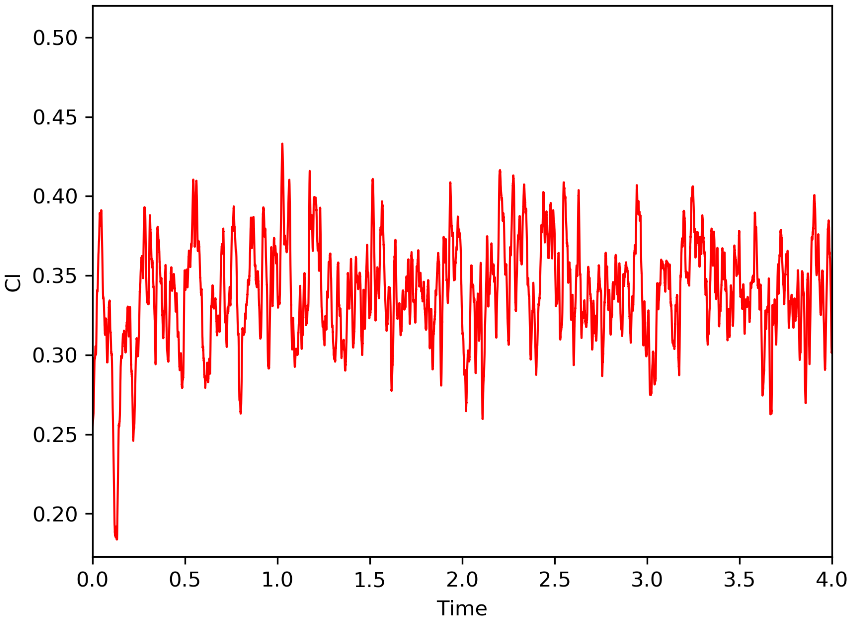

Figure 4.8: DDES model C_l convergence

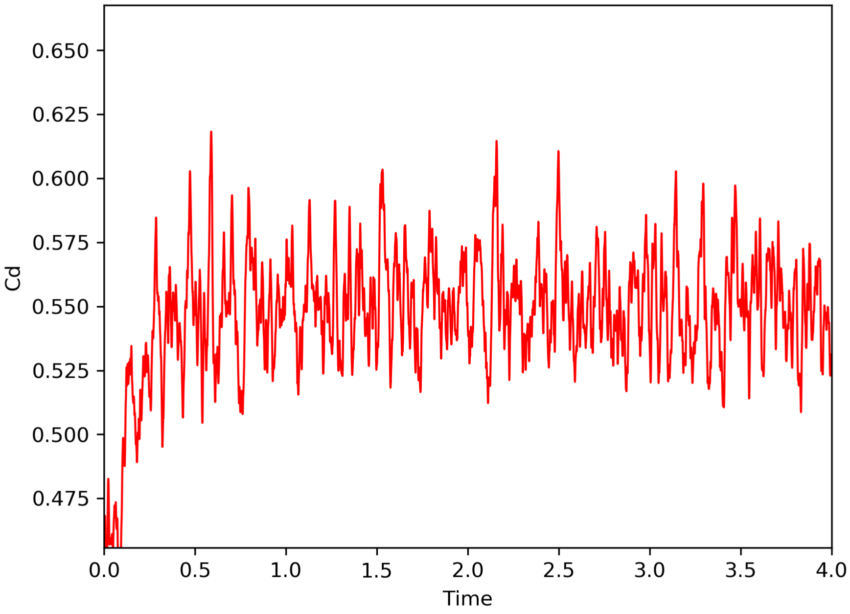

Figure 4.9: IDDES model C_d convergence

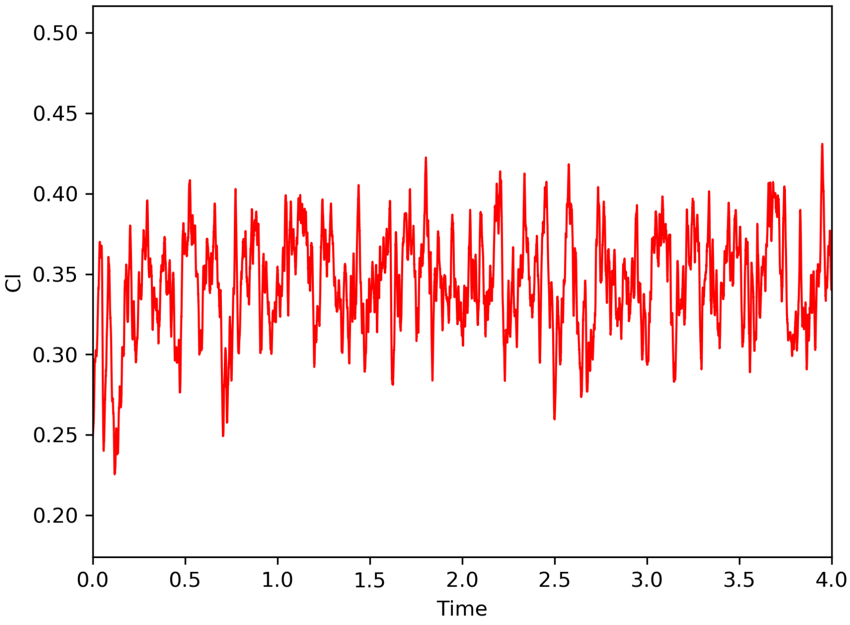

Figure 4.10: IDDES model C_l convergence

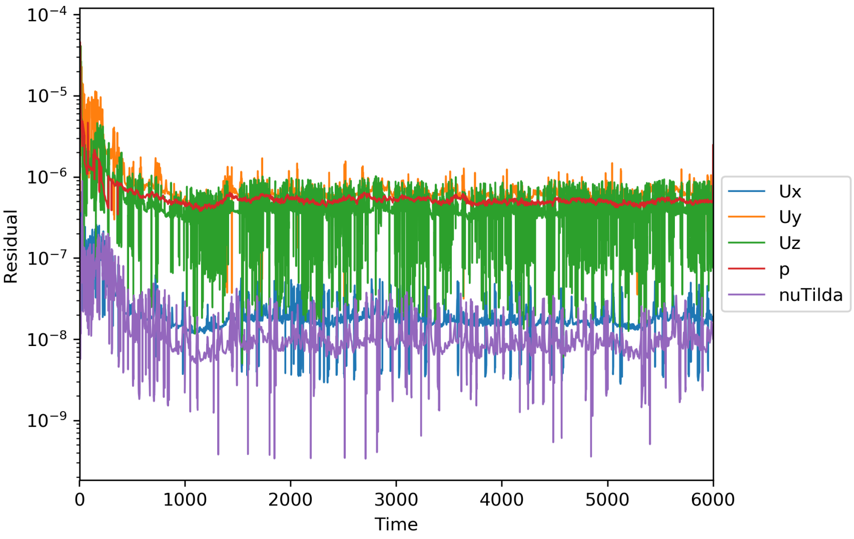

Figure 4.11: Spalart-Allmaras residuals vs time

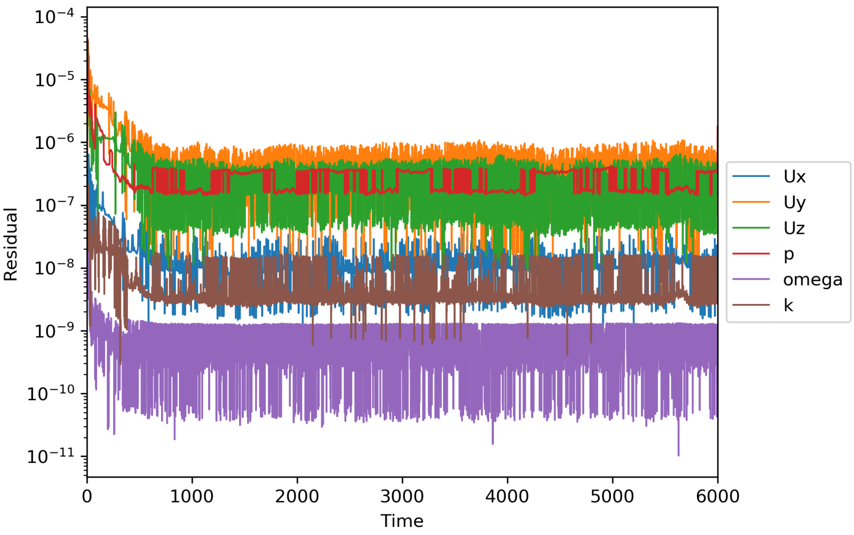

Figure 4.12: k-omega SST residuals vs time

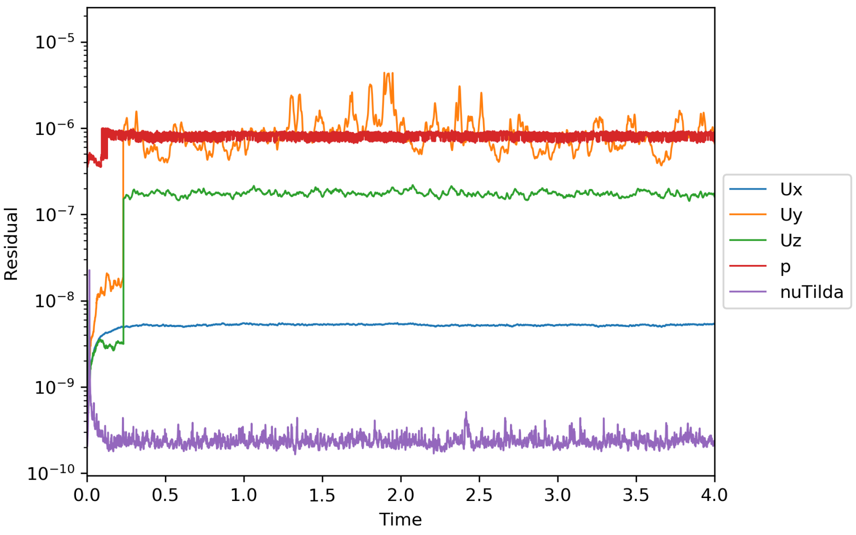

Figure 4.13: DES residuals vs time

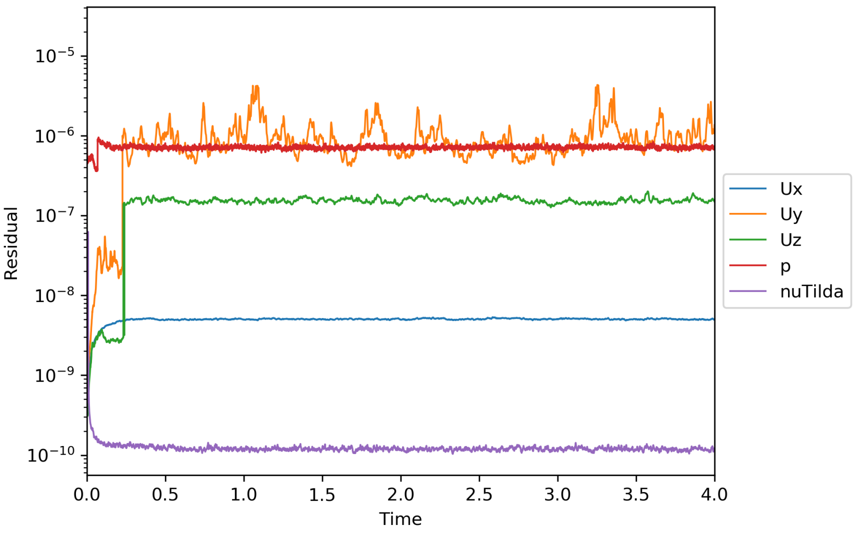

Figure 4.14: DDES residuals vs time

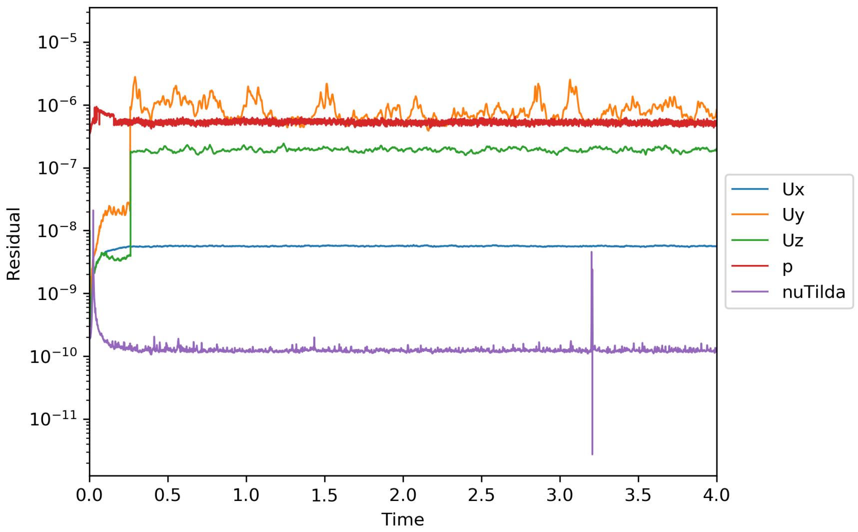

Figure 4.15: IDDES residuals vs time

Turbulence Model	C_d	C_l
Spalart-Allmaras	0.512	0.249
k-omega SST	0.513	0.277
DES	0.553	0.333
DDES	0.552	0.343
IDDES	0.551	0.347

Table 4.1: Averaged force coefficients

4.2 Force coefficients and surface C_p

To calculate aerodynamic force coefficients, the time-averaged pressure and shear stress fields are integrated over the entire model surface. The coefficient is then calculated as

$$C_x = \frac{F_x}{\frac{1}{2}\rho U_\infty^2 A f} \tag{4.1}$$

Where A_f is the projected frontal area of the vehicle, and U_∞ is the freesteam velocity. Table 4.1 shows the calculated average force coefficients.

The RANS models were within 0.001 C_d and 0.028 C_l of each other. The transient runs predicted on average 0.040 higher C_d and 0.078 higher C_l than the RANS models as shown in Table

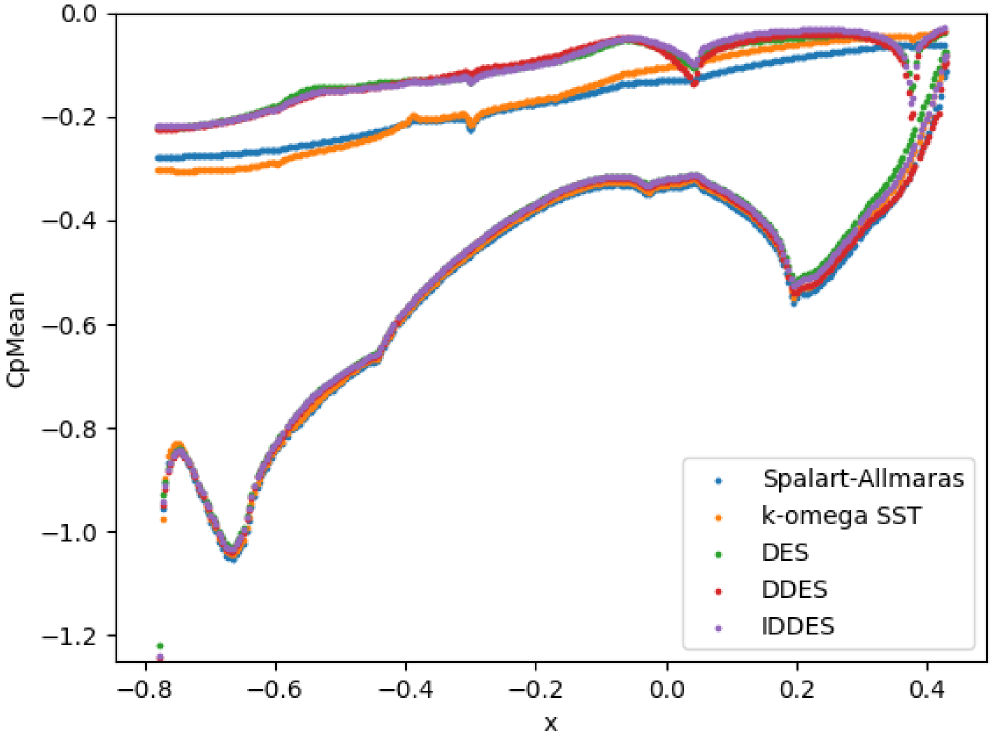

Figure 4.16: Body C_p $y = 0$ slice

4.1. The transient models were within 0.002 C_d and 0.014 C_l of each other.

By examining the centerline C_p slice in Figure 4.16 and the surface C_p images in Figures 4.17 to 4.41, the development of C_d over the vehicle can be explained as follows. There is a large increase at $x = 0$ due to stagnation on the front of the vehicle, followed by a local decrease due to lower pressure on the insides of the front wheel wells. C_d starts to increase up through $x = 1$ due to air colliding with the engine and front axle; the local C_d effect of the tires is complex due to their rotation and the ground contact patch behavior. There is a spike then drop near $x = 1.2$ from engine bulkhead, rear half of the front wheel wells, and the start of the windshield. C_d then steadily rises from $x = 1.2$ to $x = 1.6$ from the high pressures on the windshield and contribution from the side mirrors. From $x = 1.6$ to $x = 2$ C_d begins to decrease: the curvature of the roof leading edge causes the air to accelerate and static pressure to drop. From $x = 2$ to $x = 2.6$ C_d is unchanged: the roof and underbody are flat in this region, and the contribution to C_d by surface shear stress is small. From $x = 2.6$ to $x = 2.8$ C_d begins to decrease, due to curvature in the rear roof header causing the air to accelerate. At $x = 2.8$ there is a precipitous C_d spike: the passenger cab ends, and the rear of the cab sees very low C_p being in the wake. There is a short C_d decrease then increase from the low pressures on the front face of bed, then the corresponding rear face, respectively. From $x = 3.5$ to $x = 4.2$ C_d increases from air interacting with the rear axle and tires. From $x = 4.8$ to the end, there are three separate C_d increases. First, there is a smaller increases from the pressure on the inside of the tailgate, due to shear layer and air being washed in from C-pillars stagnating, plus the air recirculating within the bed area. Next, there is a large C_d increase due to the wake and low pressure on the rear face of the tailgate. Finally, the rear face of the bumper encounters low surface C_p.

The development of C_l over the vehicle can be explained as follows. There is an initial C_l dip due to high C_p on the top of the front bumper, plus the low pressure underneath it. C_l is fairly constant until the windshield and cowl region redirect the flow upwards and experience high C_p, decreasing C_l. Minimum C_l is reached near the side mirrors, after which C_p becomes negative on the windshield from and drops sharply on the roof due to the flow accelerating. C_l steadily increases over the rest of the vehicle from high C_p on the underbody and low C_p on the roof and bed.

Several differences in the C_p distribution are apparent between the steady Spalart-Allmaras and transient DES simulations. The distribution is vastly different on faces exposed to wake zones, in particular the rear glass and tailgate. C_p on the front tires appears unchanged, but is different on the rear tires. On the sides of the vehicle, the mirror wake is changed and pressure distribution around the rear wheel wells. Aft of the front axle, the underbody pressures are changed entirely. The transient DES simulations have generally higher underbody C_p than the steady state RANS. These are areas of the flow rich in detached, turbulent eddy content. Conversely, the areas which are the same are at the front of the vehicle before any wakes or detached flow features form (these are also RANS regions in the DES models).

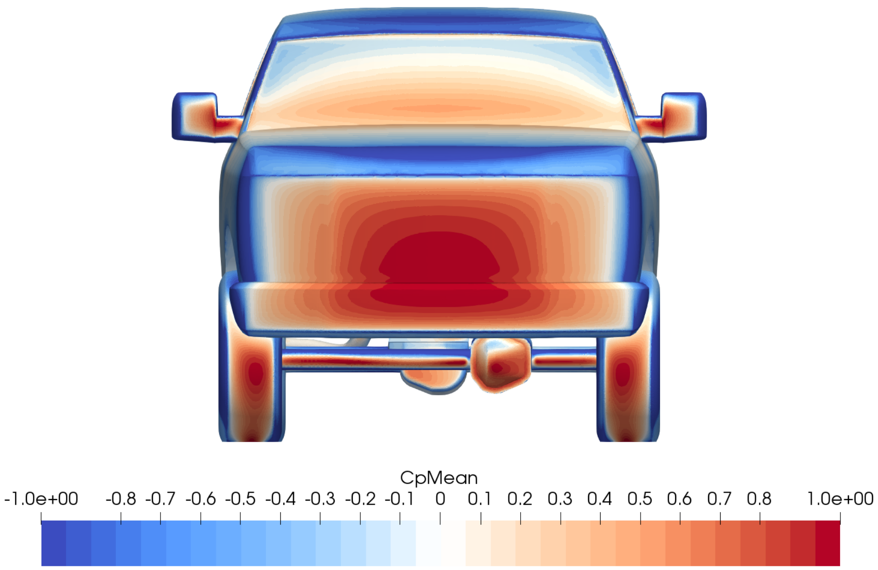

Figure 4.17: Body C_p front view, Spalart-Allmaras.

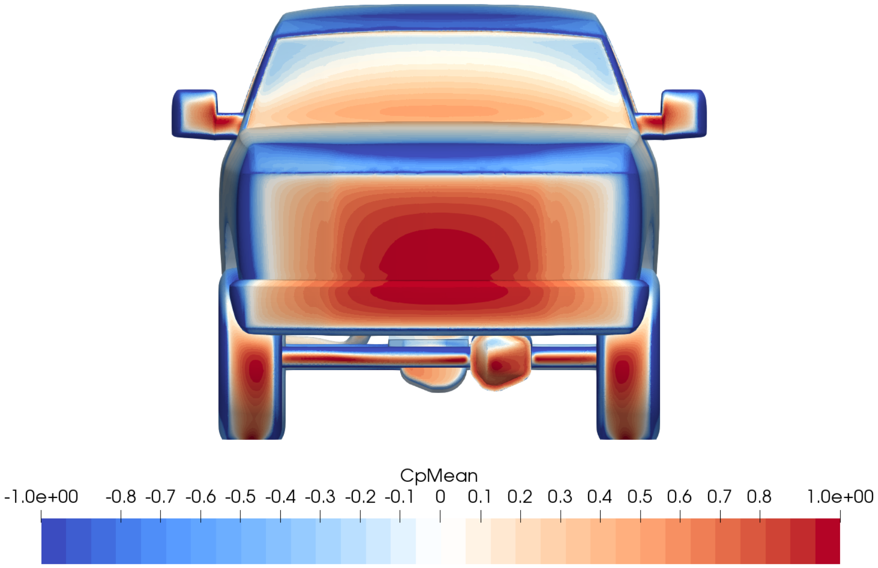

Figure 4.18: Body C_p front view, k-omega SST.

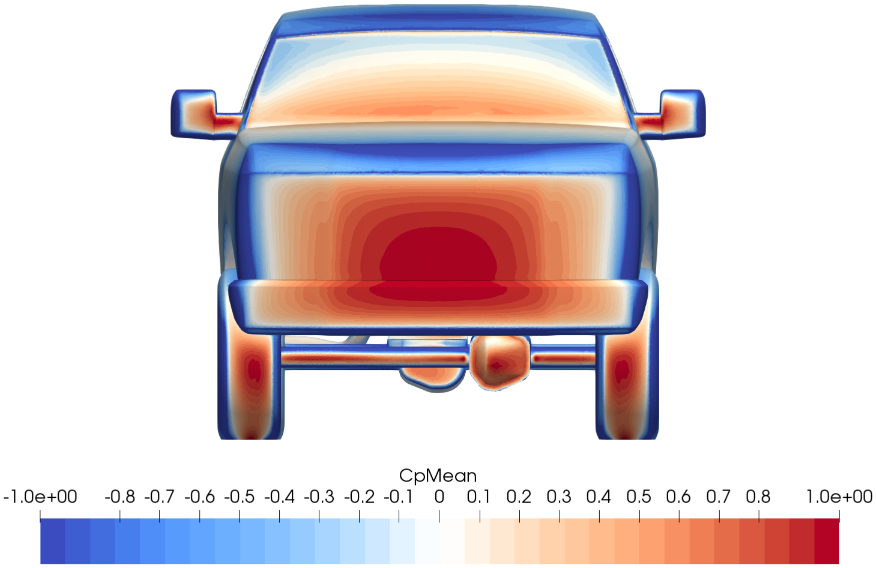

Figure 4.19: Body C_p front view, DES.

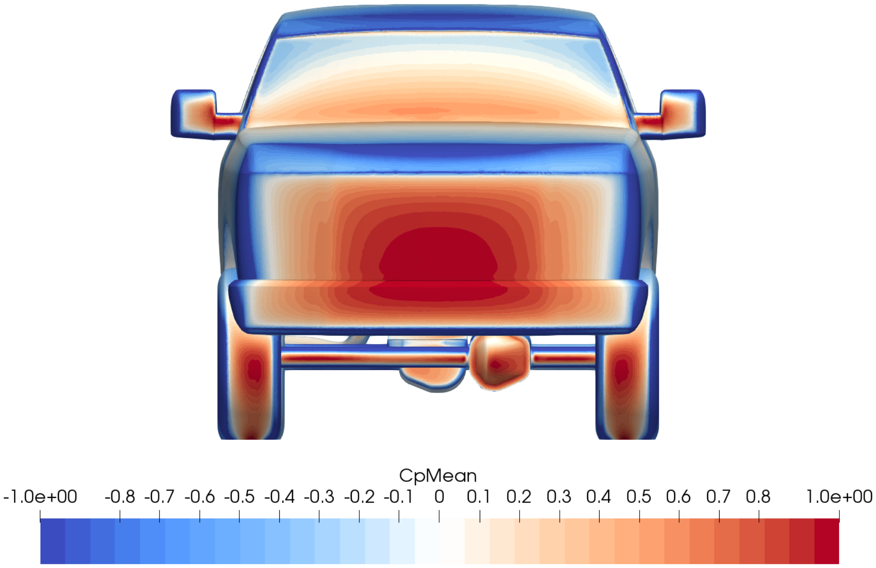

Figure 4.20: Body C_p front view, DDES.

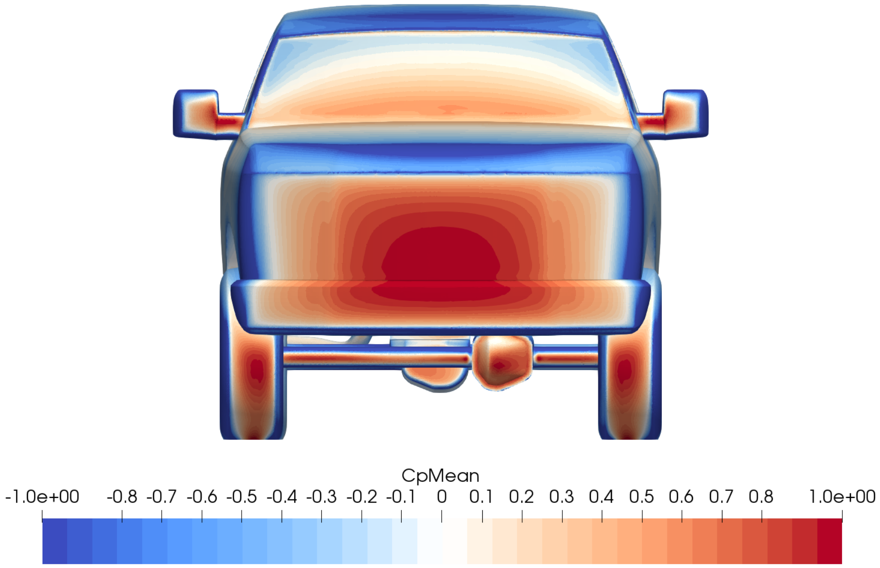

Figure 4.21: Body C_p front view, IDDES.

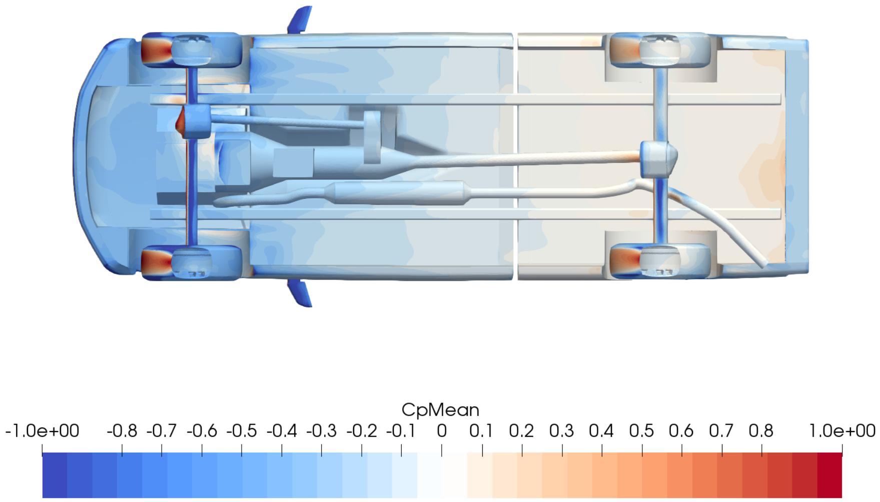

Figure 4.22: Body C_p top view, Spalart-Allmaras.

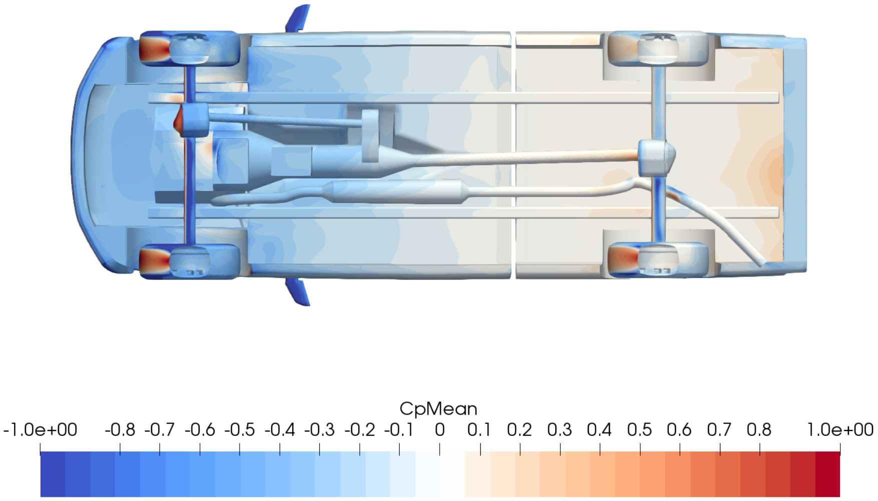

Figure 4.23: Body C_p top view, k-omega SST.

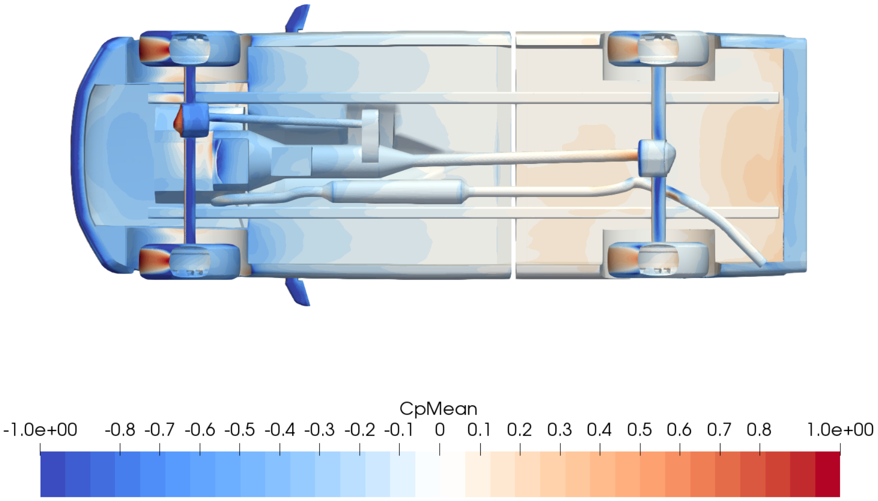

Figure 4.24: Body C_p bottom view, DES.

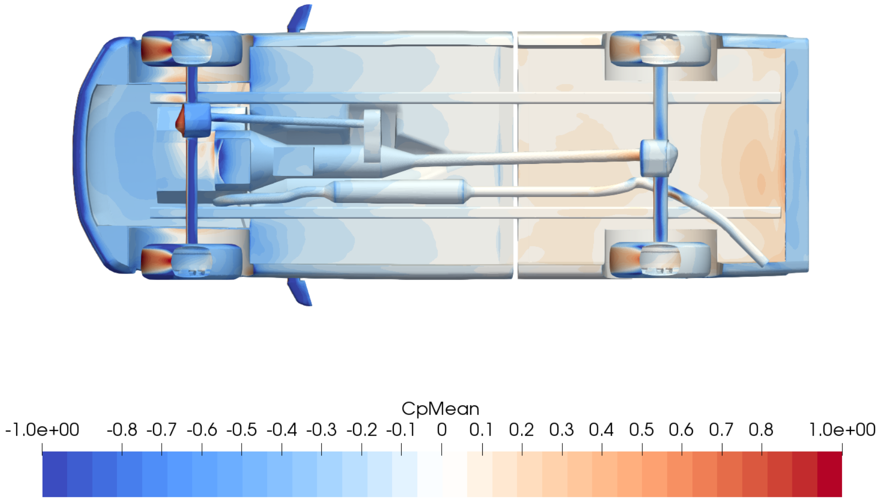

Figure 4.25: Body C_p bottom view, DDES.

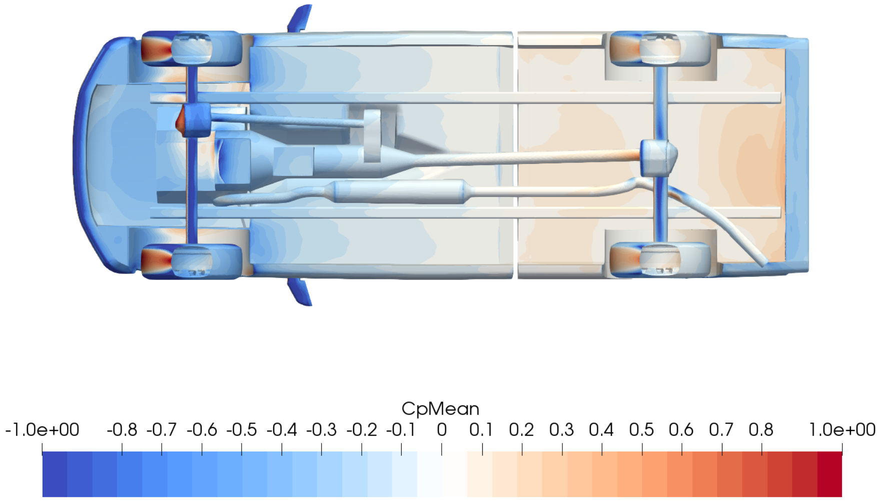

Figure 4.26: Body C_p bottom view, IDDES.

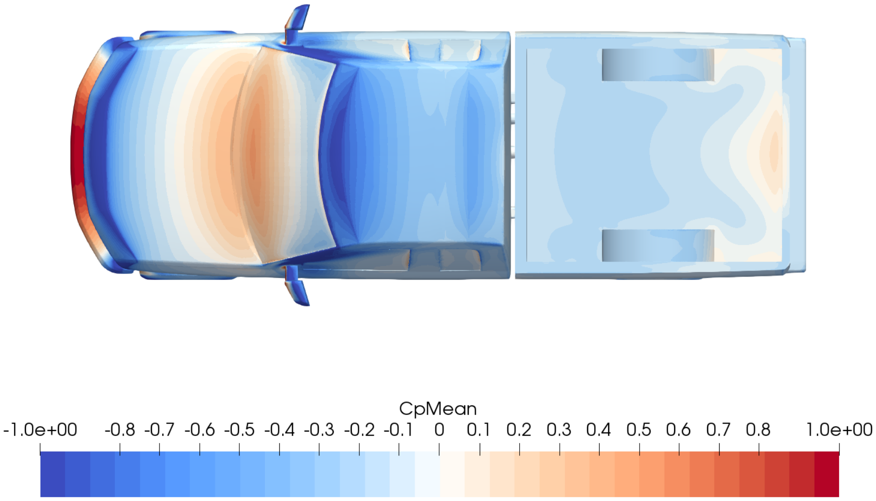

Figure 4.27: Body C_p top view, Spalart-Allmaras.

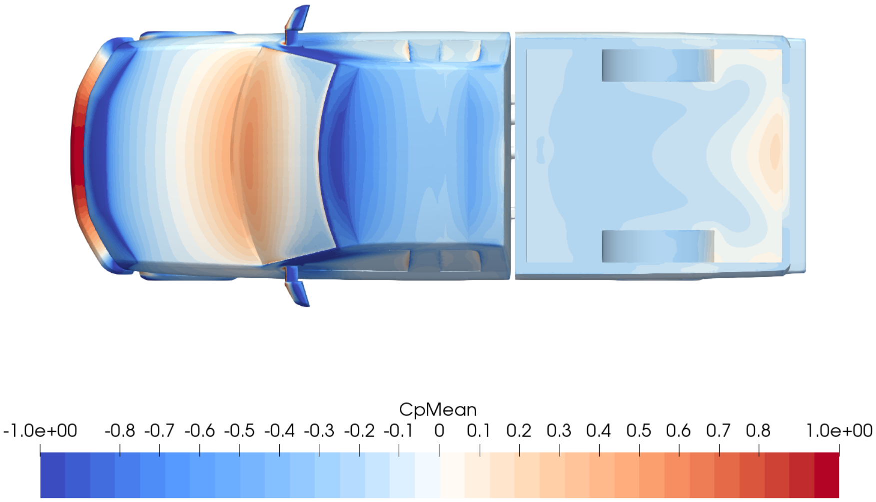

Figure 4.28: Body C_p top view, k-omega SST.

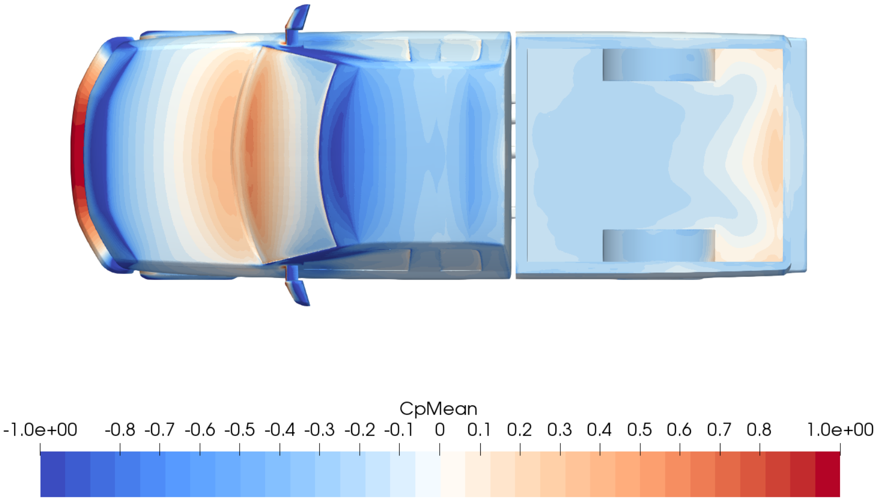

Figure 4.29: Body C_p top view, DES.

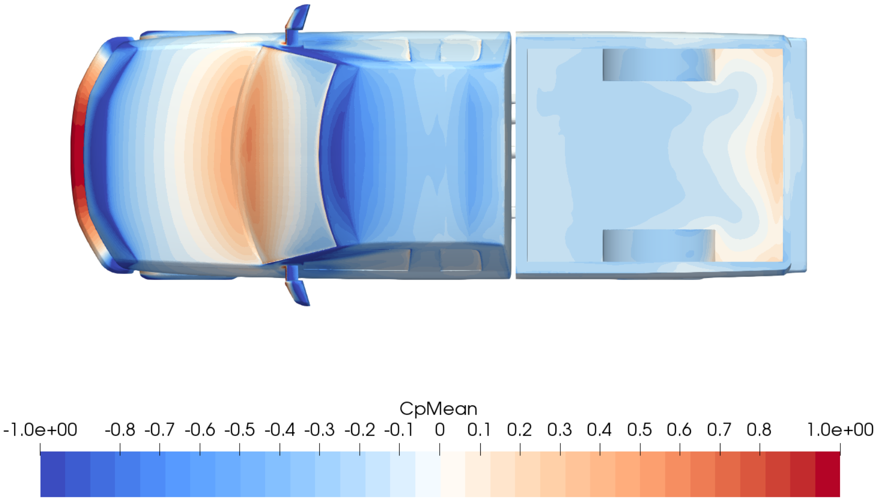

Figure 4.30: Body C_p top view, DDES.

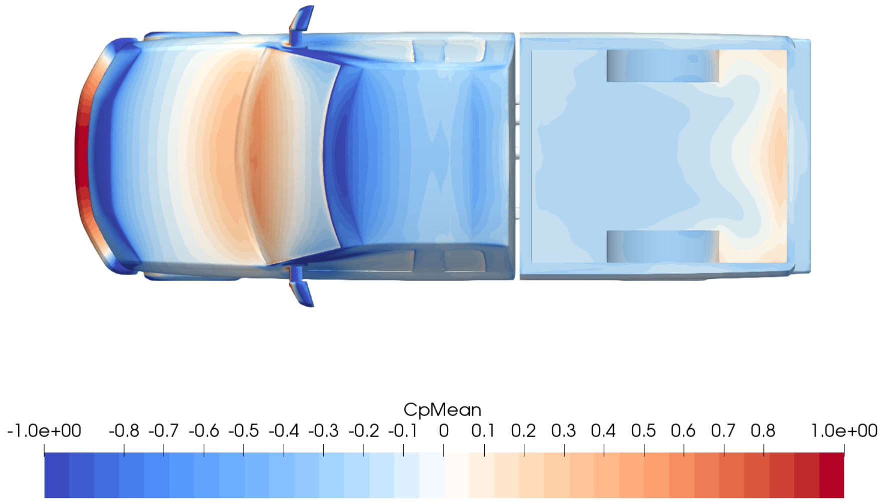

Figure 4.31: Body C_p top view, IDDES.

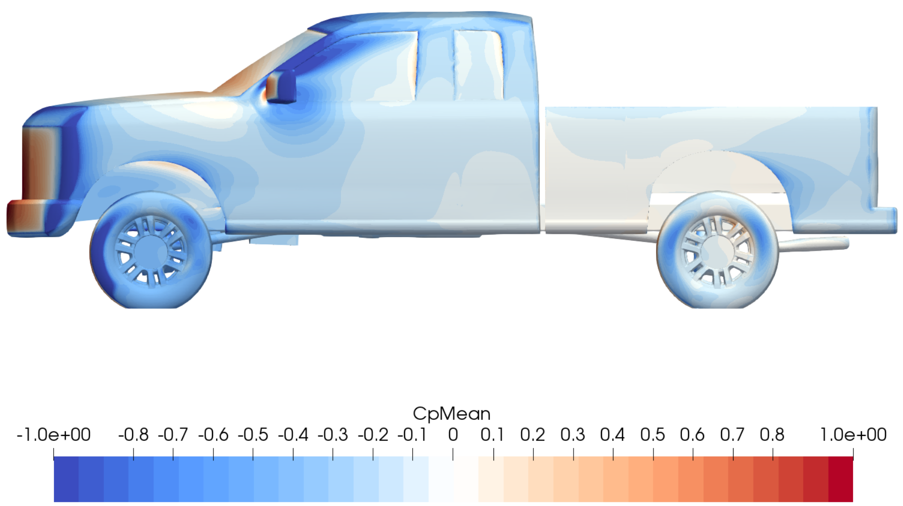

Figure 4.32: Body C_p side view, Spalart-Allmaras.

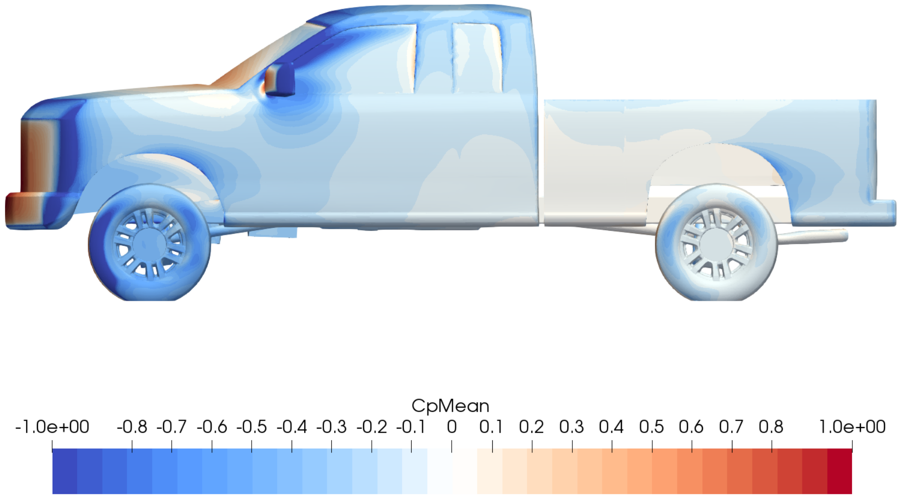

Figure 4.33: Body C_p side view, k-omega SST.

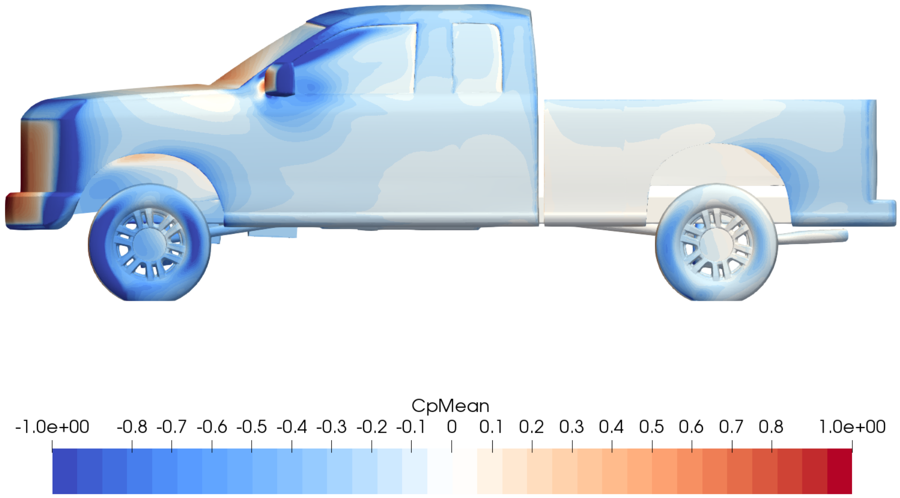

Figure 4.34: Body C_p side view, DES.

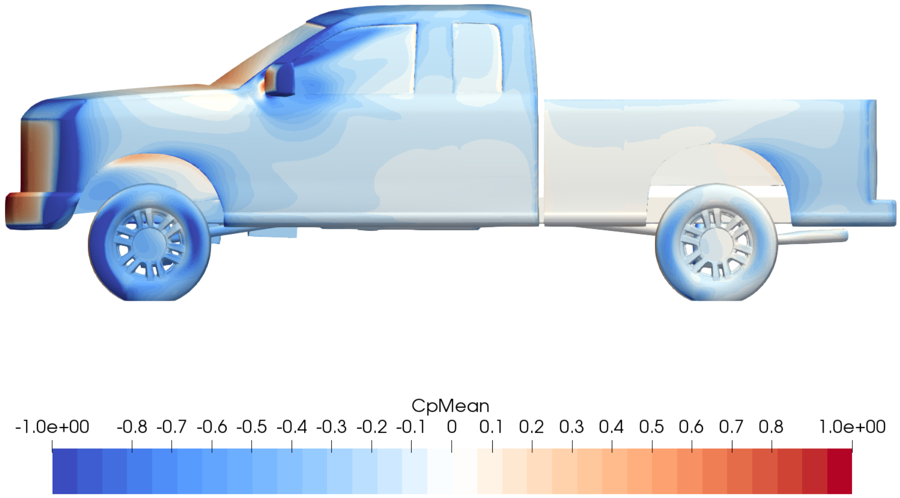

Figure 4.35: Body C_p side view, IDDES.

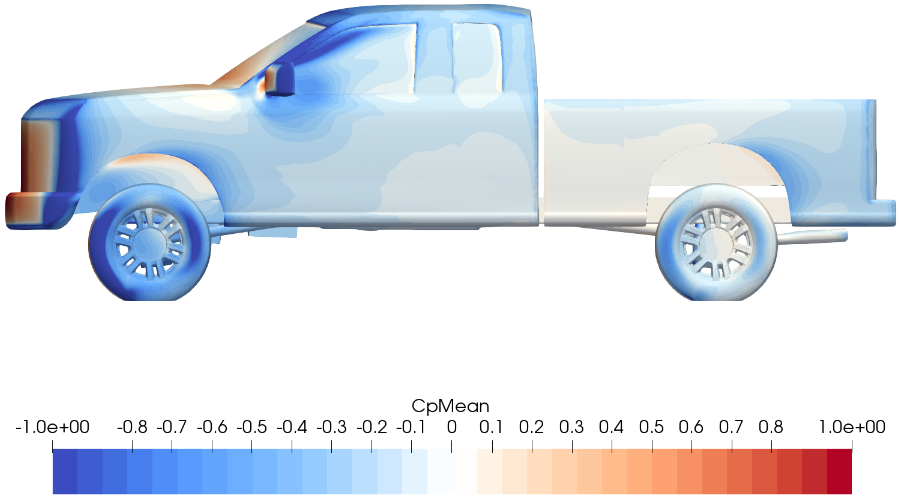

Figure 4.36: Body C_p side view, IDDES.

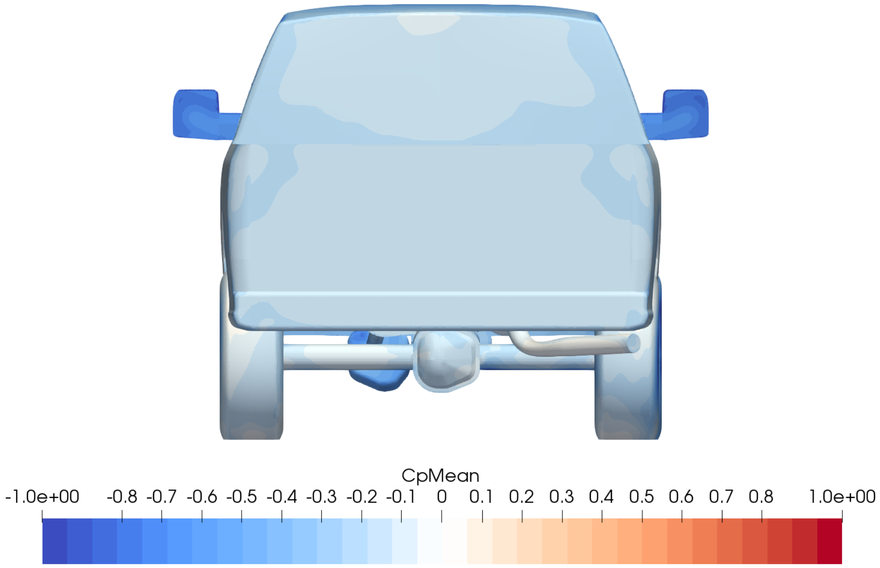

Figure 4.37: Body C_p rear view, Spalart-Allmaras.

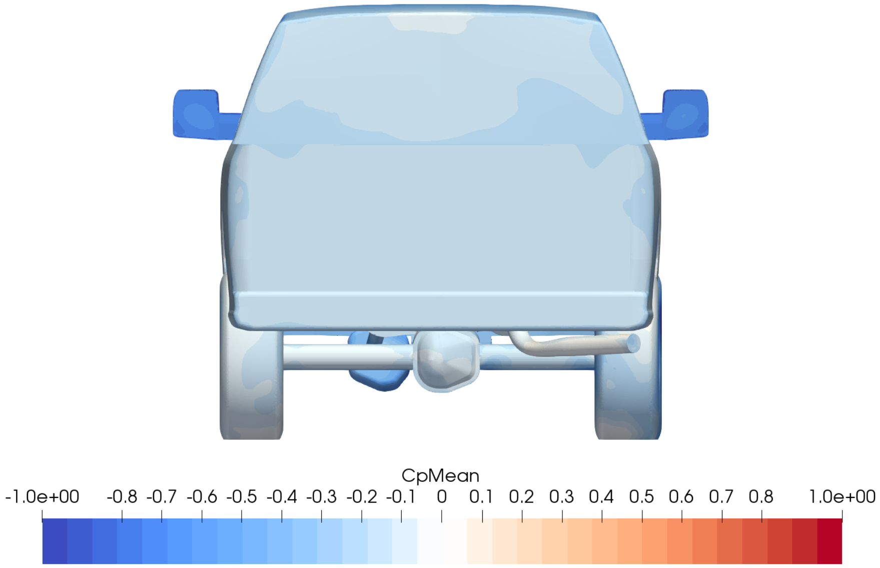

Figure 4.38: Body C_p rear view, k-omega SST.

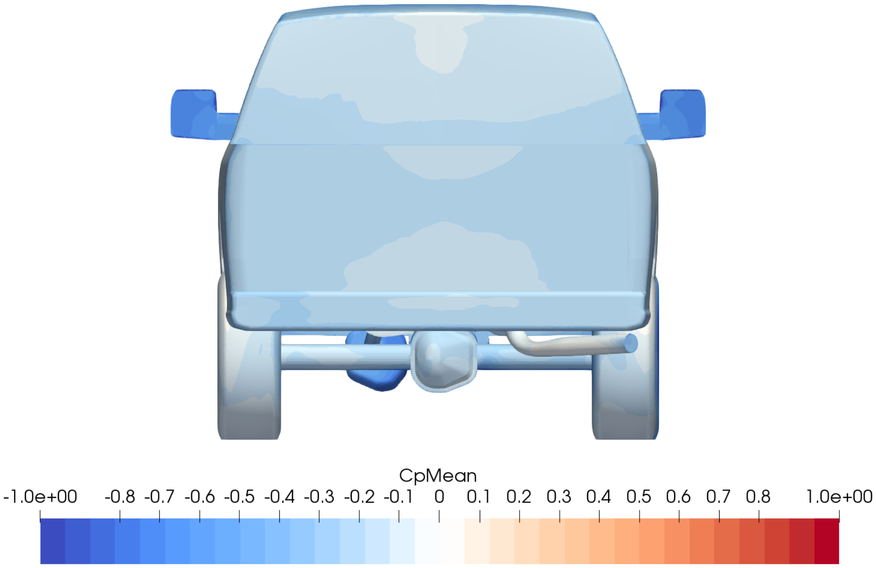

Figure 4.39: Body C_p rear view, DES.

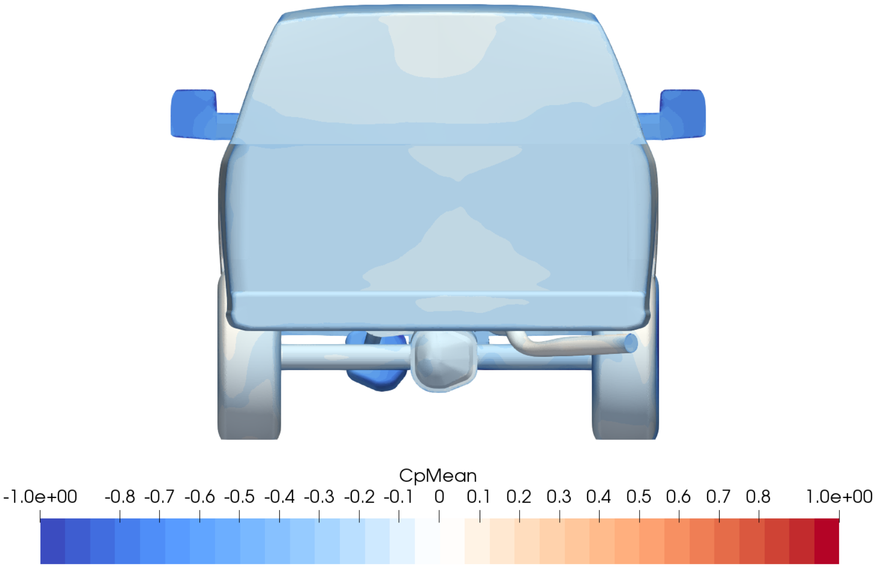

Figure 4.40: Body C_p rear view, DDES.

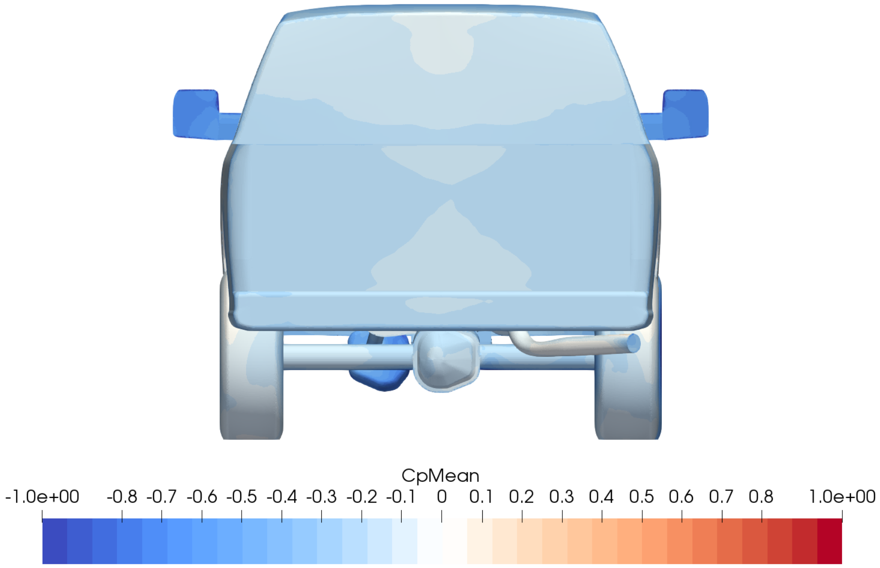

Figure 4.41: Body C_p rear view, IDDES.

4.3 Qualitative Flow Field Analysis

Figures 4.42 through 4.46 show how the velocity field changes along the y = 0 centerline of the truck. Flow decelerates as it stagnates on the front fascia and approaches the cowl; it accelerates as it moves over the hood leading edge, over the roof leading edge, and under the front bumper. The low speed region behind the cab in the bed is a large recirculation zone, similar to a backward-facing step. The shear layer demarcating the boundary between the high-speed freestream flow and the recirculation zone is visible as it descends down from the back of the cab and over the tailgate. The wake of the vehicle is also visible as a low-speed region behind the tailgate. The shear layer from the cab and the underbody flow both clearly influence the wake behavior. Moving further behind the vehicle, the wake dissipates relatively quickly, yet the lower-speed flow extends for many truck-lengths beyond. The behavior of the wake and shear layer changes significantly between the Spalart-Allmaras and DES models, but there is no noticeable difference between the DES models. The shape of the DES wakes behind the tailgate are distinguished from RANS due to the large scale eddy content being resolved there.

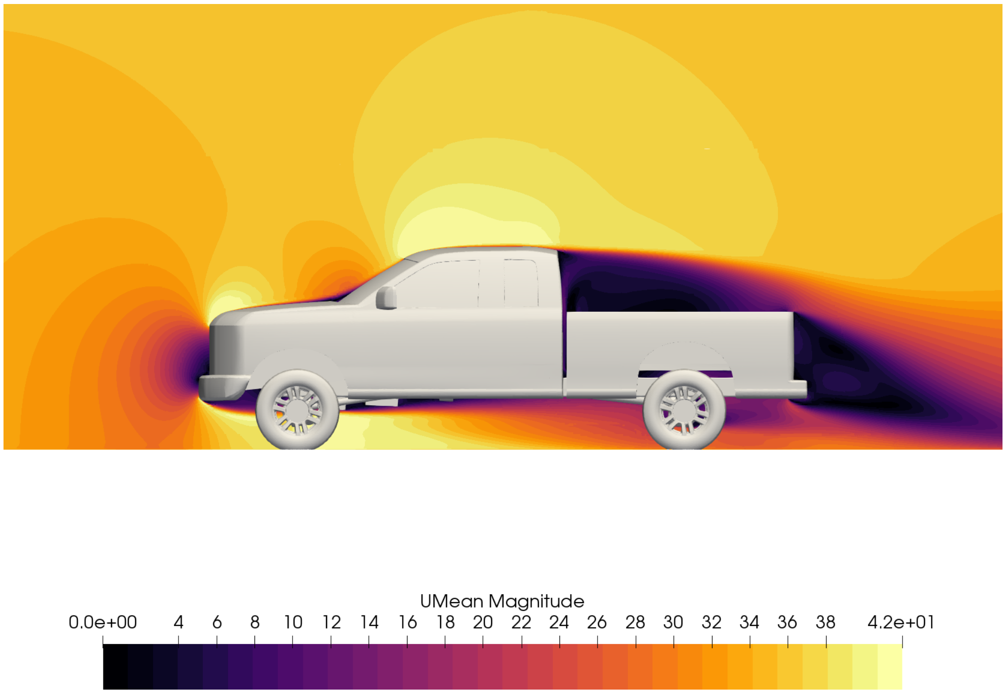

Figure 4.42: U/U_∞ y = 0 slice, Spalart-Allmaras.

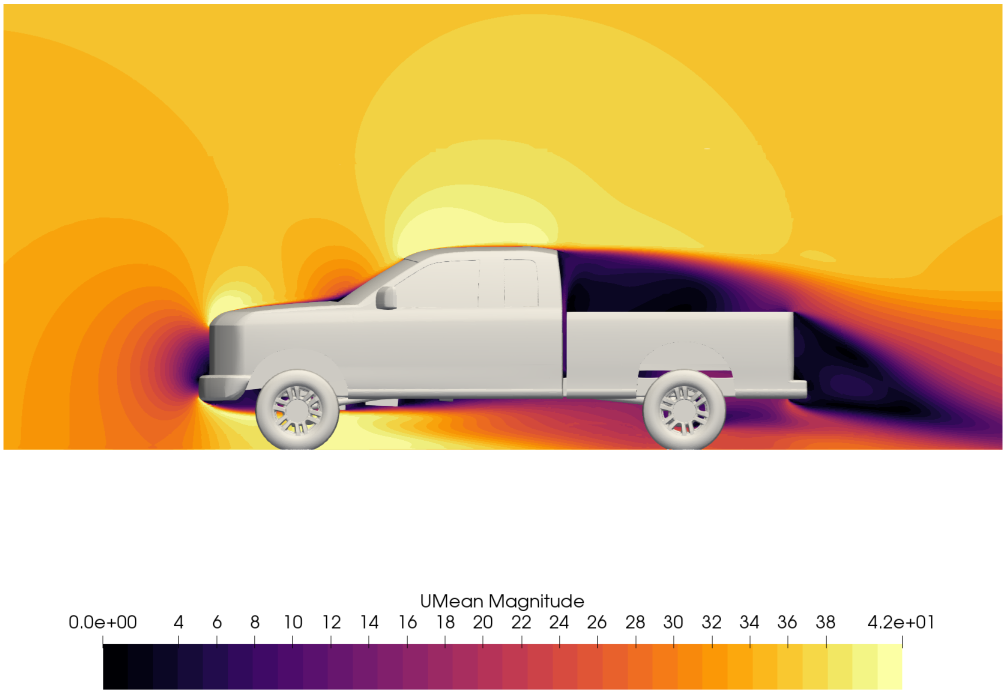

Figure 4.43: U/U_∞ y = 0 slice, k-omega SST.

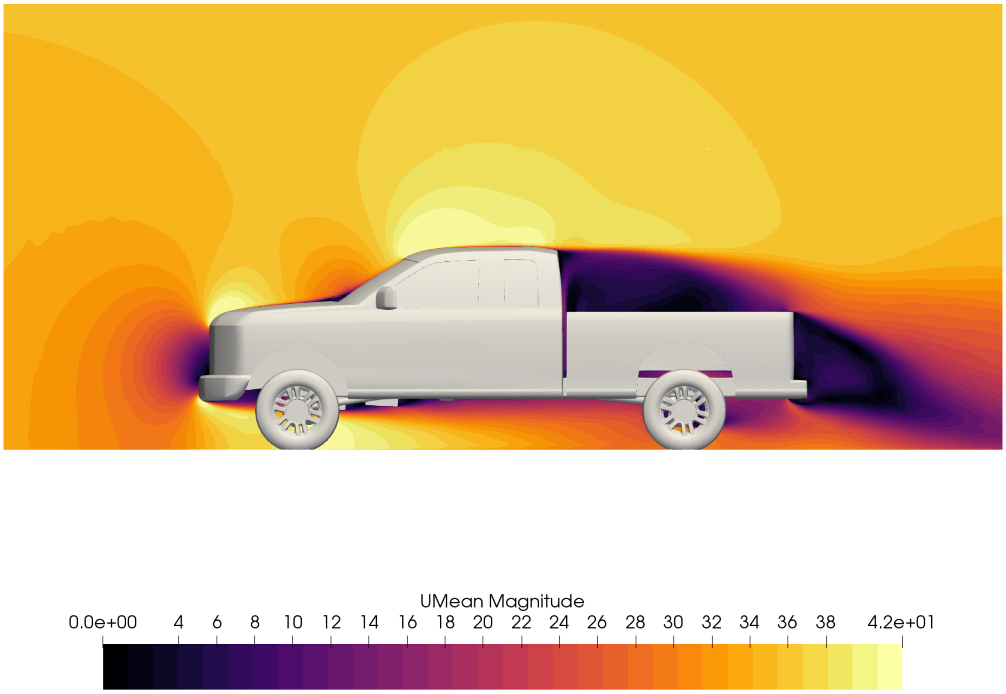

Figure 4.44: U/U_∞ y = 0 slice, DES.

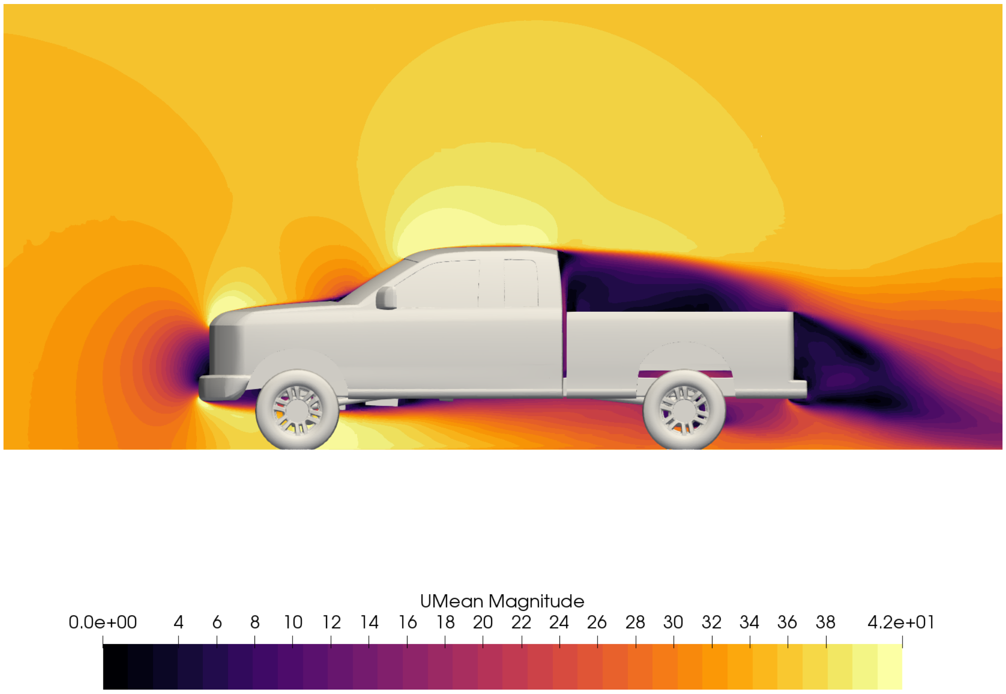

Figure 4.45: U/U_∞ y = 0 slice, DDES.

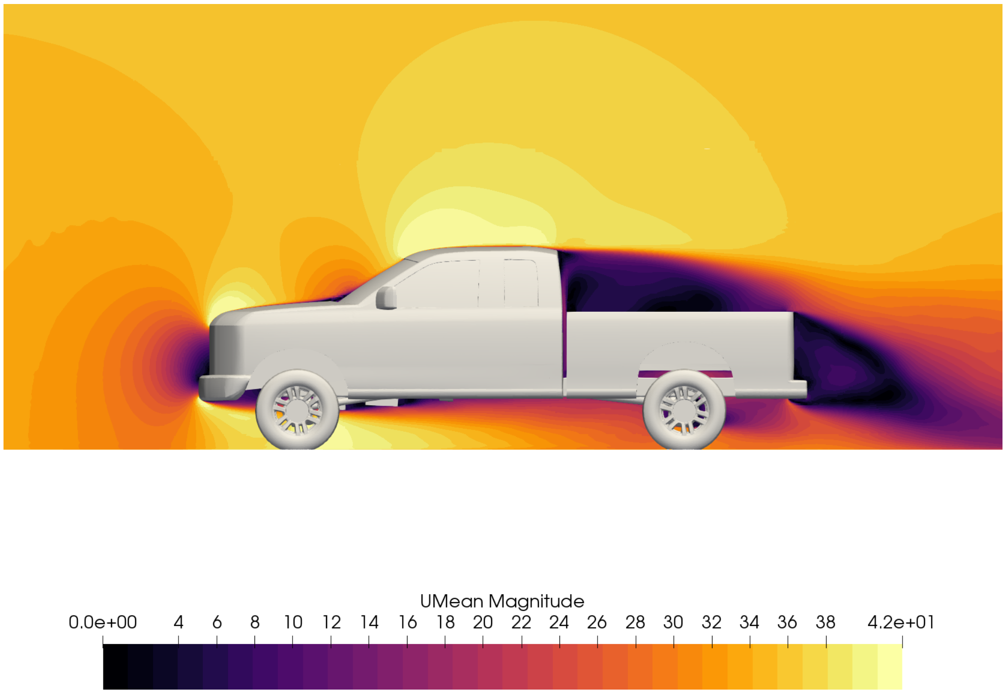

Figure 4.46: U/U_∞ y = 0 slice, IDDES.

Figures 4.47 through 4.51 show an XY slice of the velocity field through the middle of the tires. We can see the wakes being ejected outwards from the wheels influence the flow downstream, as well as the effect of the underbody component such as the front axle obstructing the flow. Spalart Allmaras shows greatly exaggerated wakes behind the underbody components , and the initial jet from the front underbody flow perpetuates further downstream before dissipating, compared to the DES models.

To visualize the wakes three-dimensionally, we can take isosurfaces of C_{pt} shown in Figures 4.52 through 4.61. In wake zones, high vorticity causes fluid friction and energy dissipation, reflected by decreased C_{pt}. Therefore, we can visualize the boundaries of the zone by drawing three-dimensional contours at $C_{pt} = 0$, since negative C_{pt} values will be in the wake. Wake structures are evident around the mirrors, wheels, cab, tailgate, and axles. Observe the smaller length- and time-scale content visible in the DES variant isosurfaces which is not present in the RANS simulation. The front axle and wheel wakes persist seemingly twice as long downstream in Spalart-Allmaras compared to the DES models. Interestingly, the rear tire wake is asymmetric on the RANS models,

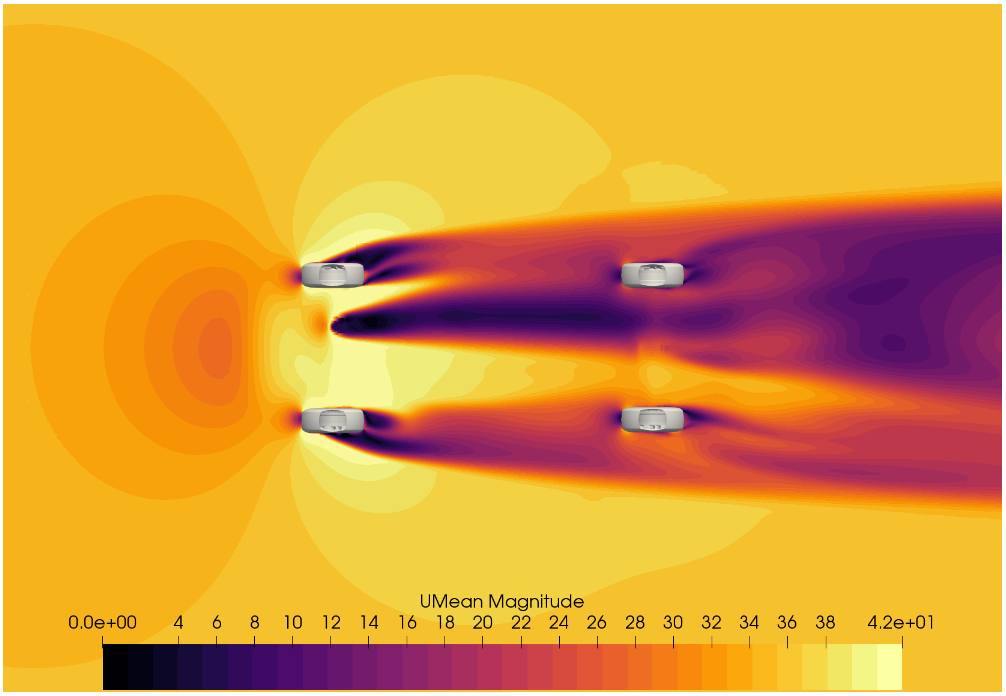

Figure 4.47: U/U_∞ z = 0.16 slice, Spalart-Allmaras.

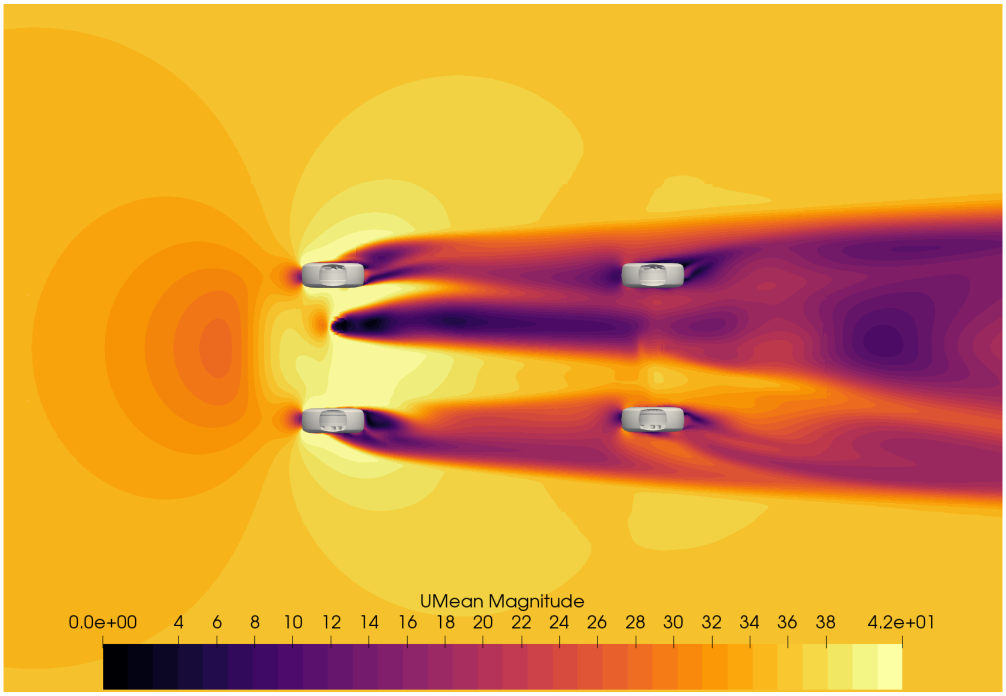

Figure 4.48: U/U_∞ z = 0.16 slice, k-omega SST.

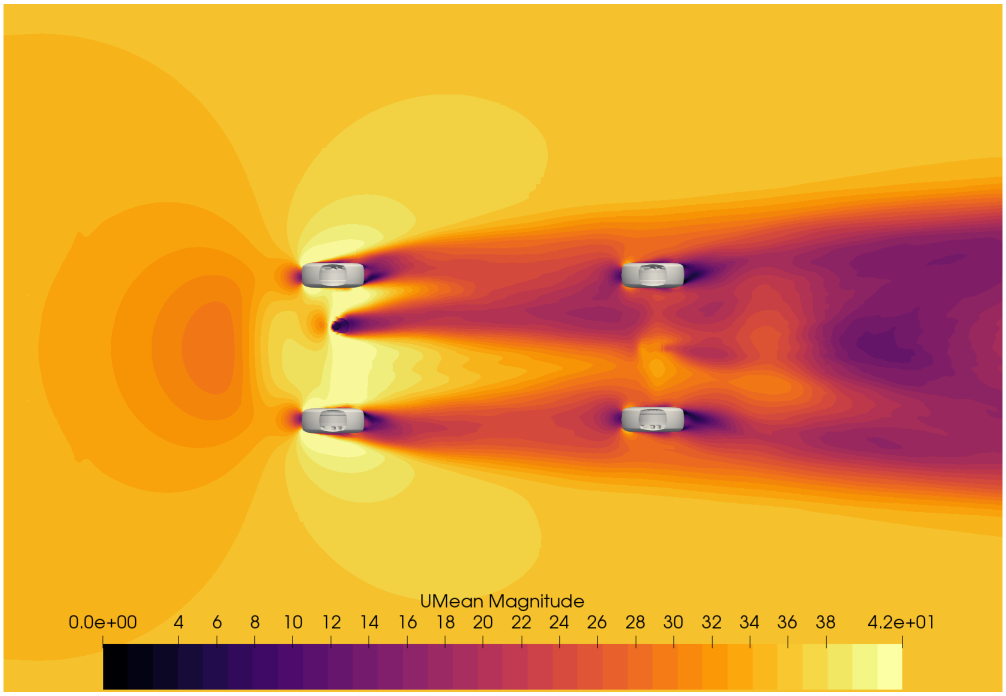

Figure 4.49: U/U_{∞} z = 0.16 slice, DES.

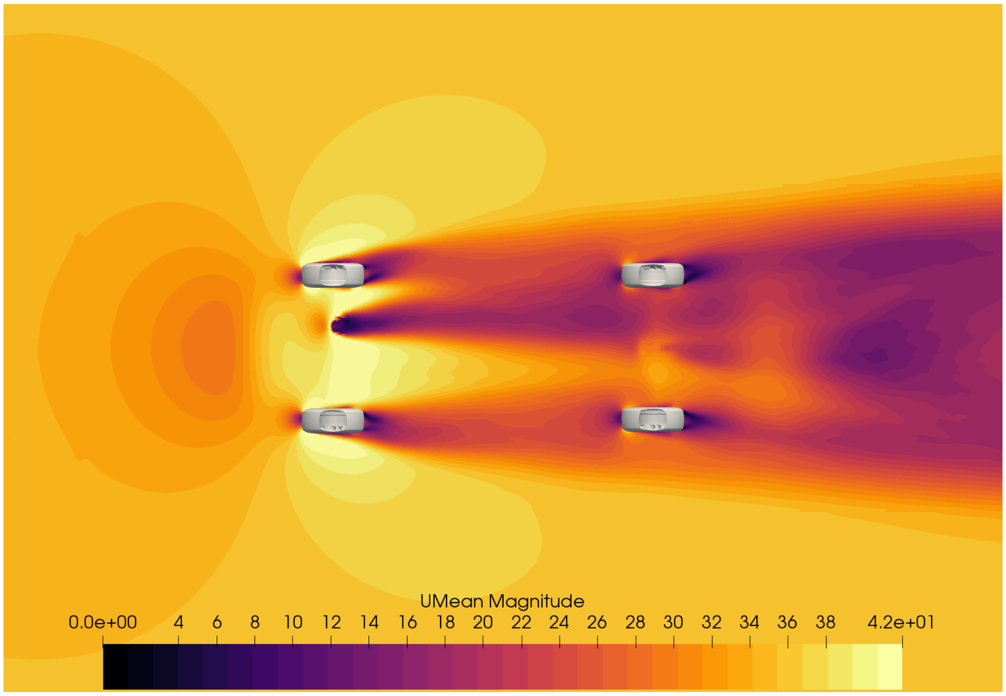

Figure 4.50: U/U_{∞} z = 0.16 slice, DDES.

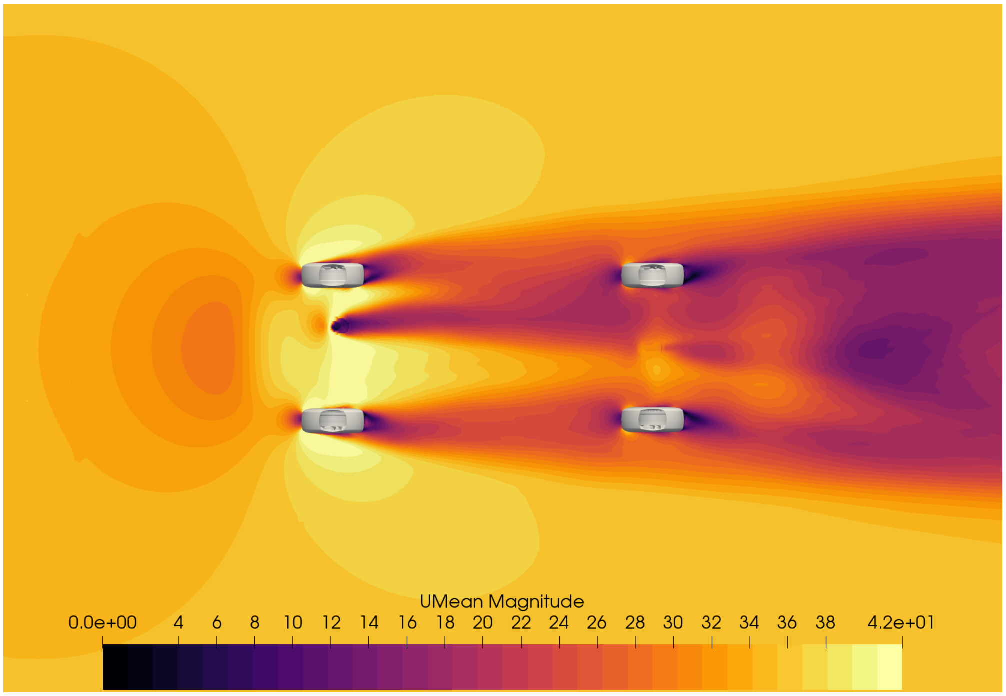

Figure 4.51: U/U_∞ z = 0.16 slice, IDDES.

kicking out noticeably on the rear right tire.

We can visualize the vortex structures present in the flow with slices of vorticity. Figures 4.62 through 4.96 reveal the vortex cores and their rotation. See that the A-pillar and mirror vortices are elongated in Spalart-Allmaras compared to DES. In the DES models, these vortices seem to burst much earlier. The front wheels show elongated structures as well, and the rear wheels in particular have several vortex structures which are absent in DES. The asymmetric flow feature on the rear right tire is obserable again here on the RANS models. See the vortices washing around the bottom of the C-pillars into the bed. The largest differences in vortex structures are observed near the rear of the vehicle. The horizontal vortex structure washing over the tailgate is present in the DES models but completely absent in RANS. The RANS models also have some structures near the rear tires that do not appear in DES. The vortices rolling off the side of the tailgate and up from the bumper appear smaller in RANS than in DES. Overall, the DES models showed little differences between each other.

When flow detaches from the wall, the velocity in the boundary layer approaches zero and then

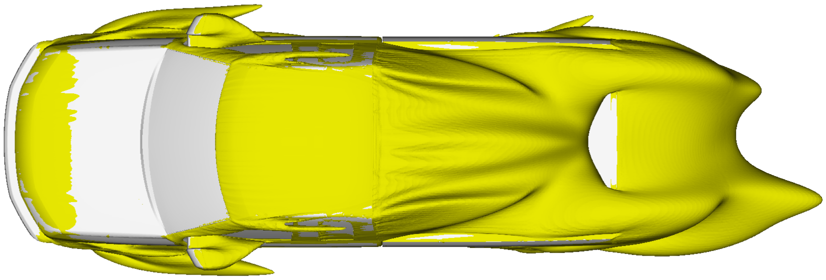

Figure 4.52: C_{pt} isosurface, top, Spalart-Allmaras.

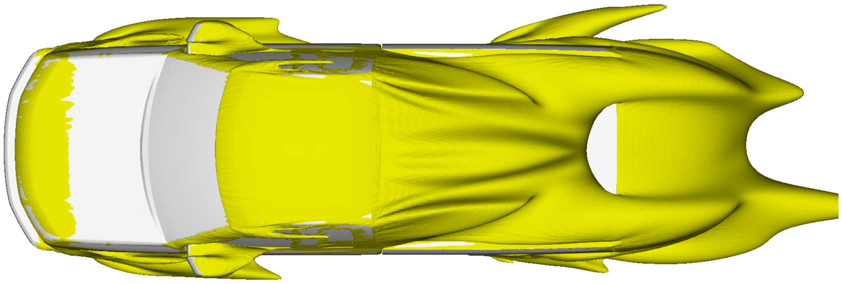

Figure 4.53: C_{pt} isosurface, top, k-omega SST.

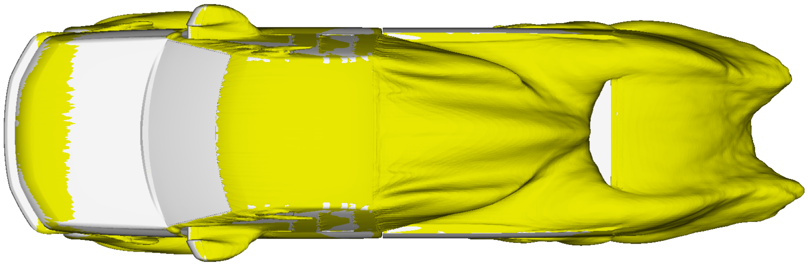

Figure 4.54: C_{pt} isosurface, top, DES.

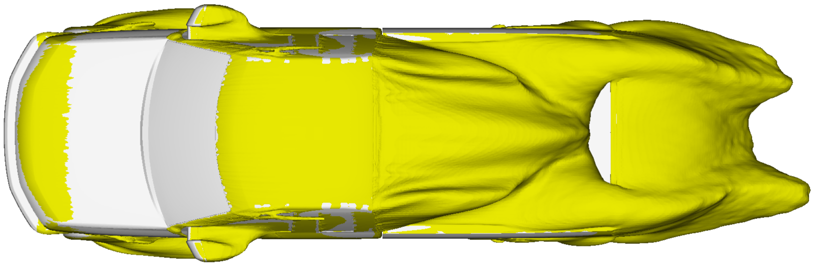

Figure 4.55: C_{pt} isosurface, top, DDES.

Figure 4.56: C_{pt} isosurface, top, IDDES.

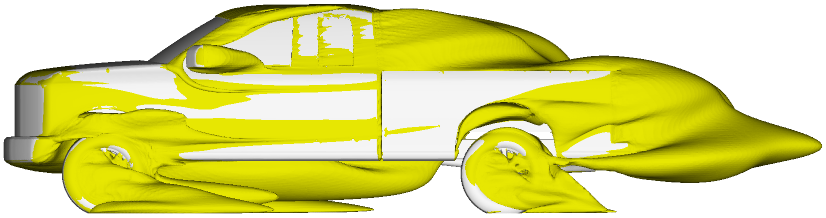

Figure 4.57: C_{pt} isosurface, side, Spalart-Allmaras.

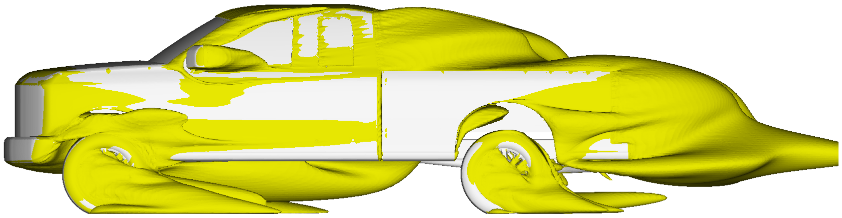

Figure 4.58: C_{pt} isosurface, side, k-omega SST.

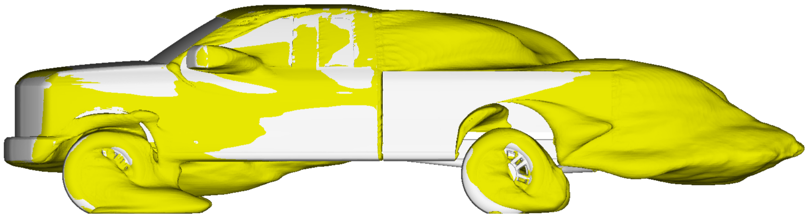

Figure 4.59: C_{pt} isosurface, side, DES.

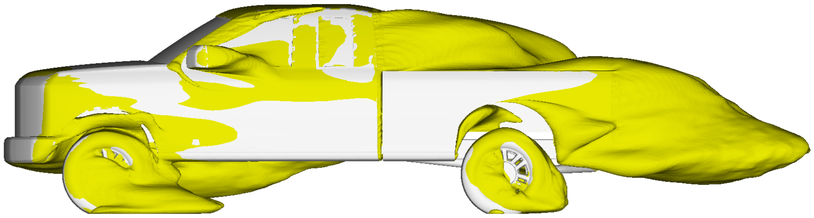

Figure 4.60: C_{pt} isosurface, side, DDES.

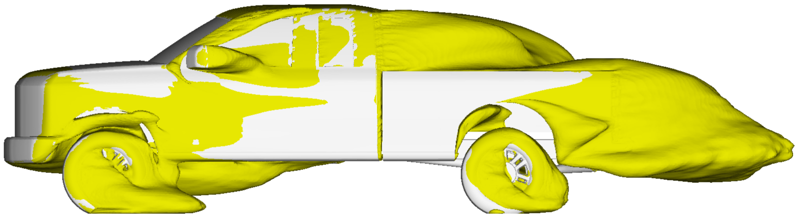

Figure 4.61: C_{pt} isosurface, side, IDDES.

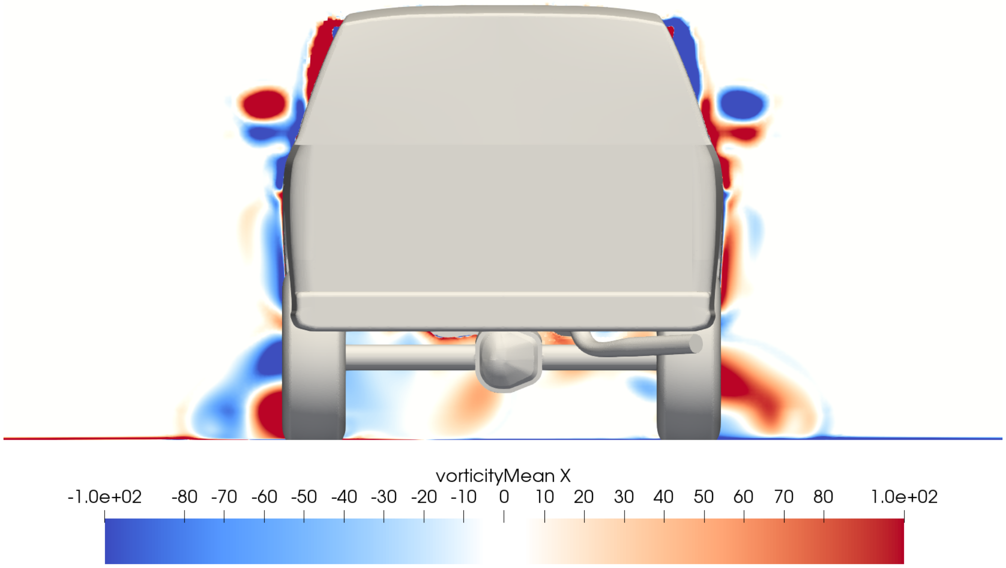

Figure 4.62: Mean x–vorticity $x = -0.5$ slice, Spalart-Allmaras.

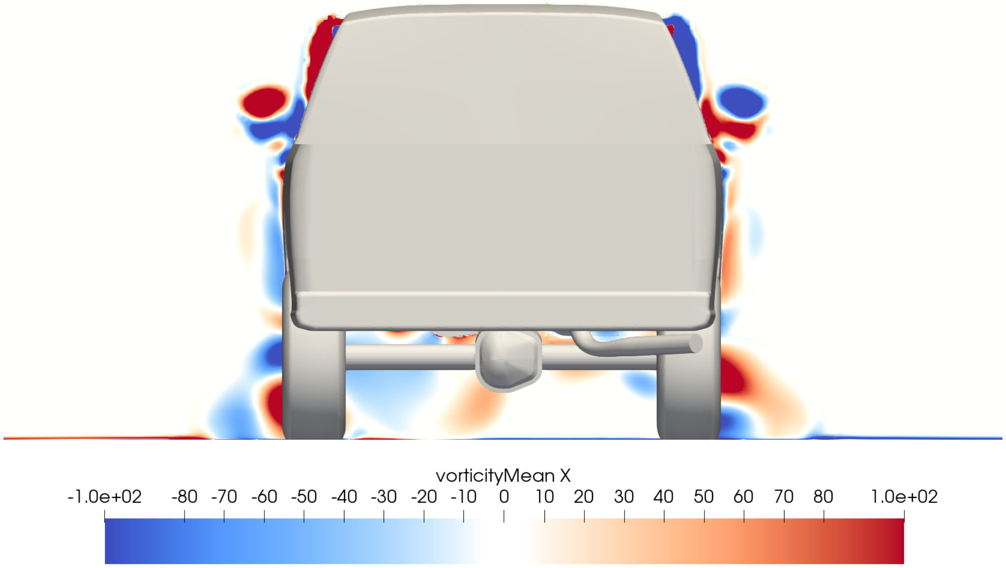

Figure 4.63: Mean x–vorticity $x = -0.5$ slice, k-omega SST.

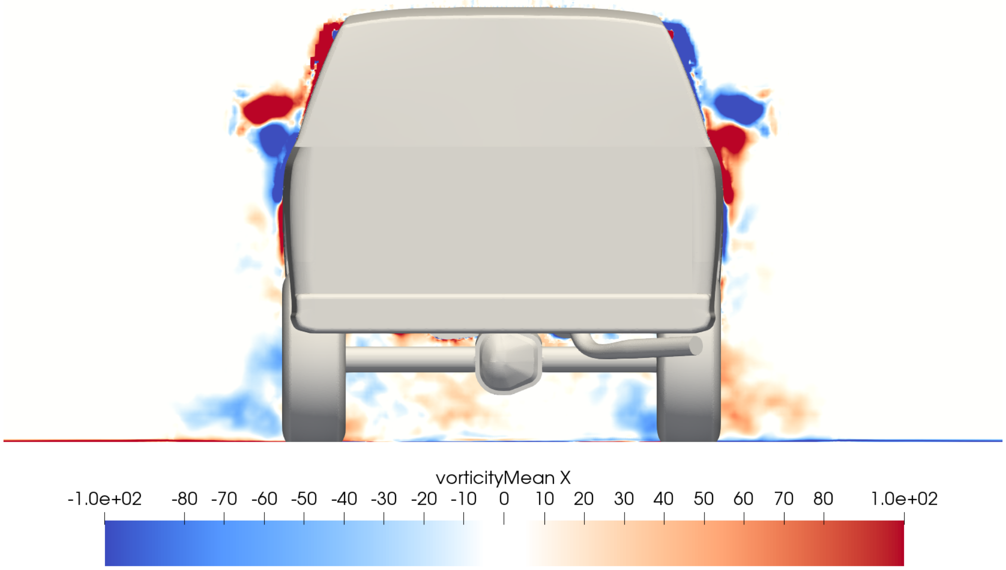

Figure 4.64: Mean x–vorticity $x = -0.5$ slice, DES.

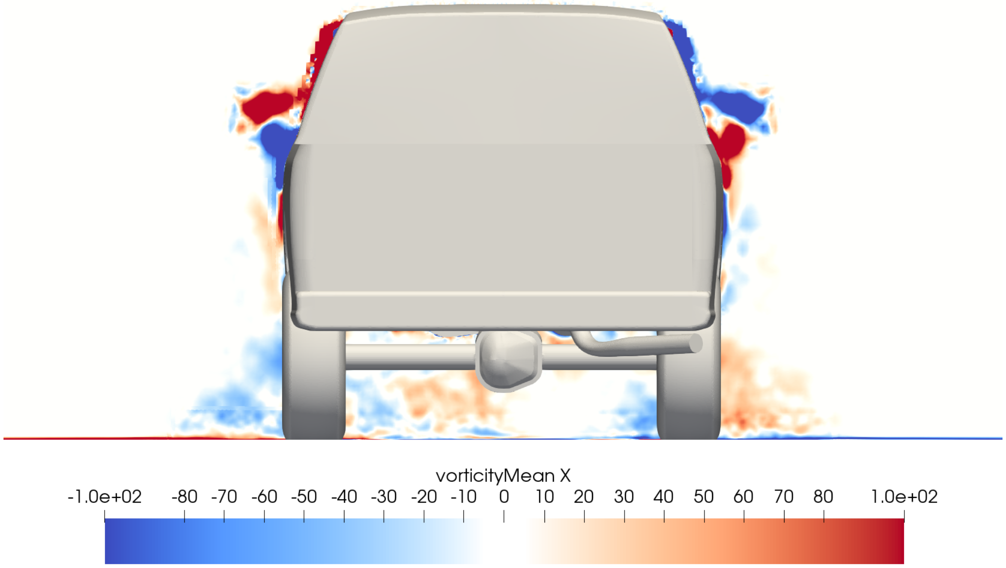

Figure 4.65: Mean x–vorticity $x = -0.5$ slice, DDES.

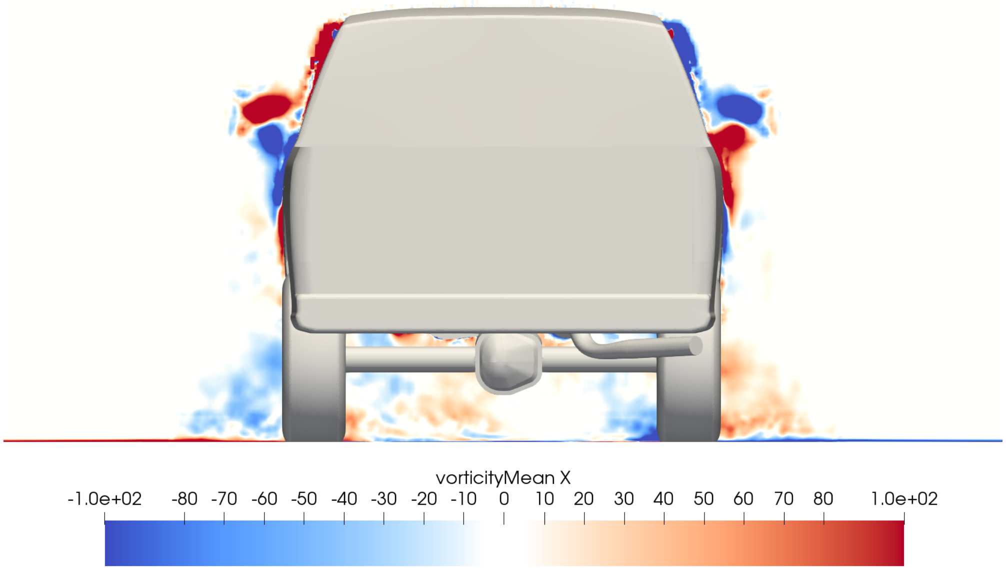

Figure 4.66: Mean x–vorticity $x = -0.5$ slice, IDDES.

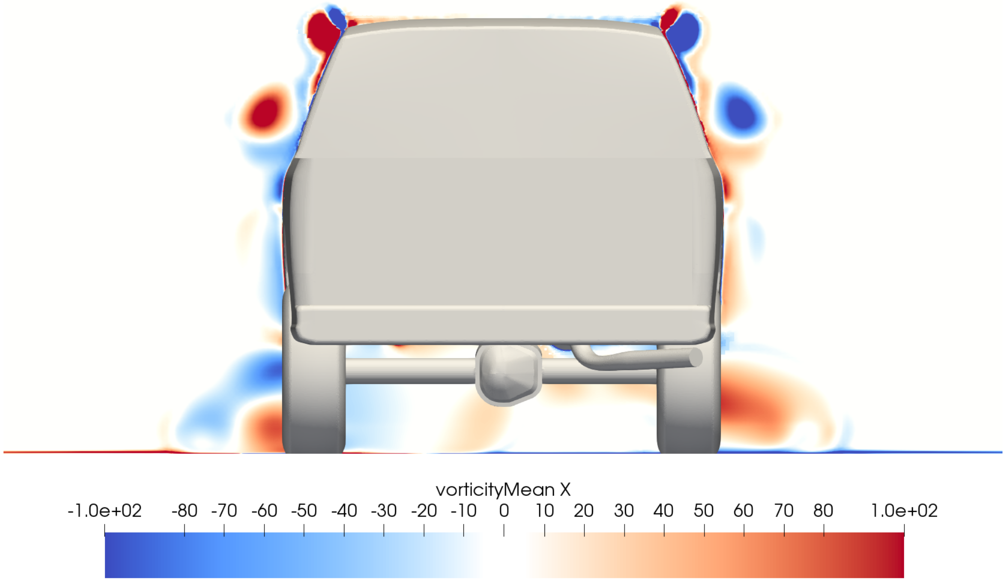

Figure 4.67: Mean x–vorticity $x = 0$ slice, Spalart-Allmaras.

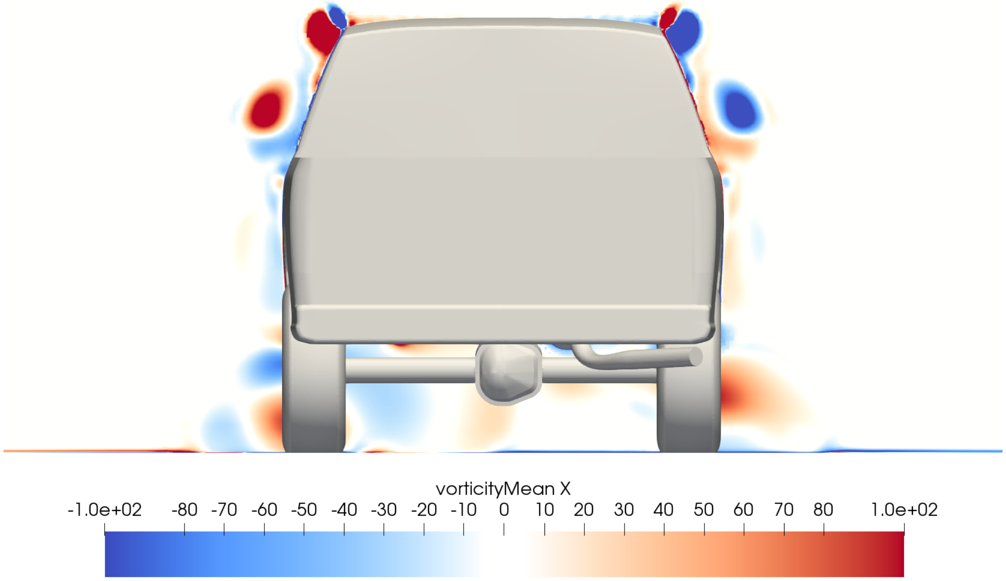

Figure 4.68: Mean x–vorticity $x = 0$ slice, k-omega SST.

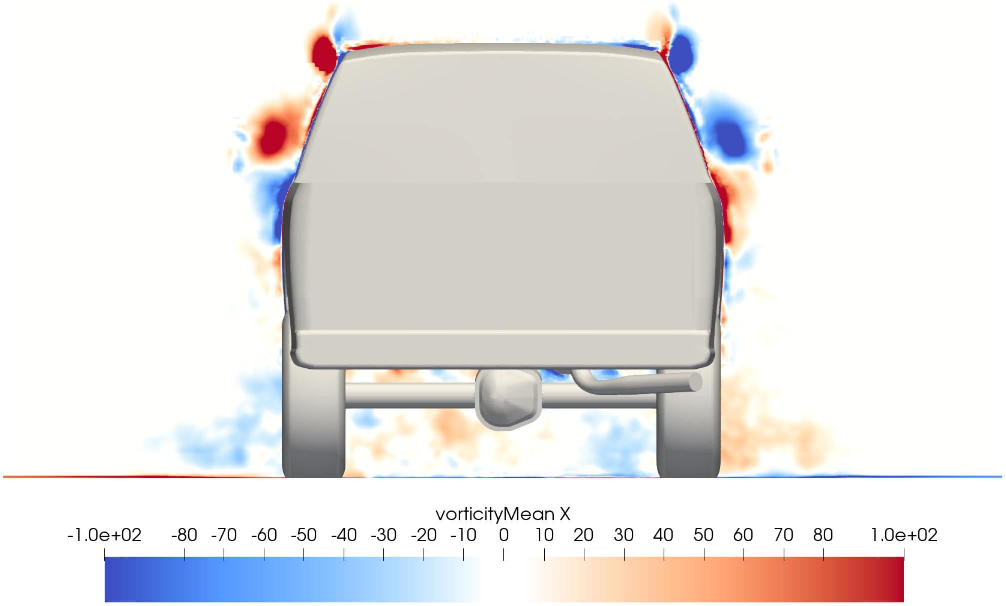

Figure 4.69: Mean x–vorticity $x = 0$ slice, DES.

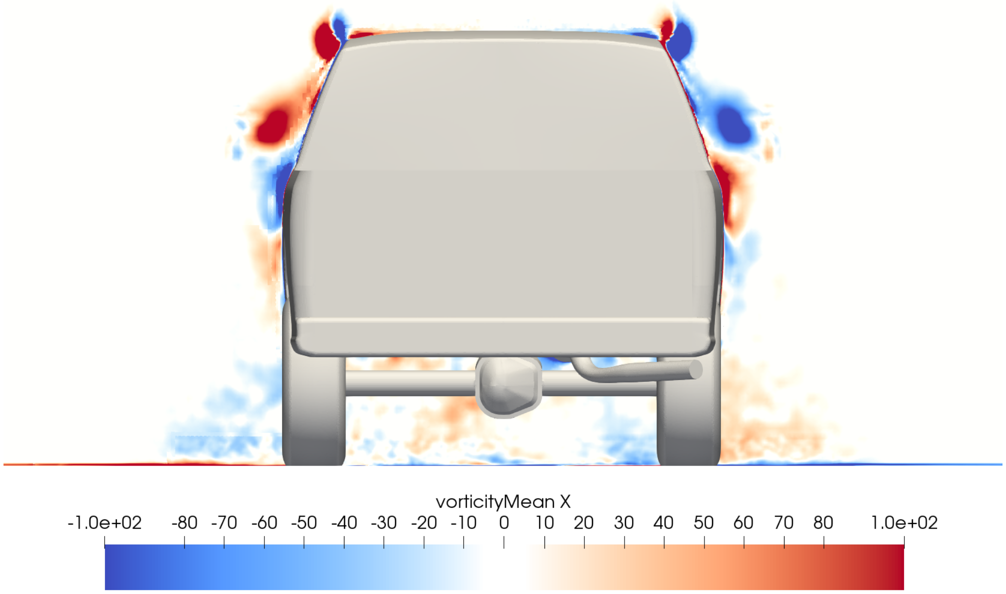

Figure 4.70: Mean x–vorticity $x = 0$ slice, DDES.

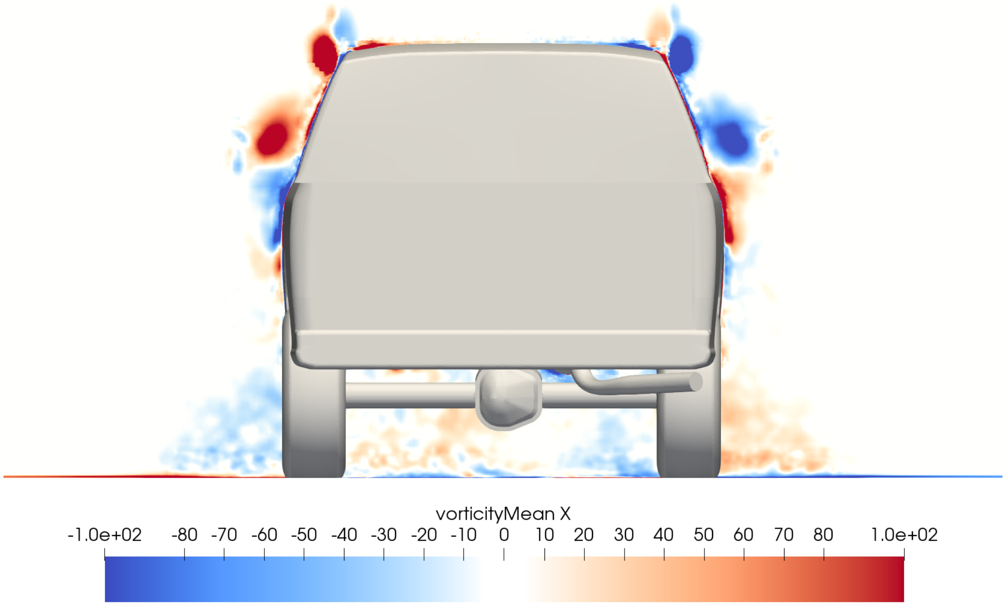

Figure 4.71: Mean x–vorticity $x = 0$ slice, IDDES.

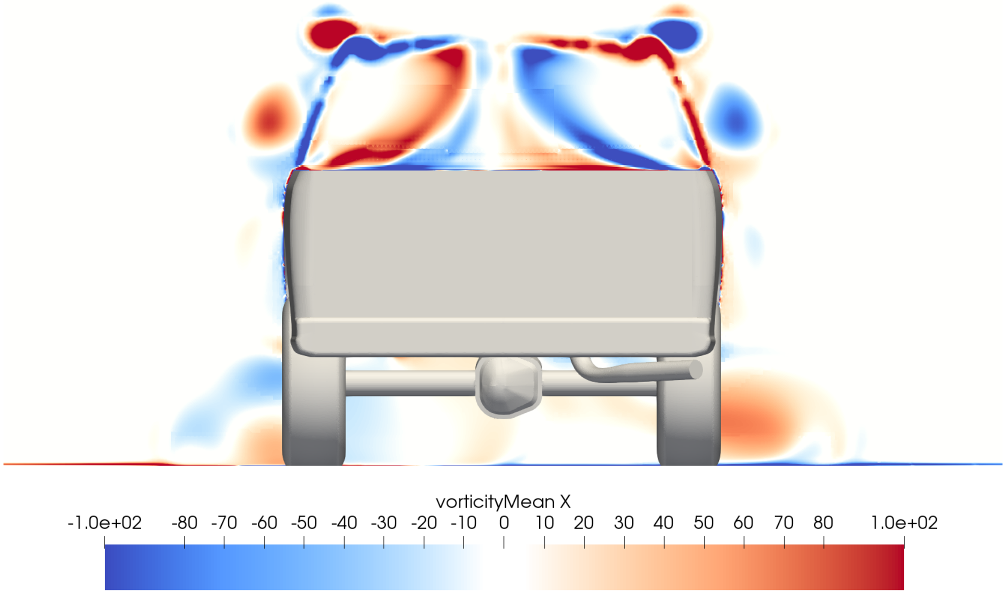

Figure 4.72: Mean x–vorticity $x = 0.5$ slice, Spalart-Allmaras.

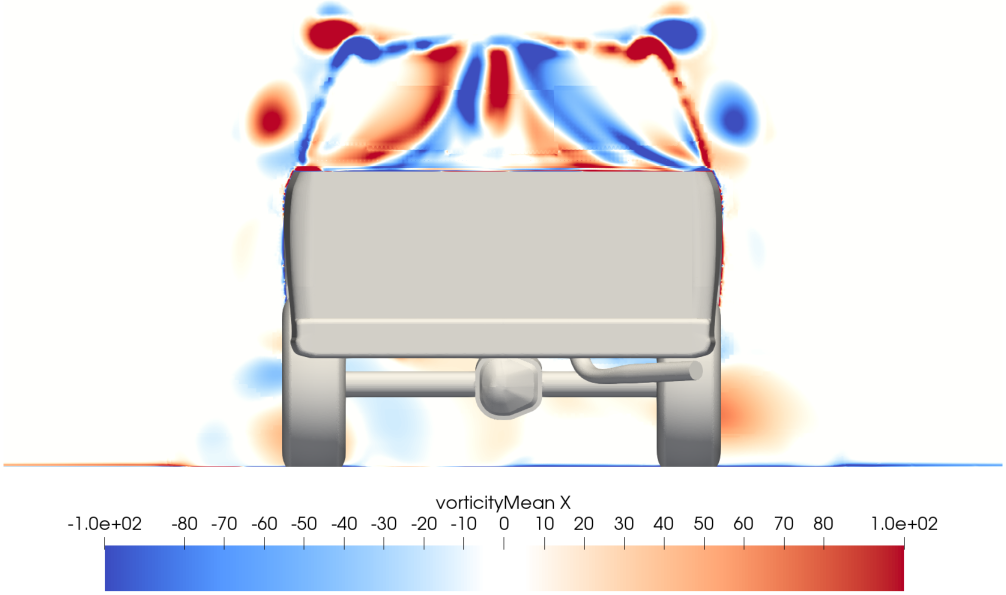

Figure 4.73: Mean x–vorticity $x = 0.5$ slice, k-omega SST.

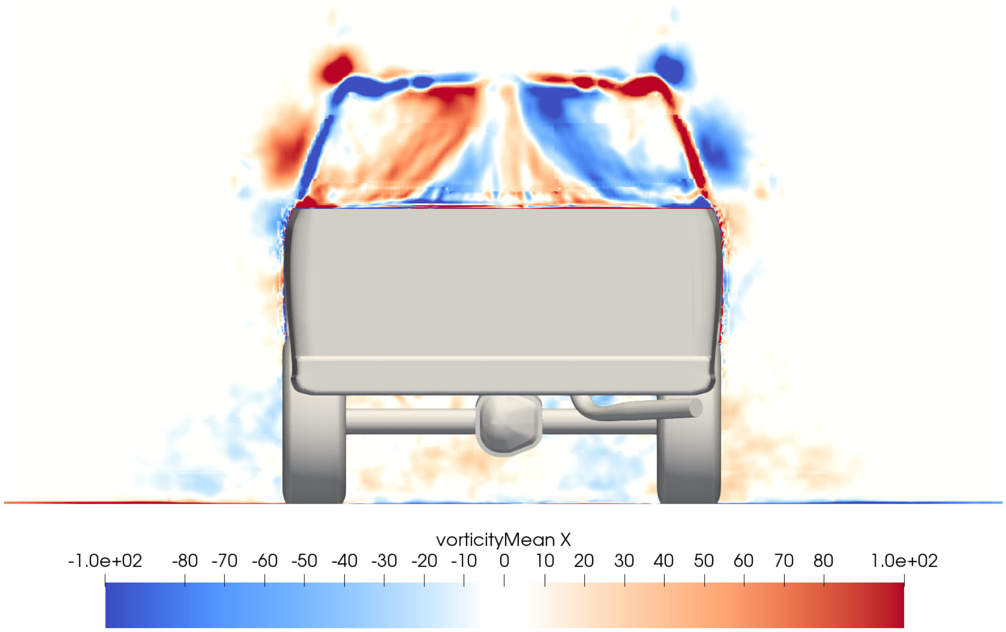

Figure 4.74: Mean x–vorticity $x = 0.5$ slice, DES.

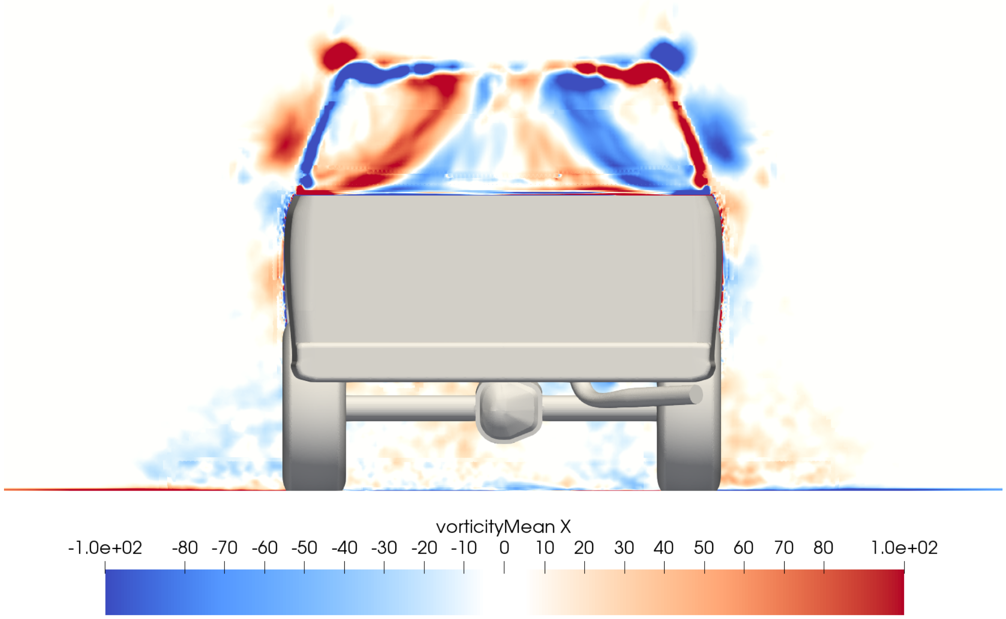

Figure 4.75: Mean x–vorticity $x = 0.5$ slice, DDES.

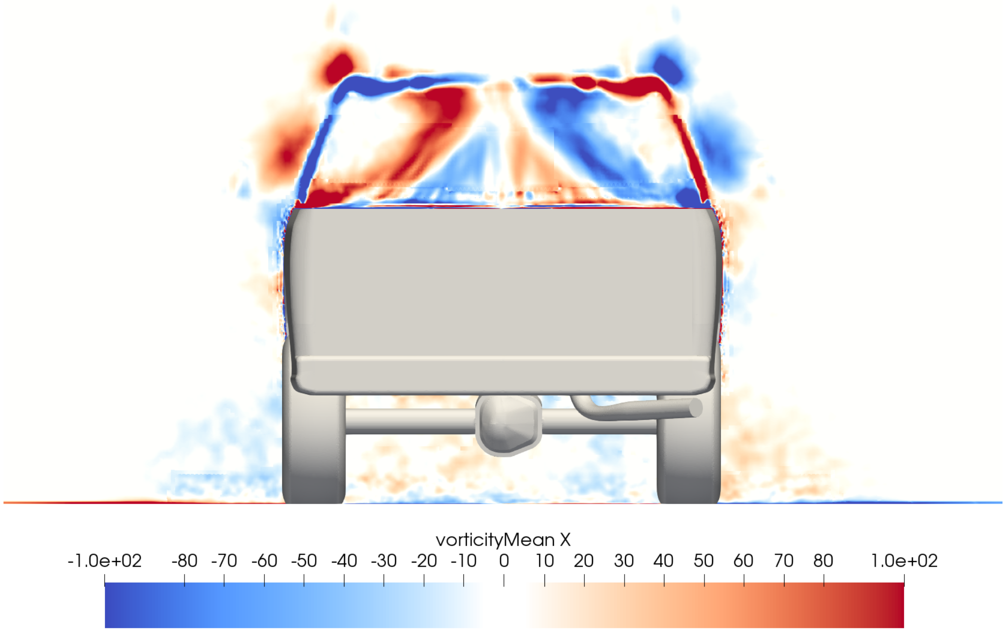

Figure 4.76: Mean x–vorticity $x = 0.5$ slice, IDDES.

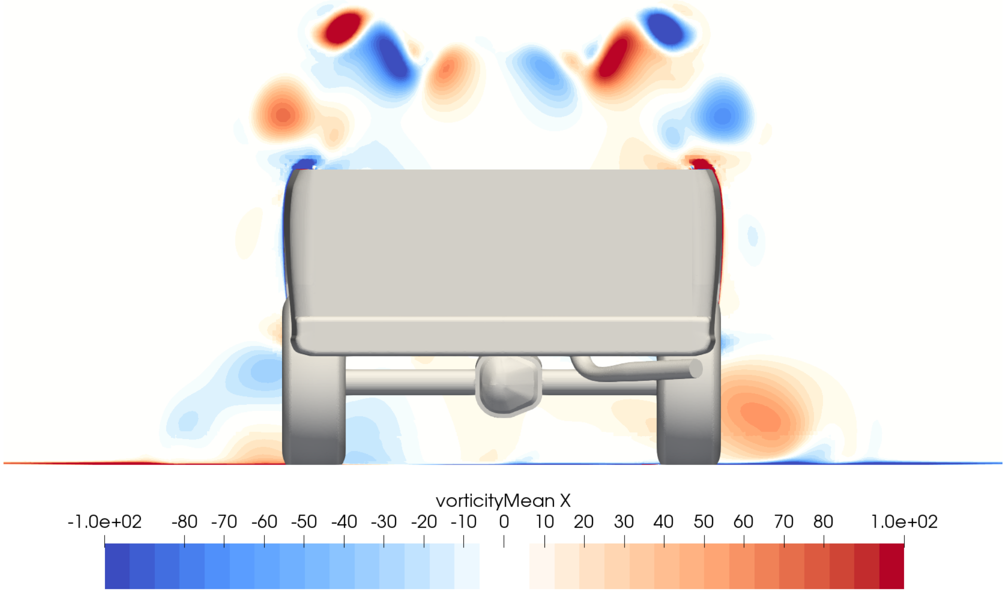

Figure 4.77: Mean x–vorticity $x = 1.0$ slice, Spalart-Allmaras.

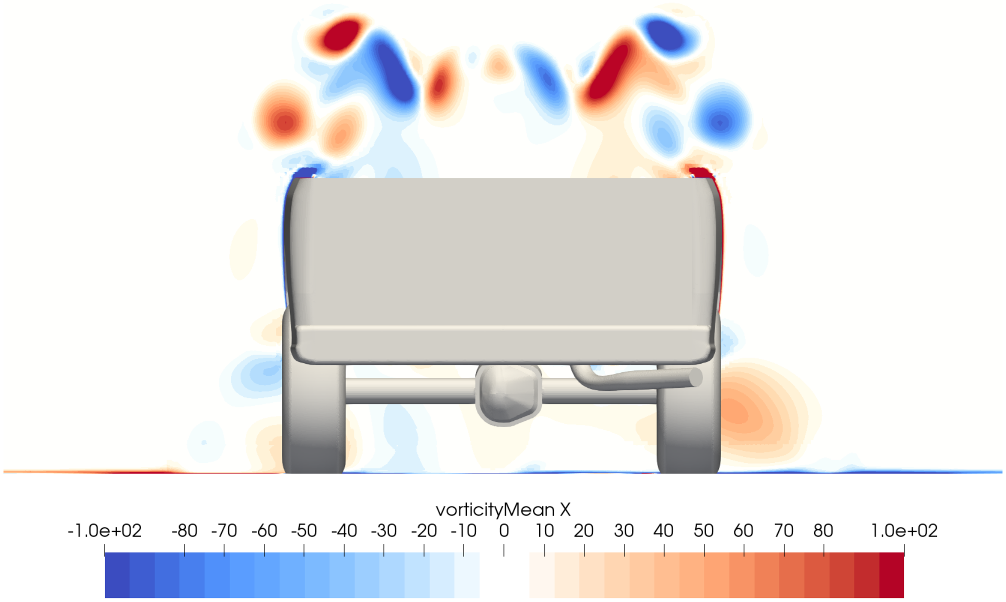

Figure 4.78: Mean x–vorticity $x = 1.0$ slice, k-omega SST.

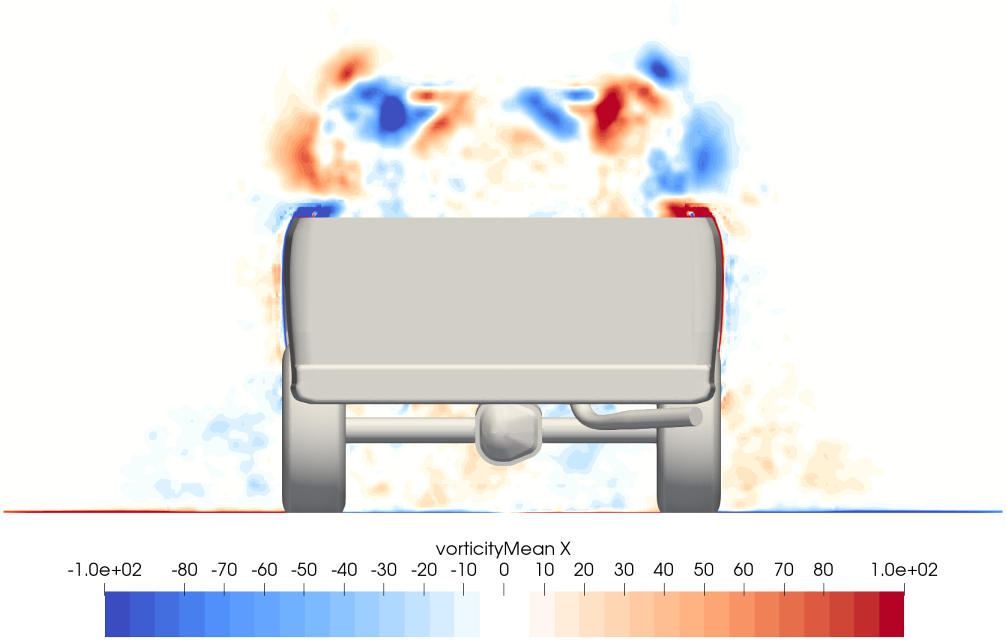

Figure 4.79: Mean x–vorticity $x = 1.0$ slice, DES.

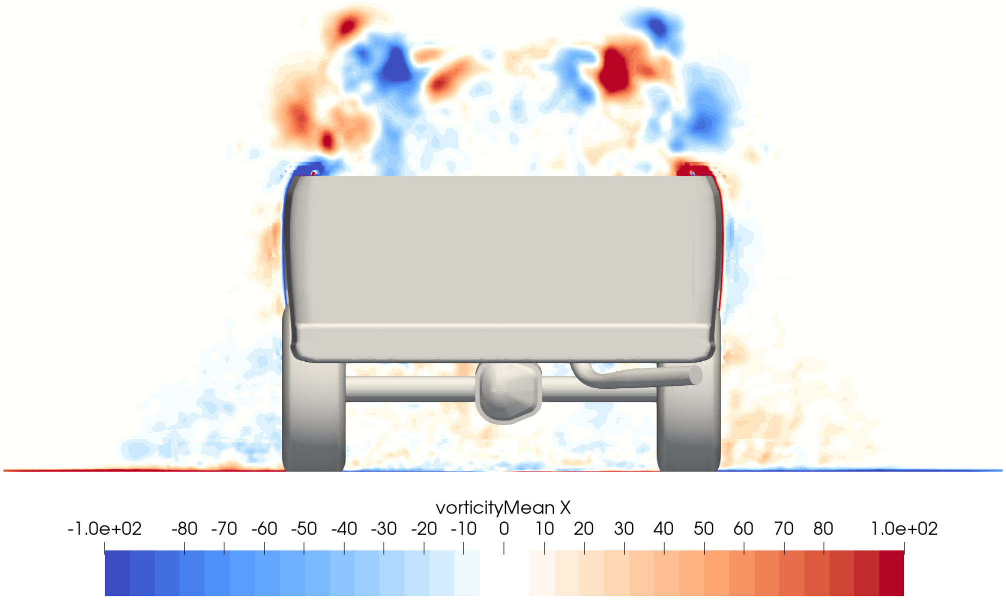

Figure 4.80: Mean x–vorticity $x = 1.0$ slice, DDES.

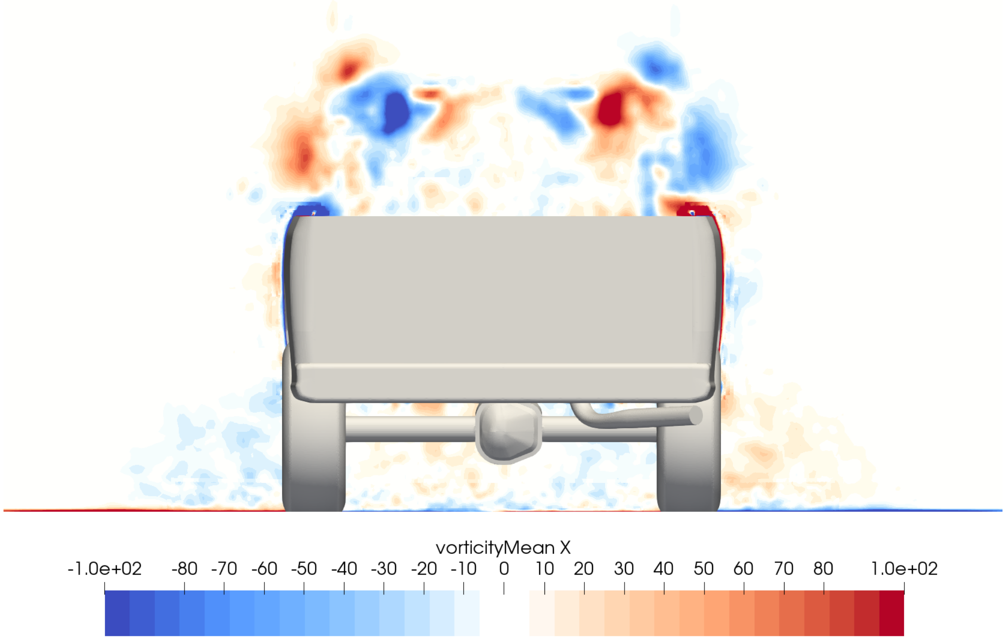

Figure 4.81: Mean x–vorticity $x = 1.0$ slice, IDDES.

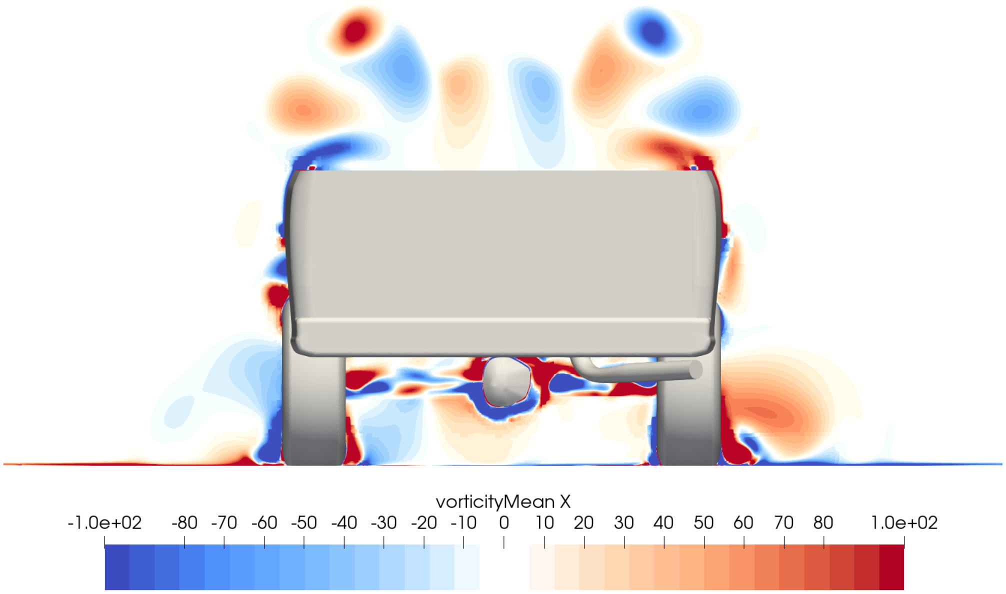

Figure 4.82: Mean x–vorticity $x = 1.5$ slice, Spalart-Allmaras.

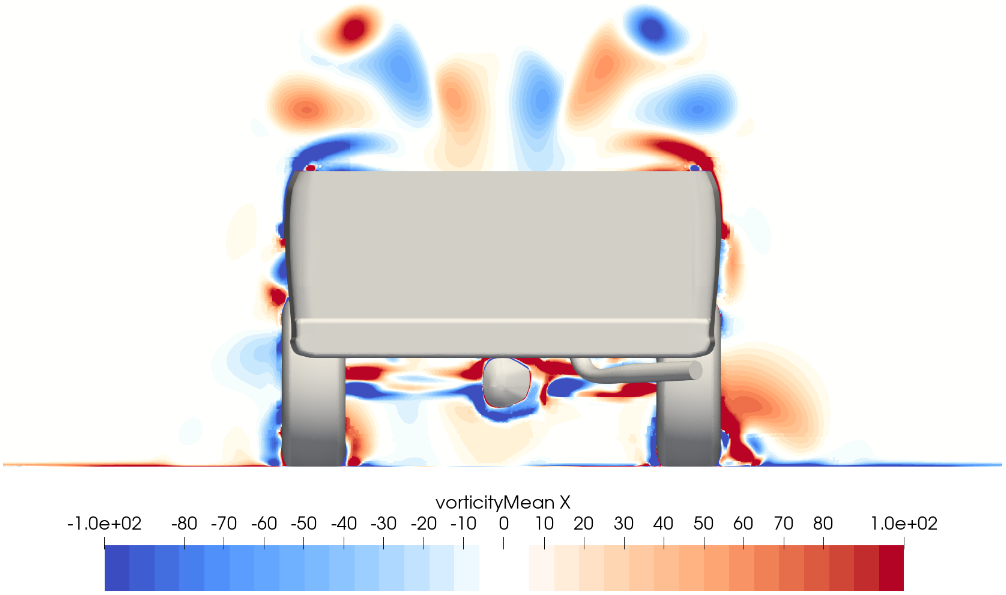

Figure 4.83: Mean x–vorticity $x = 1.5$ slice, k-omega SST.

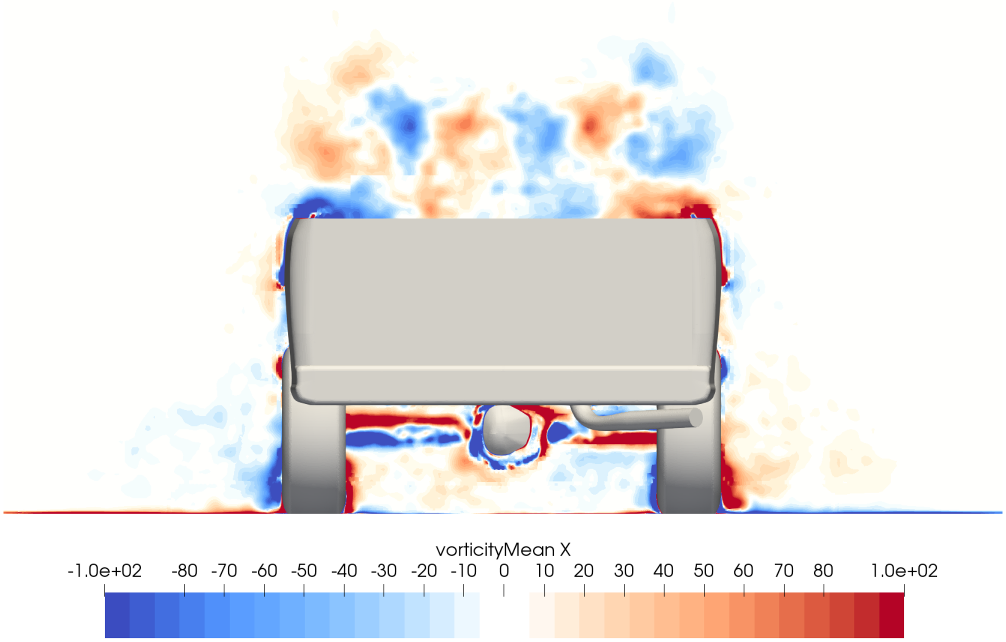

Figure 4.84: Mean x–vorticity $x = 1.5$ slice, DES.

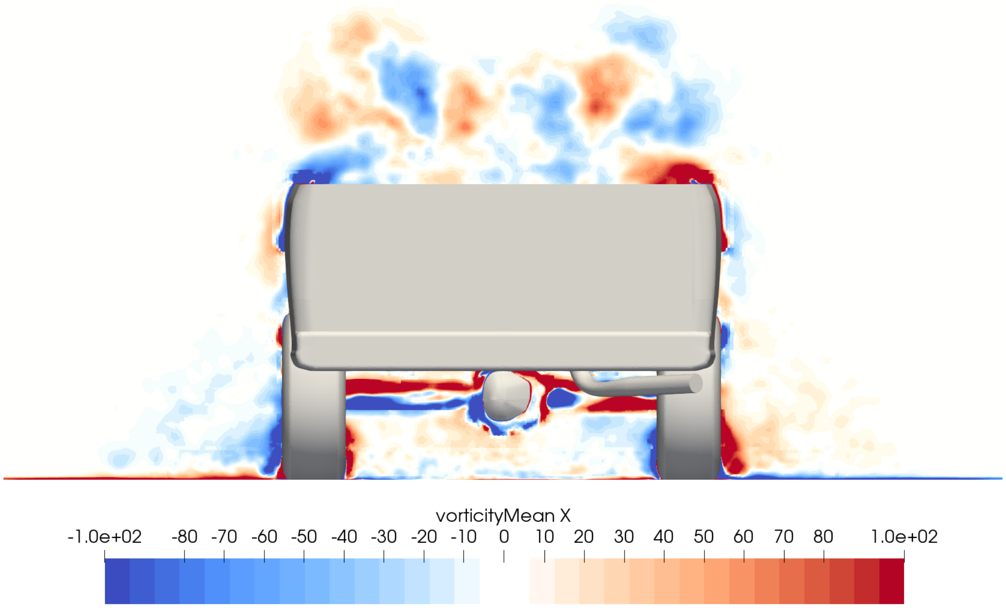

Figure 4.85: Mean x–vorticity $x = 1.5$ slice, DDES.

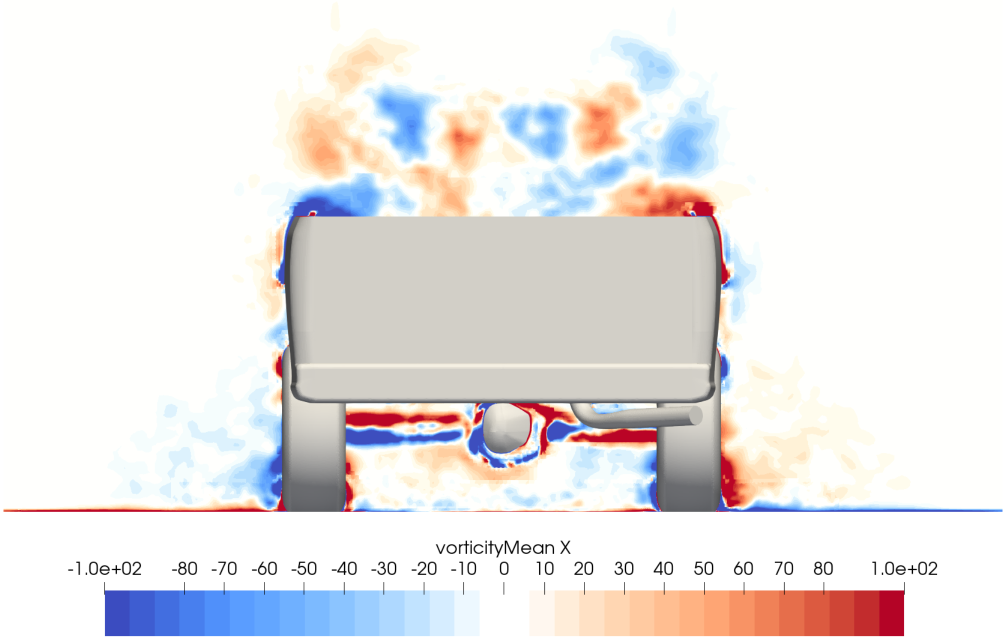

Figure 4.86: Mean x–vorticity $x = 1.5$ slice, IDDES.

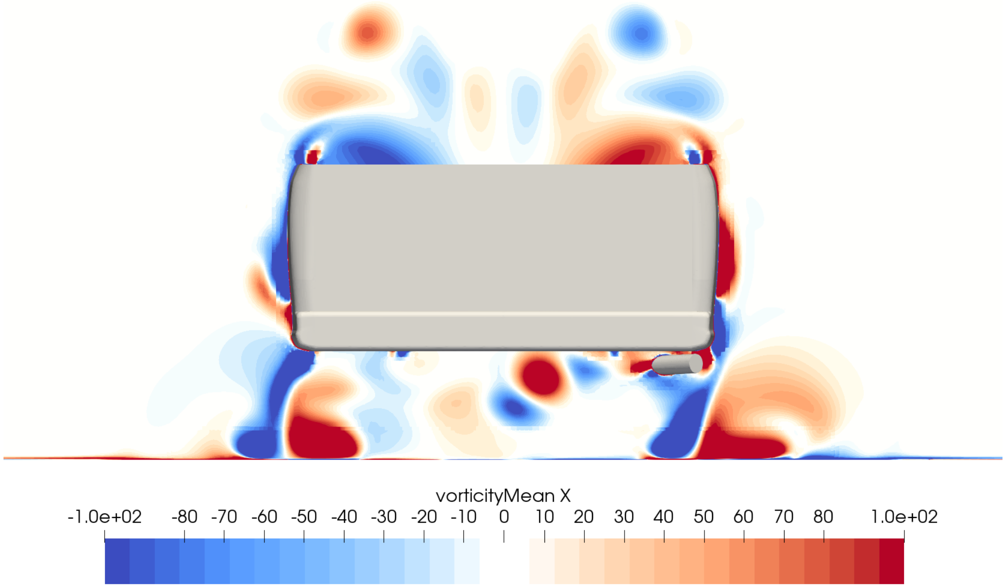

Figure 4.87: Mean x–vorticity $x = 2.0$ slice, Spalart-Allmaras.

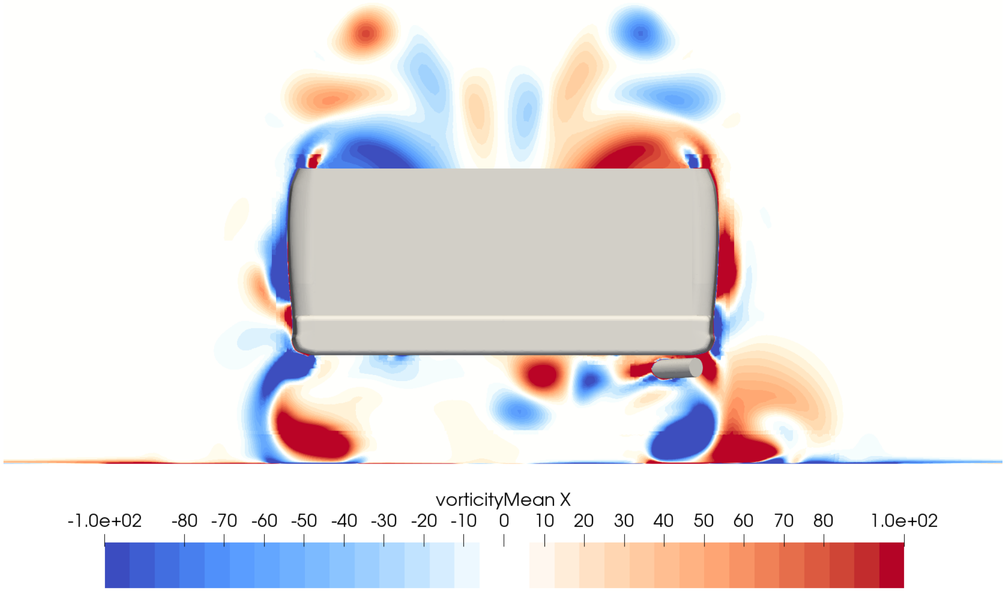

Figure 4.88: Mean x–vorticity $x = 2.0$ slice, k-omega SST.

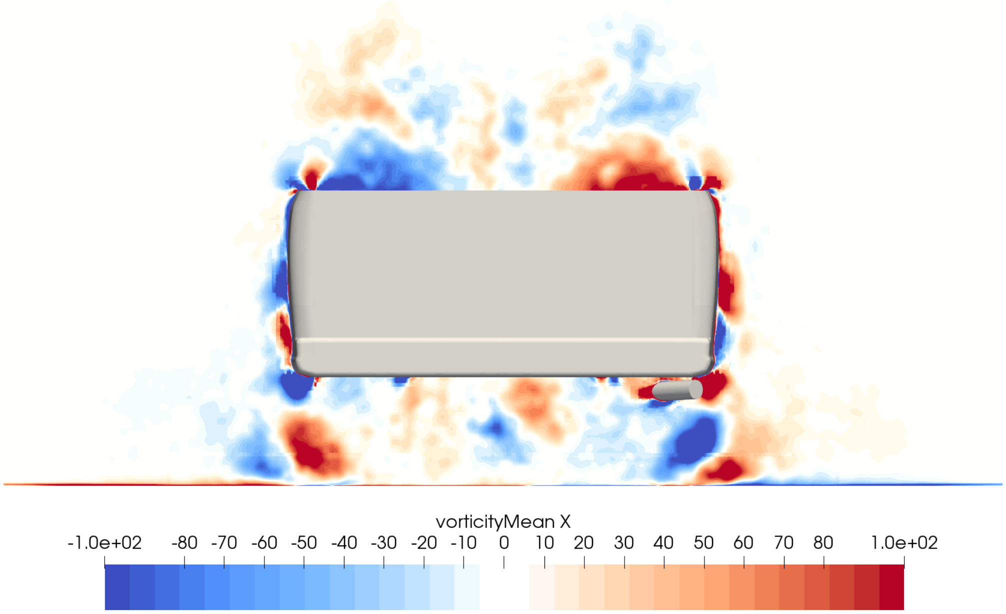

Figure 4.89: Mean x–vorticity $x = 2.0$ slice, DES.

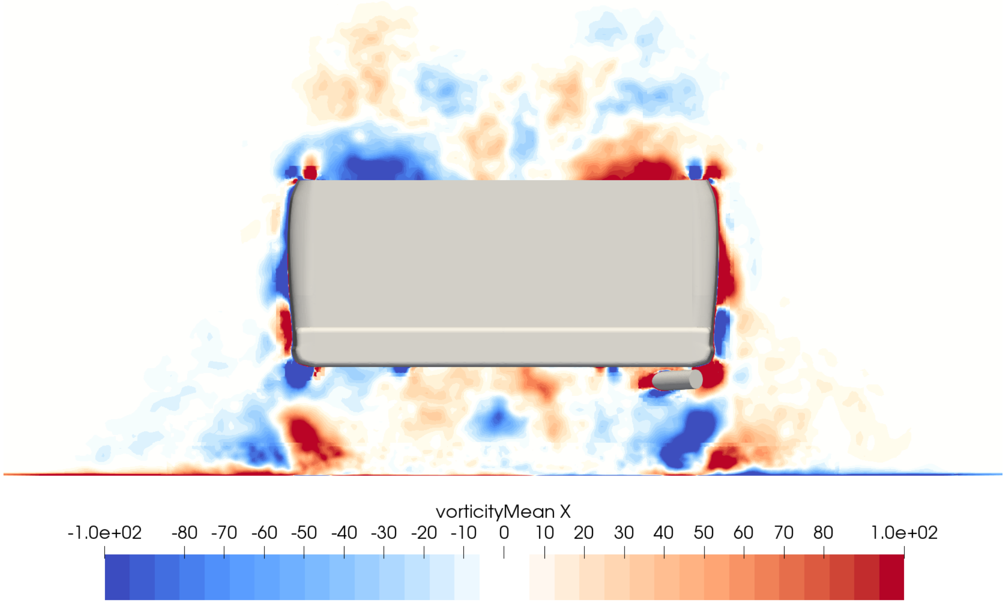

Figure 4.90: Mean x–vorticity $x = 2.0$ slice, DDES.

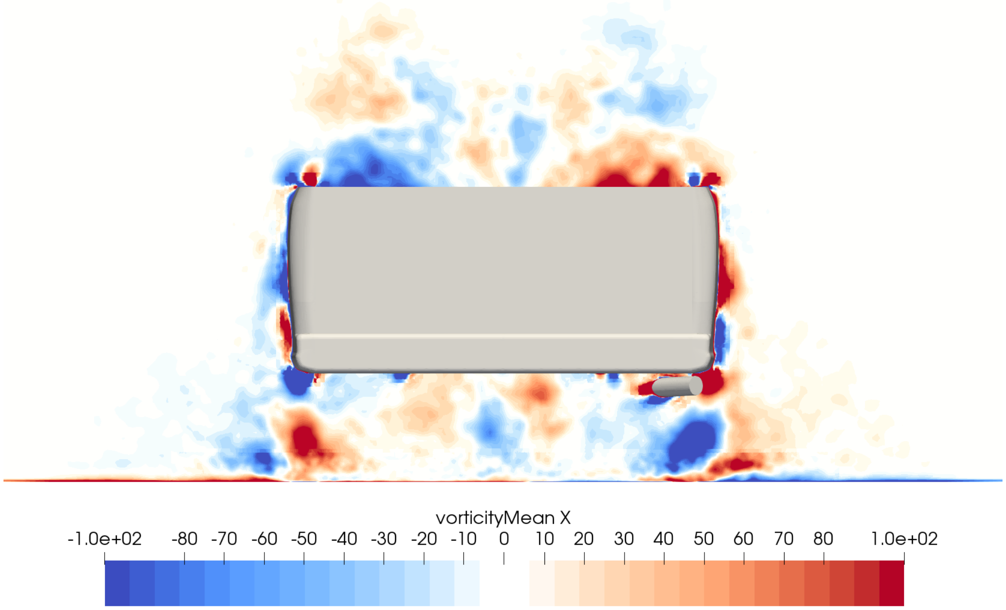

Figure 4.91: Mean x–vorticity $x = 2.0$ slice, IDDES.

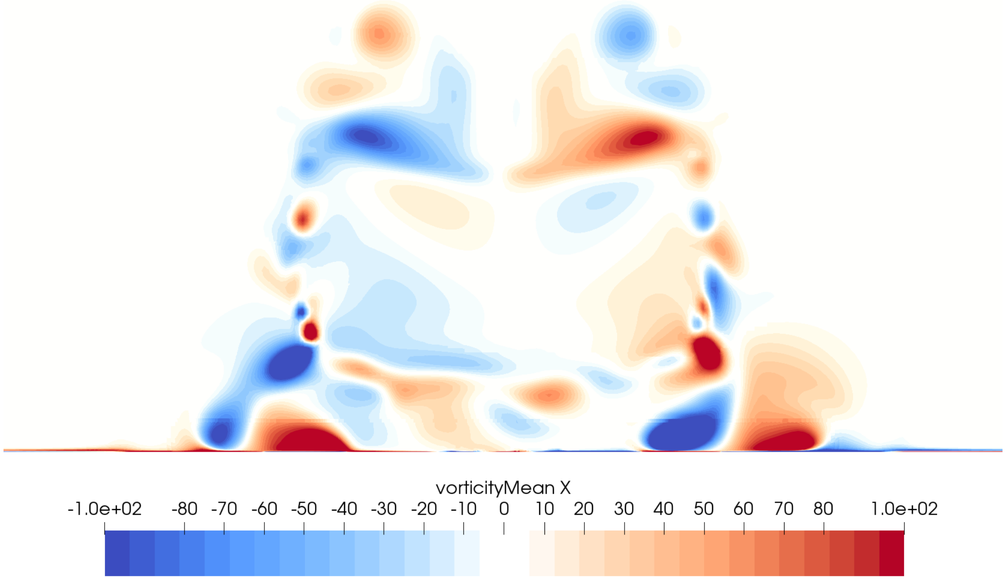

Figure 4.92: Mean x–vorticity $x = 2.5$ slice, Spalart-Allmaras.

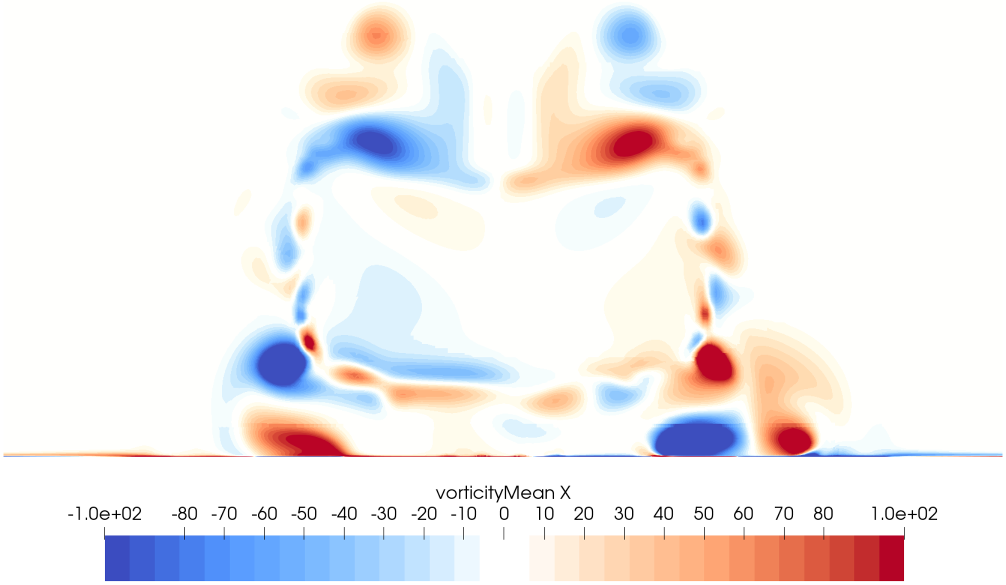

Figure 4.93: Mean x–vorticity $x = 2.5$ slice, k-omega SST.

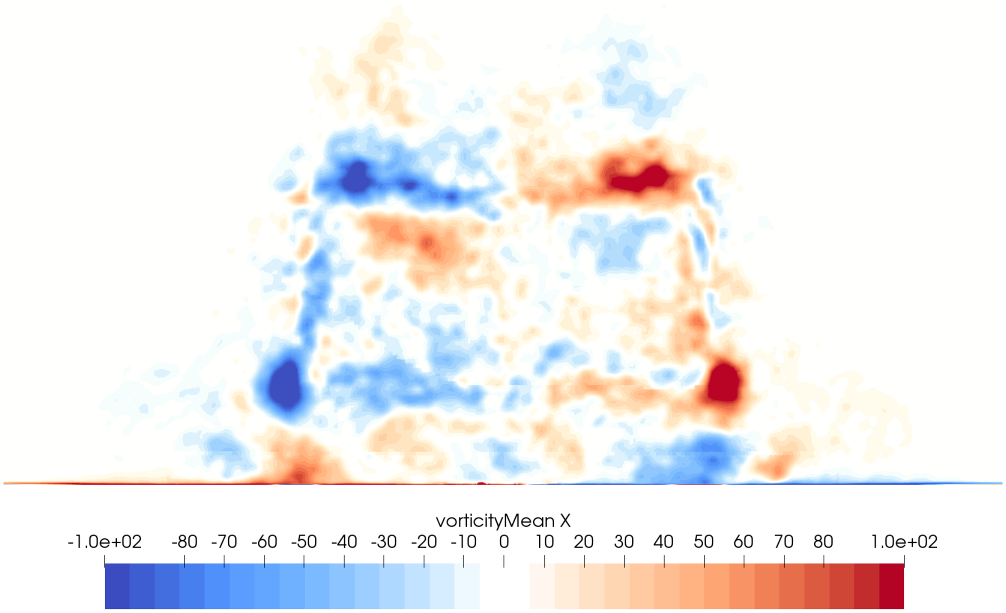

Figure 4.94: Mean x–vorticity $x = 2.5$ slice, DES.

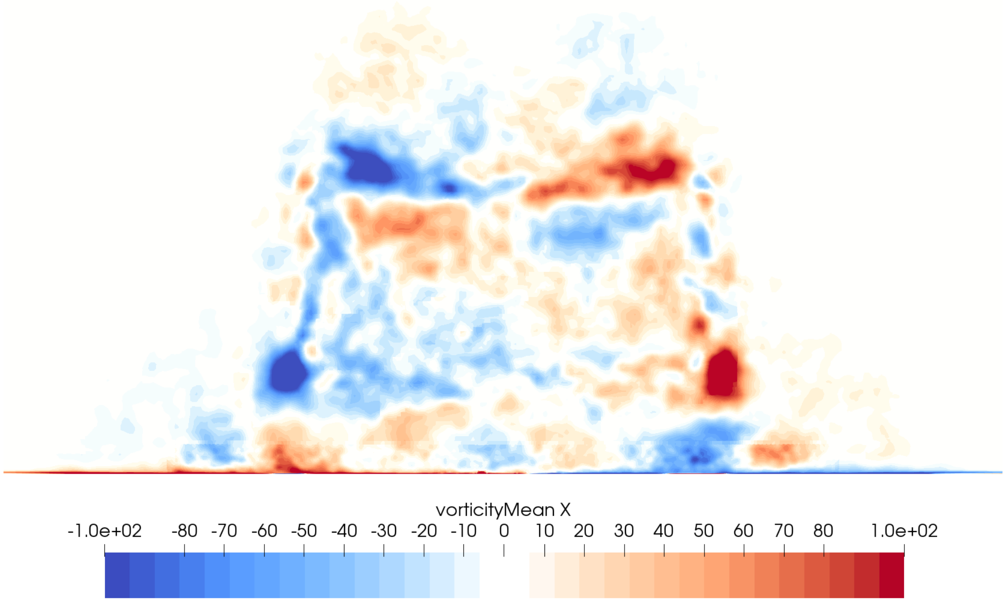

Figure 4.95: Mean x–vorticity $x = 2.5$ slice, DDES.

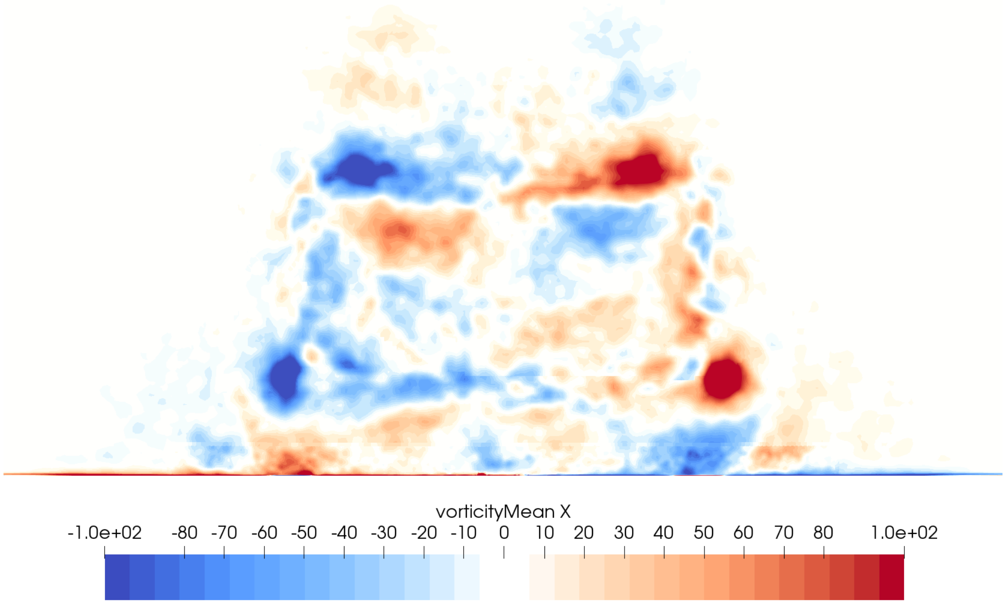

Figure 4.96: Mean x–vorticity $x = 2.5$ slice, IDDES.

reverses flow. To visualize this, the surface shear stress is plotted. Figures 4.97 to 4.101 show flow detachment from the mirror and wheel wakes. The shape of the detachment zone is quite different between Spalart Allmaras RANS and DES: curiously, the Spalart-Allmaras detachment zones seem to ”streak” across the entire truck, whereas in DES the flow reattaches some distance downstream. This also holds true for the wheel wakes. The A-pillar vortex re-attachment line appears similar across all models on the driver side window. The top view in Figures 4.102 to 4.106 unsurprisingly shows completely detached flow in the bed. Across turbulence models, there is no difference in flow detachment behavior on the rear header of the roof. Finally, from Figures 4.107 to 4.111, we see that the underbody flow is highly detached due to the lack of component shielding.

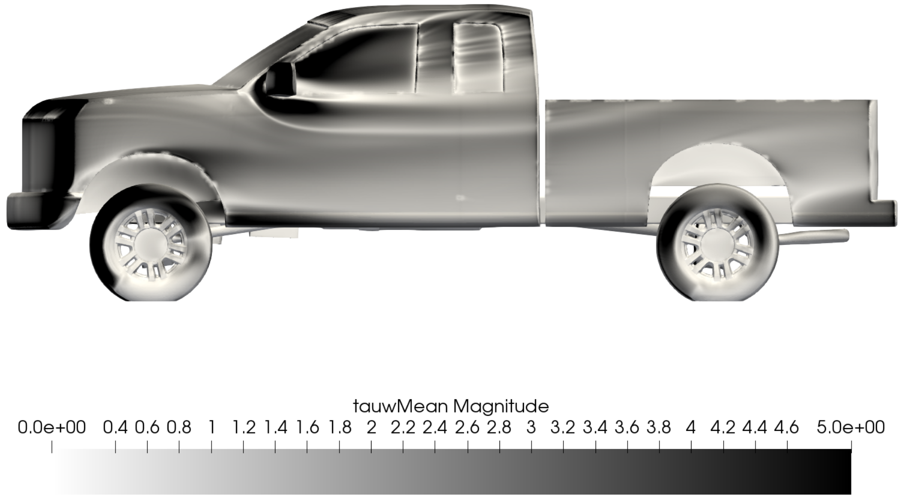

Figure 4.97: Surface shear stress, side, Spalart-Allmaras.

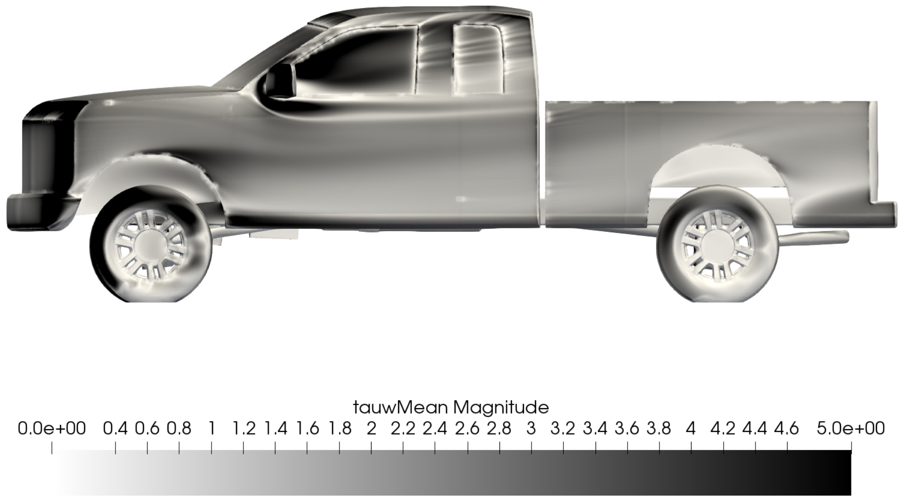

Figure 4.98: Surface shear stress, side, k-omega SST.

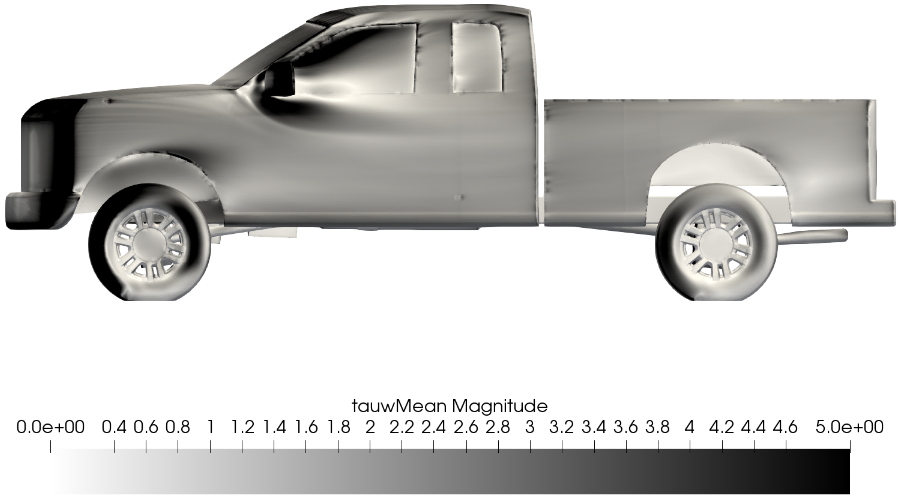

Figure 4.99: Surface shear stress, side, DES.

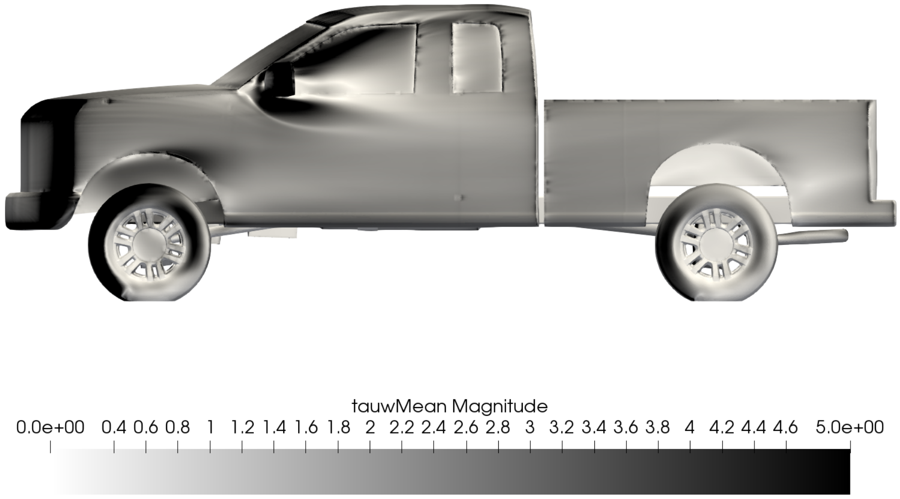

Figure 4.100: Surface shear stress, side, DDES.

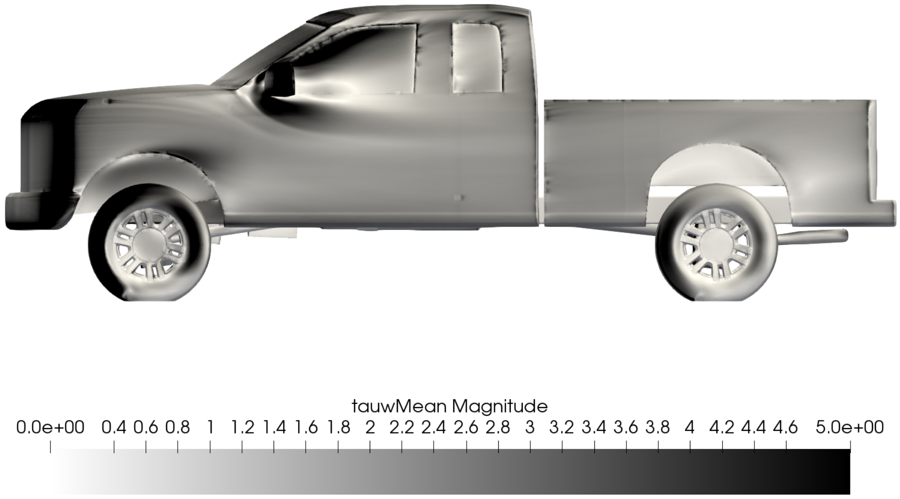

Figure 4.101: Surface shear stress, side, IDDES.

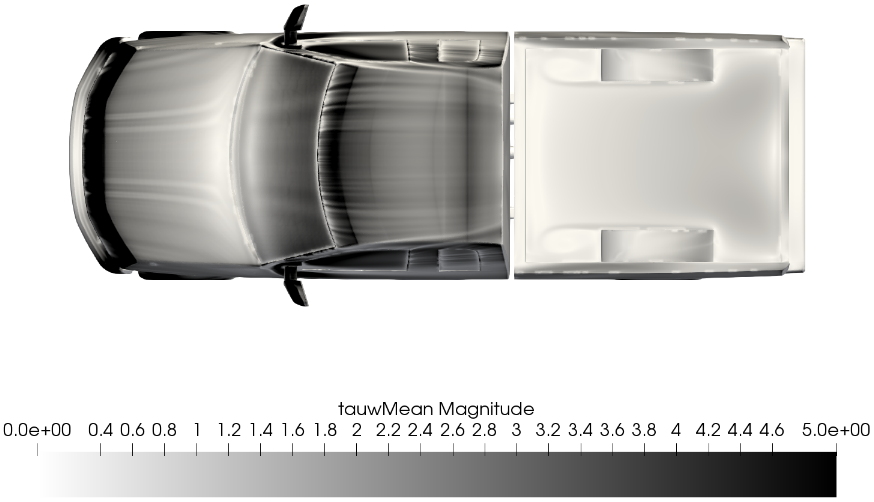

Figure 4.102: Surface shear stress, top, Spalart-Allmaras.

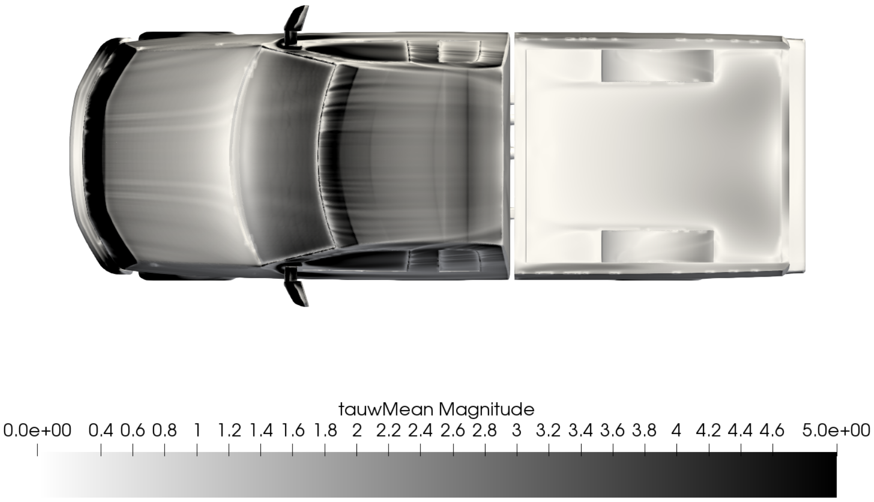

Figure 4.103: Surface shear stress, top, k-omega SST.

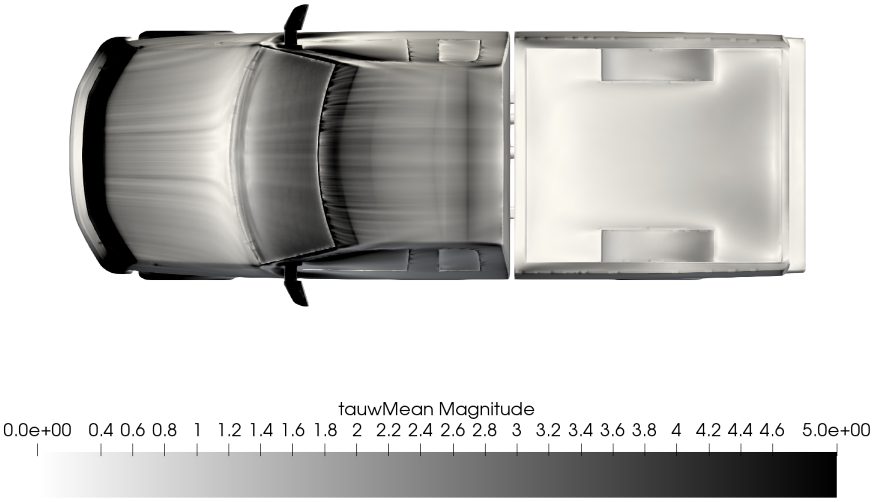

Figure 4.104: Surface shear stress, top, DES.

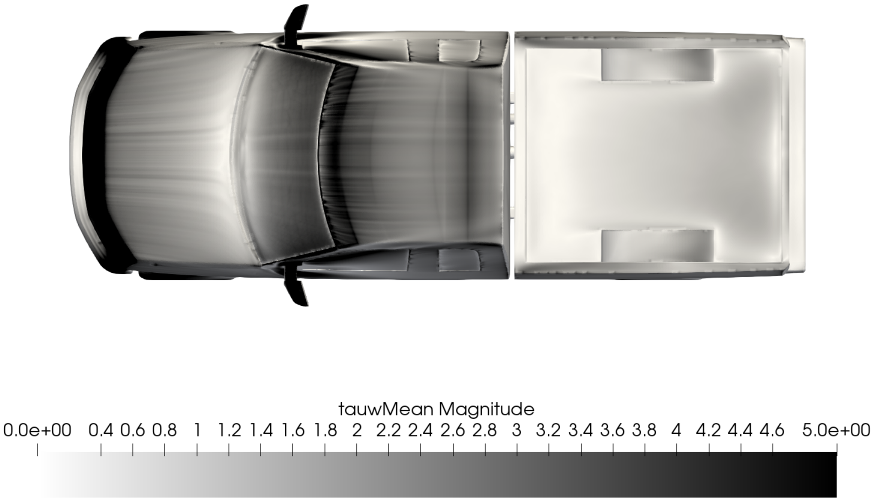

Figure 4.105: Surface shear stress, top, DDES.

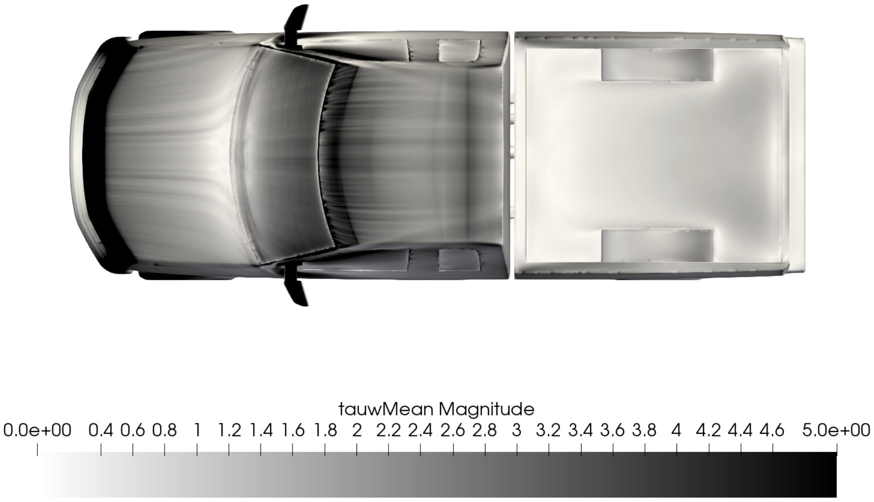

Figure 4.106: Surface shear stress, top, IDDES.

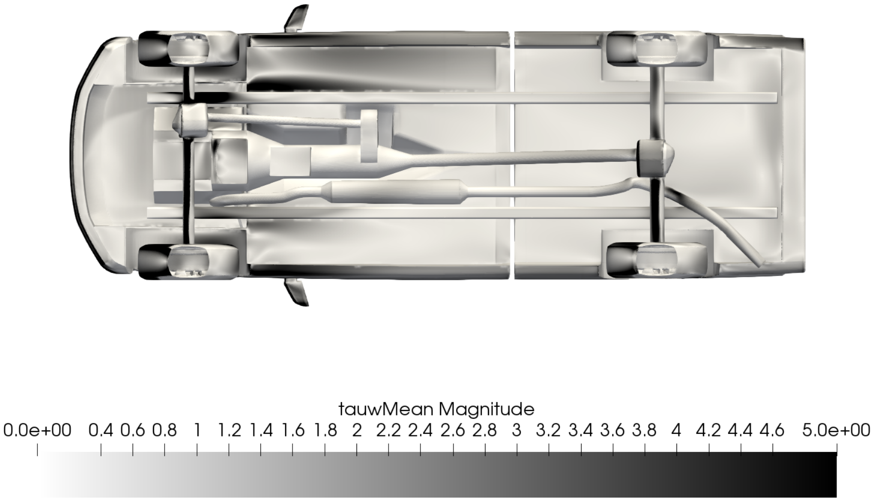

Figure 4.107: Surface shear stress, bottom, Spalart-Allmaras.

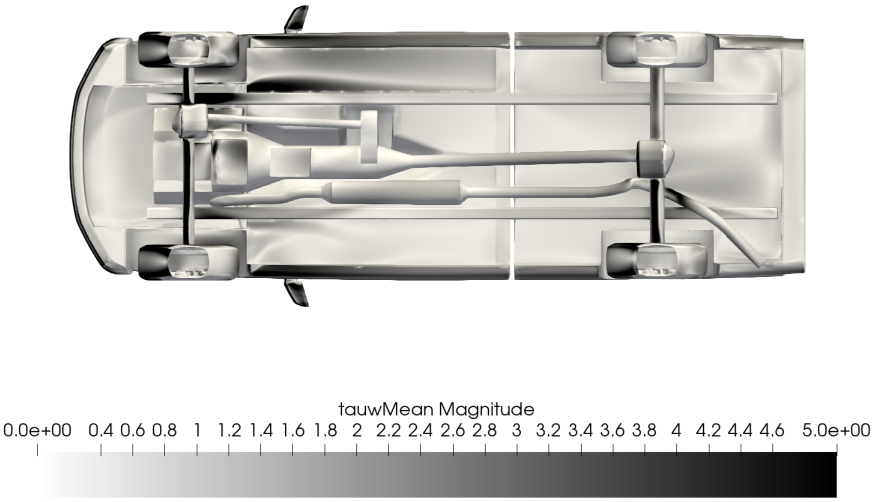

Figure 4.108: Surface shear stress, bottom, k-omega SST.

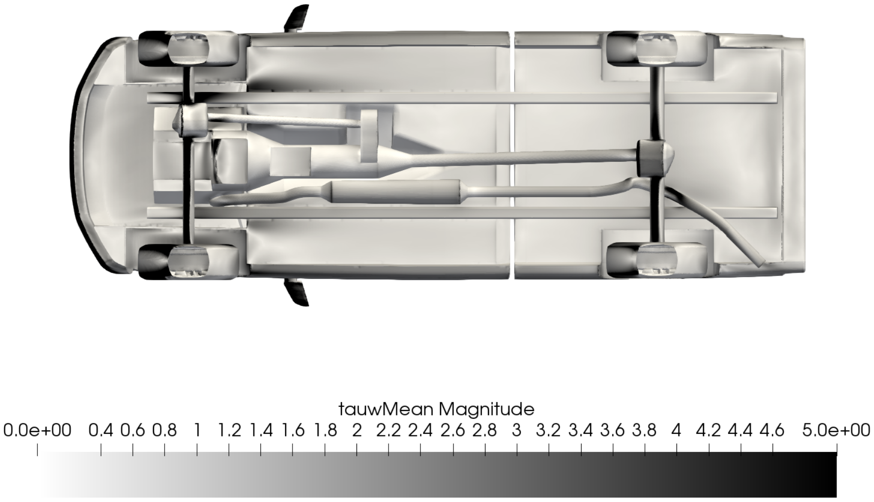

Figure 4.109: Surface shear stress, bottom, DES.

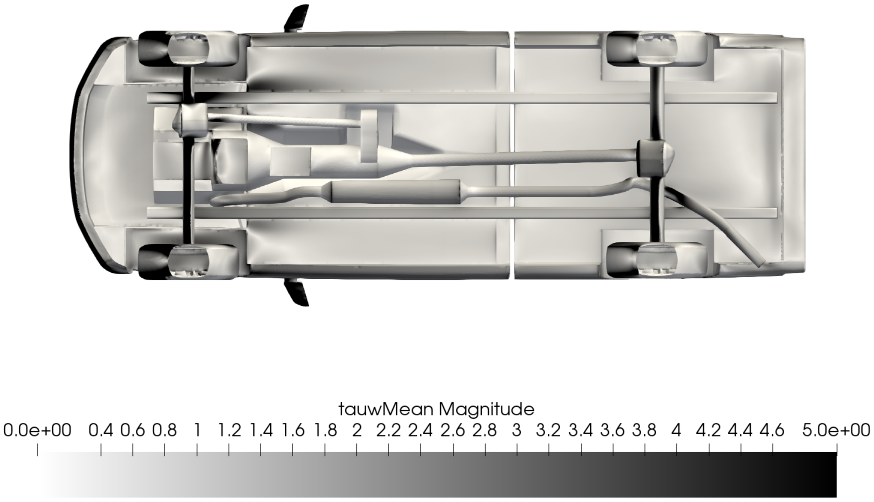

Figure 4.110: Surface shear stress, bottom, DDES.

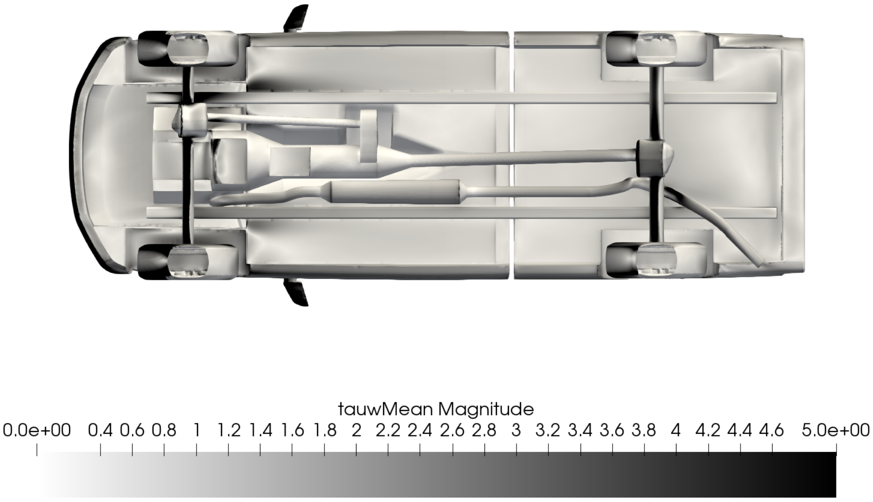

Figure 4.111: Surface shear stress, bottom, IDDES.

CHAPTER V: CONCLUSIONS

In this study, three hybrid RANS-LES turbulence models—DES, DDES, and IDDES—were evaluated in an external aerodynamics CFD simulation of a simplified truck shape. The results were compared to the Spalart-Allmaras and k-omega SST steady-state RANS models. The hybrid models yielded similar force coefficients, with both C_d and C_l within 0.002 C_d and 0.014 C_l for all three. The hybrid models also predicted C_d and C_l 0.040 C_d and 0.078 C_l higher on average than the steady RANS models, respectively. Surface C_p and near wall velocity were similar between all the models on the front fascia, hood, windshield, and front half of the front wheel wells. However they begin to differ downstream of these regions. In particular, surface C_p in highly-detached zones were significantly different between the RANS and hybrid models. This occurred in critical areas such as the back of the cab and tailgate, which are large contributors to C_d. Similarly, C_l was strongly affected by the change in underbody C_p development. Reattachment behavior also differed, most notably in the mirror wake on the front door windows.

Several flow features such as the front wheel wakes, underbody center jet, and A-pillar vortices seemed to dissipate much slower in RANS: in some cases, their streamwise length was doubled. The flow structures behind the rear tires were in some cases completely different. Some structures were present around the rear tires only in RANS; conversely, there was a horizontal vortex rolling off the tailgate that was completely absent in RANS.

Flow field differences between DES, DDES, and IDDES were few and subtle. There were no significant alterations in flow structures between them, and the surface C_p fields were nearly identical. Though the three models are fundamentally different and increasingly complex, the common DES strategy and use of Spalart-Allmaras made the results similar. Looking at the differences between the models, we might expect to find differences where there was adverse pressure gradient driven separation, due to problems with modeled stress depletion in DES. However, the general boxiness of the truck shape and its relatively shallow curvature meant that separation was instead dictated by trailing edges. In contrast, we might expect to see differences on the rear glass of the notchback vehicle shown in Figure 2.5, which has a steeper angle.

An important component missing from this study is the wind tunnel. While we do have a general idea of which schemes are better in CFD from first principles and numerical analysis, without comparision to physical test results, it is difficult to gauge the true performance of each turbulence model. On a basic level, it is useful to compare overall force coefficients obtained in the tunnel to those seen in CFD, and simply see which is closer. However, this metric is deceptive because in CFD, areas with overpredicted forces can cancel out underpredicted forces, giving a false sense of security. A better correlation technique is pressure data obtained through taps or sensors, either on the surface or out in the flow. This enables confirmation of which areas of the vehicle have forces being predicted correctly, and the others that fall short. This feedback is more valuable because it narrows the scope of investigation to problem areas in the CFD model.

Flow visualization techniques such as surface oil streaks allow engineers to see surface flow topology and—critically—separation lines. Comparing separation behavior in the tunnel to CFD confirms whether boundary layer development is being predicted correctly, which is linked directly to the turbulence model. Finally, particle image velocimetry (PIV) allows direct visualization of the instantaneous U field with lasers. In CFD, each turbulence model will predict flow structures differently. As seen in the results of this study, some structures come completely into and out of existence depending on the turbulence model. The only way to validate which structures are real, and which turbulence model is predicting them correctly, is by using PIV or related techniques.

For all the changes caused by turbulence models, the force coefficients and flow fields are somewhat similar, and so one could argue that the choice of turbulence model is not important. From the results however, we see that the flow fields are fundamentally changed by the choice of turbulence model. Notice that regions of the flow field which were sensitive to the choice of turbulence model tended to overlap with important design areas on the truck. Transient solutions take significantly longer to compute than RANS solutions: on the basis of number of steps, each RANS solution in this study took 6,000 steps, whereas the transient solutions required 20,000 steps. It is tempting to run cheaper RANS solutions at the cost of physical realism, but ultimately the effort is a waste if the CFD results are compromised by a turbulence model that performs poorly. While I hypothesize that the transient hybrid RANS-LES models are more realistic than RANS due to first principles, the vehicle must be physically tested to confirm this.

To continue this study, the most important matter is to obtain wind tunnel results, with accompanying pressure data and flow visualization. There are also several more hybrid RANS-LES models to evaluate. Of the DES-type, there are variants that substitute Spalart-Allmaras with more sophisticated models such as k-omega SST. There is also Partially-Averaged Navier-Stokes (PANS), which attempts to smoothly blend together modeled and resolved turbulence instead of using discrete switching as in DES. Hybrid RANS-LES turbulence models are a popular and successful turbulence modeling approach for automotive aerodynamics, and they will likely continue to be used until computing power grows enough to enable industrial LES simulations.

BIBLIOGRAPHY

[1] O. Zikanov. *Essential Computational Fluid Dynamics*. Wiley, 2010.

[2] P. R. Spalart and S. R. Allmaras. “A one-equation turbulence model for aerodynamic flows”. In: *30th aerospace sciences meeting and exhibit* (1992), p. 439.

[3] F. R. Menter. “Improved Two-Equation k–ω Turbulence Models for Aerodynamic Flows”. In: *NASA Technical Memorandum 103975* (Oct. 1992), p. 31.

[4] D. C. Wilcox. “Reassessment of the scale-determining equation for advanced turbulence models”. In: *AIAA Journal* 26.11 (Nov. 1988), pp. 1299–1310.

[5] F. R. Menter and T. Esch. “Elements of Industrial Heat Transfer Predictions”. In: *16th Brazilian Congress of Mechanical Engineering* (Nov. 2001), p. 127.

[6] J. Lee and H. Choi. “A dynamic global subgrid-scale model for large eddy simulation of scalar transport in complex turbulent flows”. In: *Journal of Mechanical Science and Technology* 26.12 (Dec. 2012), pp. 3803–3810.

[7] J. Smagorinsky. “General Circulation Experiments with the Primitive Equations”. In: *Monthly Weather Review* 91.3 (1963), pp. 99–164.

[8] P. R. Spalart, W-H Jou, M. L. Strelets, et al. “Comments on the Feasibility of LES for Wings, and on a Hybrid RANS/LES Approach”. In: *Proceedings of first AFOSR international conference on DNS/LES* (Jan. 1997).

[9] P. R. Spalart, S. Deck, M. L. Shur, et al. “A New Version of Detached-eddy Simulation, Resistant to Ambiguous Grid Densities”. In: *Theoretical and Computational Fluid Dynamics* 20.3 (May 2006), p. 181.

[10] M. L. Shur, P. R. Spalart, M. Kh. Strelets, et al. “A hybrid RANS-LES approach with delayed-DES and wall-modelled LES capabilities”. In: *International Journal of Heat and Fluid Flow* 29.6 (2008), pp. 1638–1649.

[11] S.R. Ahmed, G. Ramm, and G. Faltin. “Some Salient Features Of The Time-Averaged Ground Vehicle Wake”. In: *SAE Technical Paper* (Feb. 1984).

[12] A. I. Heft, T. Indinger, and N. A. Adams. “Introduction of a New Realistic Generic Car Model for Aerodynamic Investigations”. In: *SAE Technical Paper* (Apr. 2012).

[13] M. Islam, F. Decker, E. de Villiers, et al. “Application of Detached-Eddy Simulation for Automotive Aerodynamics Development”. In: *SAE Technical Paper* (Apr. 2009).

[14] S. Jakirlic, L. Kutej, P. Unterlechner, et al. “Critical Assessment of Some Popular Scale-Resolving Turbulence Models for Vehicle Aerodynamics”. In: *SAE International Journal of Passenger Cars–Mechanical Systems* 10.1 (Mar. 2017), pp. 235–250.

[15] *OpenFOAM*. https://github.com/OpenFOAM. Accessed: 2019-02-22.